REFLECTANCE MAP TECHNIQUES FOR ANALYZING SURFACE DEFECTS IN METAL CASTINGS

by

ROBERT J. WOODHAM

B.A., University of Western Ontario
(1971)

S.M., Massachusetts Institute of Technology
(1974)

E.E., Massachusetts Institute of Technology
(1974)

Submitted in Partial Fulfillment of the Requirements for the Degree of

Doctor of Philosophy

at the

MASSACHUSETTS INSTITUTE OF TECHNOLOGY

September, 1977

Signature of Author: Robert J. Woodham
Department of Electrical Engineering and Computer Science, September 7, 1977

Certified by: _____
Thesis Supervisor

Accepted by: _____
Chairman, Departmental Committee

REFLECTANCE MAP TECHNIQUES FOR ANALYZING SURFACE DEFECTS IN METAL CASTINGS

by
Robert J. Woodham

Submitted to the Department of Electrical Engineering and Computer Science
on September 7, 1977, in partial fulfillment of the requirements
for the Degree of Doctor of Philosophy

ABSTRACT

This thesis explores how the observed intensity variation across surfaces of smooth objects forces conclusions about the topography of those surfaces. The problem is formulated as a problem in image analysis. A photometric approach is taken. An investigation into the correspondence between image intensity and object relief is presented. The intensity values recorded in an image are related to the surface orientation at the corresponding object points. Changes in intensity across sections of smooth surface are related to object curvature.

Surface orientation cannot be determined locally from the intensities recorded in a single image. Theoretical tools are needed to explore the correspondence between image intensity and object relief. The notion of gradient space, popularized by Huffman and Mackworth, is used to represent surface orientation. The notion of a reflectance map, due to Horn, is used to represent the relation between surface orientation and image intensity. This thesis demonstrates how properties of object curvature can be expressed as constraints on the possible surface orientations that can correspond to a given image point.

Surface orientation can be determined locally from the intensities recorded in multiple images of the same object. This fact is exploited in a new technique called *photometric-stereo*. Additional images are obtained not by moving the viewer or the object but by varying the direction of incident illumination.

The visual inspection of surface defects in metal castings is considered. Two casting applications are discussed. The first is the precision investment casting of turbine blades and vanes for aircraft jet engines. In this application, grain size is an important process variable. An existing industry standard for estimating the average grain size of metals is implemented and demonstrated on sample turbine vanes. The second is the green sand mold casting of shuttle eyes for textile looms. Here, physical constraints inherent to the casting process can be translated into constraints on the surface topography of cast objects. In both cases, visual inspection requires that the observed changes in intensity be interpreted in the context of the local surface topography. The tools developed in this thesis provide a framework for this interpretation.

Thesis Supervisor: Berthold K. P. Horn

Title: Associate Professor of Electrical Engineering and Computer Science

ACKNOWLEDGEMENT

I would like to thank my thesis supervisor, Professor Berthold Horn, and my thesis readers, Professor Patrick Winston and Dr. David Marr, for their support and enthusiasm throughout.

I would also like to thank my two friends and colleagues Mark Lavin and Tomas Lozano-Perez of the M.I.T. AI Lab who were always willing to contribute ideas both of a technical nature and other.

Dr. Mike Fassler, Dr. John Erickson and Dr. Pat Sullivan of the Casting Development Section, Materials Engineering & Research Laboratory, Pratt & Whitney Aircraft and Dr. Jim Blackler of the Draper Division Foundry, Rockwell International provided useful advice and technical assistance.

This research was made possible because of the unique facilities and atmosphere of the M.I.T. Artificial Intelligence Laboratory. For this I have many students, professors, hackers and friends, both past and present, to thank.

I am grateful for the financial support received from the Woodrow Wilson Foundation and the Canada Council.

Finally, a personal note of gratitude to two special people: Louise England, lawyer to be, and Dr. Suzanne Lacasse, civil engineer, who have always been there to bail me out of trouble and keep my foundations secure.

TABLE OF CONTENTS

I. INTRODUCTION

A major motivation for artificial intelligence research is to make machines more useful. One obvious way in which machines can be made more useful is to have them deal directly with their environment. Vision is a powerful mechanism for dealing with the environment. Visual inspection is a useful application of machines that see.

The goal of this thesis is to study how the observed intensity variation across surfaces of objects forces conclusions about the local topography of those surfaces. Interpreting image intensity in terms of underlying surface topography is the key to the automatic visual inspection of metal castings. The problem is formulated as a problem in image analysis. A photometric approach is taken. The research strategy adopted is to examine ways of squeezing the last ounce of information out of the intensity values recorded in an image before taking recourse to high-level knowledge. In order to do this, it is important to investigate the physics and geometry underlying the image forming process.

The thesis begins with a basic investigation into the correspondence between image intensity and object relief. A viewer-centered representation is developed for the determination of shape information from images. The intensity values recorded in an image are related to the surface orientation at the corresponding object points. Changes in intensity across sections of smooth surface are related to the curvature at the corresponding object points.

In order to explore the correspondence between intensity and surface orientation, certain basic theoretical tools are needed. Gradient space, popularized by <Huffman 71> and <Mackworth 73>, is an appropriate representation of surface orientation. The reflectance map, introduced by

<Horn 77a>, is an appropriate representation of the relation between surface orientation and intensity. Using these tools, the surface photometry of objects can be related to the geometry of the image forming process. Physical constraints imposed by the object, its surface photometry and by the light source, object surface and viewer geometry are the basis for photometric methods for determining surface topography directly from intensity information.

The purpose of this theoretical investigation is to develop the necessary tools for understanding how to interpret changes in intensity in terms of local surface topography. The area of application chosen for this thesis is the domain of the visual inspection of surface defects in metal castings. The inspection requirements of the casting industry have been explored. Two particular casting applications are presented. The first is the precision investment casting of turbine blades and vanes for aircraft jet engines. In this application, grain size is an important process variable. An existing industry standard for estimating the average grain size of metals is implemented and demonstrated on sample turbine vanes. The second is the green sand mold casting of shuttle eyes for textile looms. Here, physical constraints inherent to the casting process can be translated into constraints on the local surface topography of cast objects. The problem is that these constraints do not, in general, map into simple features of intensity. Rather, observed changes in intensity must first be interpreted in the context of the local object surface, light source and viewer geometry. The tools developed in this thesis provide a framework for this interpretation.

1.1 INSPECTION IS A GOOD DOMAIN FOR VISION RESEARCH

Vision is a tough problem. One thing that seems to make vision such a tough problem is the fact that many different kinds of knowledge can influence the interpretation of an image. An important question to ask concerns how much of the interpretation of an image is forced by the data itself and how much can be attributed to the influence of prior expectation. This is a difficult question to deal with in human perception because it is impossible to factor out one effect from another experimentally. At best, one can characterize human visual performance as the interaction of diverse, partially complete and possibly redundant knowledge sources.

Inspection is a good domain for vision research precisely because it is a domain which forces one to deal explicitly with the issue of what interpretation is forced by the data. In machine vision, the distinction between "data forced" and "prior expectation" can be dealt with by considering the vision problem to be a two stage process. One begins with the intensity values recorded in an image. The purpose of *image analysis* is to extract features from the raw intensity values and to convert these features into a convenient symbolic representation. The purpose of *scene analysis* is to interpret the symbolic features produced by image analysis according to some externally defined goal. Image analysis defines what can be considered as forced by the data in the subsequent interpretation. Scene analysis, on the other hand, is an exercise in problem solving. In scene analysis, one is free to invoke whatever prior knowledge is available to aid in image interpretation.

Early artificial intelligence research in machine vision concentrated on images of scenes containing plane-faced polyhedra. Initially, the distinction between image analysis and scene analysis seemed clear. The purpose of image analysis was to generate a two-dimensional line drawing of the scene <Binford and Horn 71>. The purpose of scene analysis was to interpret a two-dimensional line drawing in terms of the three-dimensional objects which gave rise to it <Roberts 65>, <Guzman 68>, <Waltz 75>, <Winston 75>.

As the field matured, the actual distinction between image analysis and scene analysis became less clear. A richer form of interaction between image analysis and scene analysis was achieved <Winston 72>, <Freuder 76>. For the most part, this new interaction was aimed at reducing the computational requirements of machine vision. For example, sensitive line verification procedures existed but were too expensive to apply uniformly over an image. The observation to be exploited was that these procedures could effectively be applied to verify the presence of lines hypothesized by scene analysis routines <Shirai 75>.

Nevertheless, a conceptual distinction between image analysis and scene analysis persists. The prevailing thought seems to be that the nature of the features extracted from an image is of less consequence than the subsequent interpretation of those features. This leads research away from basic image analysis and towards more elaborate scene analysis techniques.

In some ways, this is not surprising. Image analysis is a hard problem. Avoiding image analysis is often not so much a question of research philosophy as it is one of practical necessity. Recent work by <Horn 77a> and <Marr 76b>, however, has demonstrated that there is a great

deal of information about three-dimensional shape contained in image intensities and that this information can be computed without recourse to higher-level knowledge. For example, <Horn 77a> shows how a careful analysis of the intensity profiles in images of polyhedra can be used to interpret certain two-dimensional lines directly as convex, concave or occluding. But, in order to exploit this information, it is necessary to understand how images are formed and what determines the observed intensity in an image.

Consider the problem of visual inspection. Normal visual acuity does not guarantee success as an inspector. The initial problem is to learn how to interpret the visual data. However, the most critical requirement for reliable inspection is the ability to eliminate the influence of prior expectation on visual interpretation. The problem of inspection can be likened to that of proof-reading text. If one reads sentences, the expectation of what a word should be makes it very difficult to catch typographical errors. To proof-read effectively, it is necessary to ignore the semantic context of what one is reading and concentrate instead on the individual words and letters. Thus, an inspector is trained to see what he is forced to see rather than what he expects to see. This is precisely what makes inspection a difficult job for people. This is also what makes inspection the right job to hand over to machine vision systems.

In machine vision, the influence of prior expectation can be carefully controlled. In visual inspection, it is necessary to rely on the information contained in the actual intensity values present in an image. This makes inspection a good domain for exploring what can and can not be determined from intensity data alone.

1.2 METAL CASTING IS A GOOD DOMAIN FOR INSPECTION RESEARCH

There are important reasons why metal casting provides a good domain for research in automatic inspection. One set of reasons relates to the demand for automatic inspection systems in the casting industry:

- A foundry is a hostile work environment. OSHA and EPA regulations are forcing foundries to modernize their equipment and safety practices. But, making foundries more acceptable to humans is costly. A better idea is to automate humans out of hazardous areas. A formidable stumbling block to the automatic foundry is the need for inspection.
- Strong foreign competition is forcing the casting industry to re-evaluate its materials usage and energy costs. The goal is to minimize overdesign and associated materials wastage by achieving tighter control over the manufacturing process. Tighter control requires more inspection.
- Productivity in casting inspection is low. Maintaining tight quality standards is a difficult and costly operation. Inspection is a tedious job for humans. Tasks requiring close visual attention create fatigue. Repetitive tasks induce boredom. Yet, inspection demands mental and physical alertness. Automation is the key to increasing inspection productivity.
- Casting is a vital component of the metal working industry. The trend is towards the increased importance of casting as a primary fabrication process. More

sophisticated casting reduces the number of expensive machining operations required to complete the part. More dependable casting reduces the number of expensive machining operations wasted on defective parts. Sophisticated and dependable casting requires better quality inspection.

Another set of reasons for why metal casting provides a good domain for research in automatic inspection relates to the need for flexible, computer-based systems for automation in the casting industry:

- Foundries are job-shop environments. The typical foundry casts many different part geometries in small to medium production quantities. The specialized techniques available for the automation of large volume production are not suited to the foundry. The palletized, pick and place, orientation preserving style of parts handling envisioned by most automation engineers is the antithesis of the parts handling problem in the foundry. For example, castings are tumbled freely in common shaker machines to break away residual mold material and gating. Castings are cleaned in common sand-blast machines. It is not feasible to redesign these operations to preserve part identity and orientation. On-line inspection must be flexible enough to accommodate different part geometries and different methods of part presentation.
- The inspection of a casting does not result in a simple ACCEPT/REJECT decision. Inspection requires interpretation. Often, this interpretation depends on

different kinds of knowledge. Knowledge of the casting process determines the nature of the defects to be found. Knowledge of subsequent machining operations determines the acceptability of surface imperfections. Knowledge of in-service stress patterns determines the critical tolerances for each subsection of the part. In order to apply existing standards, automatic inspection systems must be able to interpret test data within the context of the part as a whole.

- The inspection of castings remains something of an art. Often, there is only a loose correlation between test results and hard evidence as to what functional characteristics of the part are actually being measured. Current research in non-destructive testing emphasizes the extraction of more information from existing test data as much as it does the development of new test techniques. The ability to store and retrieve test data on a computer system adds a new dimension to non-destructive testing. Computer-based interpretation is the key to exploiting as much of the information in the test data as possible.
- Foundries depend critically on the experience of their inspectors. One consequence of this dependence is that there is little or no industry-wide standardization of test interpretation. There is a strong desire to develop such standards for casting inspection. Automation of test interpretation is one way to achieve

standardization. Flexibility in automation is the key to making such standardization useful.

- There is no casting free of imperfections. Imperfections are inherent to the casting process. The goal of manufacturing is to hold these imperfections to specified tolerances. In the automation of casting inspection, the emphasis must be away from simple detection devices and towards computer-based systems. The goal is to allow maximum flexibility in the specification and interpretation of inspection standards.

1.3 WHAT MAKES IMAGE ANALYSIS HARD?

A great deal of information is contained in the intensity values recorded in an image. Yet, much of work in image analysis has not sought to explicitly exploit this fact. Why is this so? In this section, reasons are enumerated for why image analysis is a hard problem. The purpose is to point out some of the difficulties associated with interpreting image intensities. Only by taking cognizance of these difficulties is it possible to understand when and why various image analysis techniques will work and when and why they will fail.

1.3.1 THERE IS A LOT OF DATA IN AN IMAGE

One of the stumbling blocks to image analysis is the sheer quantity of data present in an image. Usually, one wants to forget about image intensities as soon as possible. Image analysis must often rely on data compression. One goal of image analysis is to extract features of intensity which are important and to throw away everything else. But, the

features one can use in a data compression process are those which can be conveniently defined in terms of properties of images. There is not always a simple correlation between properties of images and properties of objects which give rise to those images.

As a rough rule of thumb, one can say that practical vision systems exist only for domains which have the following two properties:

- There is a simple correlation between properties of interest in the domain and properties of images of the domain.
- These image properties are simple to compute.

A good correlation between properties of the domain and properties of images of the domain occurs for domains which are inherently two-dimensional. A significant reduction both in the quantity of data present in an image and in the complexity of feature computation occurs for domains in which intensity can be considered to have only two values. Thus, typical applications of machine vision systems are interpreting images, often binary, of two-dimensional objects. Examples are: optical character recognition (OCR); blood cell analysis <Young 69>; detection of etching defects in printed circuit boards <Ejiri *et al* 73>.

1.3.2 IMAGE PROJECTION CAUSES PROBLEMS

Images have two dimensions while objects exist in a three-dimensional world. Information is lost in the projection of a three-dimensional object onto a two-dimensional image. The mapping from object space to image space is many to one. It is impossible to analyze two-dimensional images without specific assumptions about the three-dimensional nature of the objects that gave rise to them. Properties of images do not always have a simple

correlation with properties of objects. A particular object feature may appear quite differently depending on the viewing direction. More insidious is the fact that projection introduces two-dimensional image features which have no direct correlation with any three-dimensional object property. Neighboring points in an image do not necessarily correspond to neighboring points on objects. Parts of one object may obscure parts of another.

1.3.3 IMAGE ILLUMINATION CAUSES PROBLEMS

The same object viewed with the same imaging geometry will generate different image intensities depending on the position and nature of the incident illumination. Thus, a change in illumination may cause a particular object feature to appear quite differently even when seen from the same viewing direction.

1.3.4 SURFACE PHOTOMETRY CAUSES PROBLEMS

The same object viewed with the same imaging and light source geometry will generate different image intensities depending on the photometric properties of the object surface. Photometric properties vary from object material to object material. For a given object material, the photometric properties vary depending on whether the object is wet or dry, clean or dirty.

1.3.5 THE HUMAN VISUAL SYSTEM IS REMARKABLY FORGIVING

The human visual system does a remarkable job of interpreting image intensity despite the problems caused by projection, illumination and surface photometry outlined above. At first glance, this might be cited as evidence that image analysis can not intrinsically be very hard. This is false optimism and can lead to serious difficulty.

The most widely known example of such a difficulty occurs in color perception. People assign the same color to an object over a wide range of incident illuminations. Mechanical systems have never been able to exhibit this color constancy. The sensitivity of photographic film must be balanced against the spectral composition of the incident illumination. No theory yet exists for how a machine vision system can assign color as a human would. Experimenters in the field soon learn that there is no simple relationship between the spectral composition of a region of an image and the color people will assign to that region.

Similar phenomena can be demonstrated in monochromatic vision. A wide variety of intensity distributions can be made perceptually indistinguishable. The same intensity distribution can be made to appear quite different depending on context. Humans often see things that are not there. These sort of examples are the fodder for research into human visual perception.

Designing an image analysis system by letting intuition decide what the intensities ought to be is a bad idea. One really has to get into the image and look at the actual numbers. This is a necessity in any practical vision application. What this work hopes to do is establish a firmer theoretical foundation for just this sort of analysis.

1.4 WHAT IS TO BE STUDIED?

The questions asked in this work are:

- How are images formed?
- How does the real world constrain an image?
- How is it possible to exploit these constraints in order to interpret the intensity values recorded in an image?

Each of these questions is considered to be a technical question. In this section, it will be convenient to present an informal discussion of the research problem in order to help motivate the technical work to follow. One can write down an equation describing the image forming process roughly as follows:

$$\text{image intensity} = \text{incident illumination} \times \text{surface reflectance} \qquad (1.4.1)$$

The terms image intensity, incident illumination and surface reflectance must be made precise. But, for the moment these technical details will be omitted in order to make some qualitative observations.

In writing down this equation, emphasis is being placed on a photometric approach. This means that image intensity is treated as a measurement arising from a real physical process. Images are to be interpreted by understanding the underlying physical process which gave rise to them.

There are four components underlying the physical process of image forming:

- surface photometry
- surface topography
- incident illumination
- imaging geometry

The surface photometry of an object is determined by the fundamental optical properties of the object material and by its surface micro-structure. Surface micro-structure is surface detail which is too fine to be resolved in the image but which nevertheless causes observable effects in the way incident light is reflected from the object surface. Surface topography, on the other hand, is surface detail which is within the resolution limits of the imaging hardware. It represents the gross object shape relative to the viewer. Incident illumination is the spatial and spectral distribution of the luminous energy falling on the object surface. Finally, imaging geometry determines the projection of the three-dimensional object space onto a two-dimensional image.

Equation (1.4.1) relates image intensity to these four components. In this work, it will be assumed that the surface photometry, incident illumination and imaging geometry are known. Equation (1.4.1) will be used to determine surface topography from image intensity.

1.4.1 RELATION TO OTHER WORK

A variety of other fields embody equation (1.4.1) in one form or another. In computer graphics, for example, one problem is the generation of gray-level images. In this application, surface topography is known. Using an assumed surface photometric function, incident illumination and imaging geometry, (1.4.1) can be used to generate an image of the object(s) in view <Phong 75>. Since gray-level images are readily interpreted by

humans, this is a useful tool in such fields as computer aided design and automated cartography.

If the surface topography, incident illumination and imaging geometry are known, then (1.4.1) can be used to determine the surface photometry from image intensity. If the spectral nature of incident illumination is varied, then the dependence of the surface photometric function on the wavelength of incident illumination can be measured. This is believed to be the key to the perception of color.

If the surface topography, incident illumination, imaging geometry and surface photometry are known, then (1.4.1) can be used to either determine the fundamental optical properties of the object material (assuming a known surface micro-structure) or to determine the surface micro-structure (assuming known fundamental optical properties of the object material). The field of reflectance spectroscopy uses (1.4.1) to determine fundamental optical properties. Reflectance spectroscopy has become an important new tool in analytic chemistry. There are many materials that cannot be analyzed by traditional spectroscopic methods. Some of these materials, however, can be ground into fine powders of known particle size and shape. In turn, analytic models have been developed to relate the photometric properties of such powders to the fundamental properties of the object material of which they are composed <Wendlandt & Hecht 66>.

A recent paper attempts to quantitatively analyze how the observed pattern of sunlight (or moonlight) glitter on a wind-ruffled sea surface can be used to deduce information about the sea state <Plass *et al* 77>. This technique is proposed both as a method for evaluating models of ocean wave structure and for making remote (i.e., satellite) measurements of the parameters that determine sea roughness such as wind speed and direction.

Analyzing the reflection of light from a flat water surface is a simple exercise in geometry and the laws of specular reflection. It is the presence of waves (i.e., surface micro-structure) that complicates this geometry considerably. The glitter pattern actually observed consists of numerous instantaneous "glints" produced by the specular reflection of the light source in the direction of view from momentarily appropriate orientations of small sections of the water surface (wave facets). The shape of the pattern is determined by the distribution of wave inclinations on the water surface. (But, as in any imaging situation, the object surface, light source and viewer geometry must be taken into consideration to account for the fact that oblique observation angles introduce apparent modifications in the wave-slope distribution.)

The above examples are important for several reasons. They illustrate that, in any imaging situation, it is necessary to explicitly account for the dependence of image intensity on the four components: surface photometry, surface topography, incident illumination and imaging geometry. In most applications, however, it is convenient to standardize one or more of these components in order to investigate the dependence of image intensity on the others. The last two examples illustrate the role that surface micro-structure plays in determining the reflectance properties of a surface. In the sea glitter paper, the only process considered is pure specular reflection. Nevertheless, the glitter pattern still is spread out. It is the surface roughness that makes the pattern appear somewhat diffuse. The last two examples also illustrate that, if one has a good analytic model of surface micro-structure, it is possible to predict the reflectance properties for a given object material, and a given object surface, light source and viewer geometry. Finally, the examples

illustrate that, regardless of the application, actual photometric measurements are required to gain insight into the factors that influence the image forming equation (1.4.1).

1.4.2 RELATION TO HUMAN PERCEPTION

This work is based on a photometric model of how images are formed. The goal is to understand the relationship between surface photometry and the light source, object surface and viewer geometry in order to interpret the intensity values recorded in an image. No attempt is made to account for the subjective human perception of those intensity values.

To illustrate, <Beck 74> contains an example of a picture of a "matte" vase. By adding two local "specularities" to this image, a new picture is created in which the entire vase appears shiny. Thus, regions in the first image appear dull while the same regions in the second image appear shiny even though the intensity values recorded are identical. The existence of this and other such human perceptual phenomena does not count as evidence for or against the methods presented here. When terms such as matte and specular are used in this work, they are given a precise technical meaning. Subjective terms such as dull and shiny will be avoided.

1.5 AN ASIDE: THE FOUNDRY AS WORK ENVIRONMENT

Unless one has worked in a foundry, it is impossible truly to appreciate what a hostile environment it is. There are the obvious physical demands and dangers. There are also more subtle hazards. The following quote is taken from a chapter on sand molding in <ASM 70>:

> *"Silica dust from foundry operations can produce silicosis if there is sufficient exposure, in terms of time and concentration, to free crystalline silica dust of particle size below five microns. Two to twenty years (average 10 years) are required to produce a case of silicosis when dust concentrations greatly exceed the maximal allowable...*
>
> *...The oil no-bake binders for sand molds consist of three parts: a modified linseed oil, a metallic drier, and an aromatic isocyanate. Sometimes the last two create a health hazard.*
>
> *Cobalt naphthenate (6% Co), the drier most commonly used in this binder, is slightly toxic. Cobalt compounds can produce contact dermatitis and sensitization. Lead naphthenate is also used as a drier. Lead can be absorbed by the skin and cause lead poisoning, especially when mineral oil, which may induce dermatitis and irritation, is used.*
>
> *Under certain conditions of poor ventilation, the amount of aromatic isocyanate (methylene diphenyl ditsocyanate, MDI) vapor liberated in shakeout operations may be a significant health hazard. Operators of shakeout devices and of overhead cranes in the area should wear an approved organic vapor respirator. Persons with known asthmatic history should not be employed on operations that release high levels of MDI vapor. To reduce decomposition of MDI, neither the sand nor the binder should be heated above 125 F. Staining of the hands by MDI can be reduced if molders use protective creams resistant to oils and solvents and wear rubber or plastic-coated canvas gloves."*

2. A FRAMEWORK FOR INTERPRETING INTENSITY CHANGE

This chapter develops the theoretical framework used for interpreting the intensity changes in an image. The goal is to relate image intensity to properties of the object being imaged. Three object properties are considered:

- Range
- Surface Orientation
- Curvature

These properties are used as the basis for a viewer-centered representation scheme for determining the shape of objects from their images. The connection between these three object properties and image intensity is determined by the surface photometry of the objects in view, by the nature of the incident illumination and by the object surface, light source and viewer geometry.

The image analysis problem is formulated as the problem of determining, at each point in an image, the range, the surface orientation and the object curvature at the corresponding object point. *Range* is defined to be the distance of the object point from the viewer. It is a single-valued function at each image point. *Surface orientation* is defined to be the direction of an outward surface normal at the object point. It is a two-valued function at each image point. *Curvature* is defined to be the two principal curvatures (and associated directions) at the object point. It is a three-valued function at each image point. The range, surface orientation and object curvature at an image point together define the *object relief* at that image point.

The approach taken here is photometric. An analysis of the basic image forming equation:

image intensity = incident illumination x surface reflectance (2.1)

is used to show how image intensity is related to surface orientation and how a change in image intensity is related to curvature.

2.1 A VIEWER-CENTERED REPRESENTATION FOR SHAPE INFORMATION

An important question to ask of any problem solving system is what representations are used for the different kinds of information needed at each stage of problem solution. This section outlines the representation scheme used in the initial determination of shape information from images. In image analysis, the representation used will depend more upon what it is possible to compute from the intensity values in an image than on what is ultimately desirable. In subsequent stages of analysis, the representations can be made more sensitive to the needs of the specific application.

A viewer-centered representation is chosen for the initial determination of the shape of objects in an image. This representation distinguishes the following three classes of scene feature:

1. Contours of range discontinuity. (OCCLUSION boundaries)
2. Contours of discontinuity of surface normal (CONVEX and CONCAVE edges)
3. Sections of smooth surface.

<Marr 77> calls this representation the 2-1/2-D sketch and argues for its usefulness as an intermediate representation in an overall vision system for determining shape (in an object-centered coordinate system). The goal here is to explore how such a viewer-centered intermediate

representation can be determined directly from the intensity values recorded in an image. The particular question addressed in this chapter is how the range, surface orientation and curvature can be determined for sections of smooth surface.

In order to do this, gradient space and the reflectance map are defined. Using these tools, the physical constraints imposed by the light source, object surface and viewer geometry are translated into geometric constraints on the possible surface orientations that can correspond to a given image point. These geometric constraints form the basis for photometric methods to determine the range, surface orientation and curvature at object points corresponding to given image points. In this chapter, a particular relaxation algorithm is presented which determines surface orientation from a single image by propagation of mutual constraint on possible orientations at selected image points consistent with general hypotheses about object shape. This algorithm serves to illustrate how physical contraint imposed by the imaging geometry can be used to constrain surface topography. The purpose of this presentation is to build insight and intuition into the framework for interpreting intensity change. The mathematical details are found in Appendix: A.

2.2 DETERMINING OBJECT RELIEF

There is nothing in the initial formulation that says object relief has anything to do with intensity. This connection is established by examining the underlying photometry of the image forming process. First, however, it is worthwhile reviewing the different techniques available for determining object relief (at a distance). Figure 2-1 summarizes these techniques.

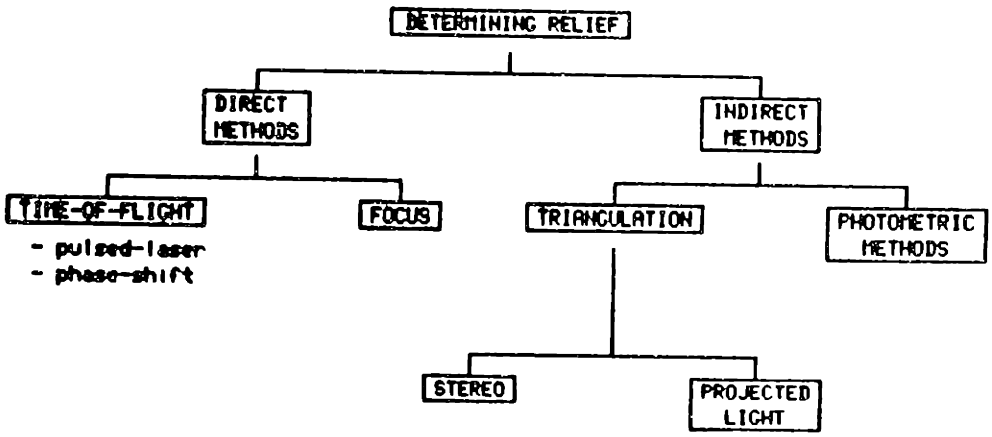

Figure 2-1 Characterizing techniques for determining object relief (at a distance).

Roughly speaking, the methods for determining object relief can be divided into two categories. First, there are methods which attempt to measure range directly. Focussing, for example, can be used as a direct ranging technique. The focus of an optical system depends on the range of the objects being imaged. Techniques for the automatic focussing of imaging systems have been explored <Horn 68>. In an early experimental system <Winston 72>, automatic focussing was able to locate objects in a scene to an accuracy of about ±1 inch at a total distance of about 6 feet (approximately ±1 part in 100). The use of focussing as a ranging technique depends, however, on the presence of sharp features (such as edges) in the scene. It is not suited for ranging over surfaces with smoothly varying topography.

Another method for determining range directly is based on time-of-flight measurements of a signal reflected back from the object surface. One design technique uses a pulsed laser to measure time-of-flight directly. This approach has proven practical for the long distance ranging required in space exploration <Johnston 73>. It has also been applied to more terrestrial endeavors <Caulfield 76>. A more common design technique for short distance ranging measures time-of-flight as the phase shift between the emitted and returning signal. The CW LIDAR Pointing System developed at the C. S. Draper Laboratory measures time-of-flight this way using a non-coherent LED (centered at 910 nanometer) amplitude modulated at 50 MHz. <DRAPER 73>. This system is reported to be accurate to ±1 millimeter at a total distance of about 3 meters (approximately ±1 part in 3000). A similar system has been developed at Stanford Research Institute and is reported in <Nitzan *et al.* 77>. This last article includes a useful discussion of the

inherent design trade-offs associated with such direct ranging devices. Basically, accuracy is achieved by maintaining a favorable signal to noise ratio. The signal to noise ratio can be improved either by increasing the power of the source or increasing the time constant used to sample each point.

Second, there are methods which determine range from indirect measurements. These techniques can be further subdivided into triangulation methods and photometric methods. One kind of triangulation method uses a stereo pair of images obtained from two known positions. Any point in an image determines a ray in space. The range at a point in an image is determined by computing the intersection of this ray and the ray determined by the corresponding point in the other image. But, in order to determine the second ray, it is first necessary to find the corresponding point in the other image. Thus, stereo ranging suffers from the same qualitative limitations as does the technique of automatic focussing. Solving the correspondence problem depends on the presence of features in one image that can be matched to features in the other. It is unsuitable for ranging over surfaces with smoothly varying topography.

Another kind of triangulation method avoids the correspondence problem by using specially controlled illumination. The idea is to project thin sheets of light sequentially on the scene and record the image resulting from each sheet. The range at a point in an image is determined by computing the intersection of the ray associated with the image point and the sheet of light which illuminated the point.

There is one reported technique which uses specially controlled illumination to determine surface orientation directly. <Will & Pennington 71> describe a method which uses special illumination to

code surface orientation as the modulation on a spatial frequency carrier grid. With this method, it is possible to extract the surface orientation of planar regions in a scene by linear frequency domain filtering.

Finally, as indicated above, photometric methods are methods which determine range from an analysis of the image forming equation (2.1). A photometric approach to range determination was first proposed in <van Diggelen 51> and subsequently applied to lunar images obtained from Ranger spacecraft <Rindfleisch 65>. The particular photometric properties of the material of the maria of the moon cause a simplification in the mathematics required to determine range from intensity. <Horn 75> generalized the photometric approach to account for surfaces with arbitrary photometric properties. The relation between image intensity and object surface is determined by surface orientation. The relation between a change in image intensity and a change in surface orientation is determined by object curvature. If the surface orientation at each object point can be determined, then the corresponding range value is obtained by starting at a known point and integrating surface orientation (over sections of smooth surface). Photometric methods are complementary to stereo ranging and focus ranging. Photometric methods are most suited to surfaces with smoothly varying topography. (The integration of surface orientation cannot be carried out across discontinuities in range or discontinuities in surface orientation.)

In photometric methods, the problem of determining the object relief becomes a problem in image analysis. But, regardless of how object relief is determined, it is important to realize that oject relief corresponds to an image with the effects due to incident illumination and surface photometry explicitly factored out. Thus, exploring how to determine

object relief directly from the intensity values recorded in an image is important to image analysis because it addresses the issue of how to account for the effects of incident illumination and surface photometry.

Note, however, that two stumbling blocks remain. First, determining object relief does nothing to overcome the problems associated with the quantity of data present in an image. Indeed, if object relief is determined at each image point, the quantity of data and associated computational load increases significantly. But, data compression for subsequent scene analysis has a more explicit representation to deal with when based on relief than when based strictly on intensity and thus can do a better job <Nevatia & Binford 73>. Second, while knowledge of object relief solves some of the problems associated with image projection (eg. depth discontinuities can be used to separate objects in an image), it nevertheless still corresponds to a viewer-centered representation of shape. It is at this point that it becomes necessary to invoke some external assumptions about the objects in view if one intends to recover the three-dimensional structure lost in the image projection.

2.3 GRADIENT SPACE AND THE REFLECTANCE MAP

In order to understand the correspondence between intensity data and surface orientation, it is necessary to relate the geometry of the image forming process to the photometry of the object being imaged. The problem of determining surface orientation from intensity can be characterized as a mapping:

$$T: I(u,v) \rightarrow SO(u,v)$$

which assigns to each image intensity point I(u,v) a surface orientation SO(u,v). In a visual world consisting of opaque smooth objects immersed in

a transparent medium, the mapping T is well defined since each image intensity point I(u,v) arises from a unique object point (which, in turn, defines a unique surface orientation). What is not obvious, however, is whether T can be determined from intensity data alone. The difficulty is that, in terms of intensity, T is not a local operator. In formulating methods for determining surface orientation from image intensity, it will be important to keep track of the photometric and physical constraints that are invoked.

SO(u,v) is a two-valued function of u and v since two parameters are required to specify an arbitrary direction in space. One might expect surface orientation to be difficult to represent explicitly. Gradient space is an appropriate formalism for reasoning about surface orientation.

Gradient space can be motivated in several ways. For present purposes, it will be related directly to surface orientation. If the equation of a smooth surface is given explicitly as:

$$z = f(x,y)$$

then a surface normal is given by:

$$\left[\frac{\partial f(x,y)}{\partial x}, \frac{\partial f(x,y)}{\partial y}, -1\right]$$

Define:

$$p = \frac{\partial f(x,y)}{\partial x}$$

$$q = \frac{\partial f(x,y)}{\partial y}$$

so that the surface normal becomes (p,q,-1). The quantity (p,q) will be called the *gradient* and *gradient space* is defined to be the two-dimensional space of all such points (p,q).

Gradient space can be used to relate image intensity to surface orientation. In general, the fraction of light reflected by a surface in a given direction depends upon the optical properties of the object material, the surface micro-structure and the spatial and spectral distribution of the incident light. The key photometric observation underlying the relation between intensity and surface orientation is the following:

> *No matter how complex the distribution of incident illumination, for most surfaces, the fraction of the incident light reflected in a particular direction depends only on the surface orientation.*

To make this observation more concrete, one can standardize the representation of the light source, object surface and viewer geometry and tie this representation down to gradient coordinates p and q.

A surface photometric function $\phi(i,e,g)$ is defined in terms of the three photometric angles i, e and g illustrated in figure 2-2. These angles are called, respectively, the incident, emergent and phase angle. In this work, the emergent angle e will always be referred to as the *view angle*.

The photometric angles i, e and g are defined in an object-based coordinate system. If, however, both the viewing direction and the direction of incident illumination are known, then expressions for cos(i), cos(e) and cos(g) can be derived in terms of gradient space coordinates p and q. As a prelude to this, one must standardize the geometry of the image forming process. Suppose one chooses to describe objects in a (left-handed) coordinate system. To simplify the mathematics, one can align the viewing direction with the negative z-axis. Most image forming systems perform a *perspective projection* as illustrated in figure 2-3(a). But for objects that are small compared to the viewing distance, the

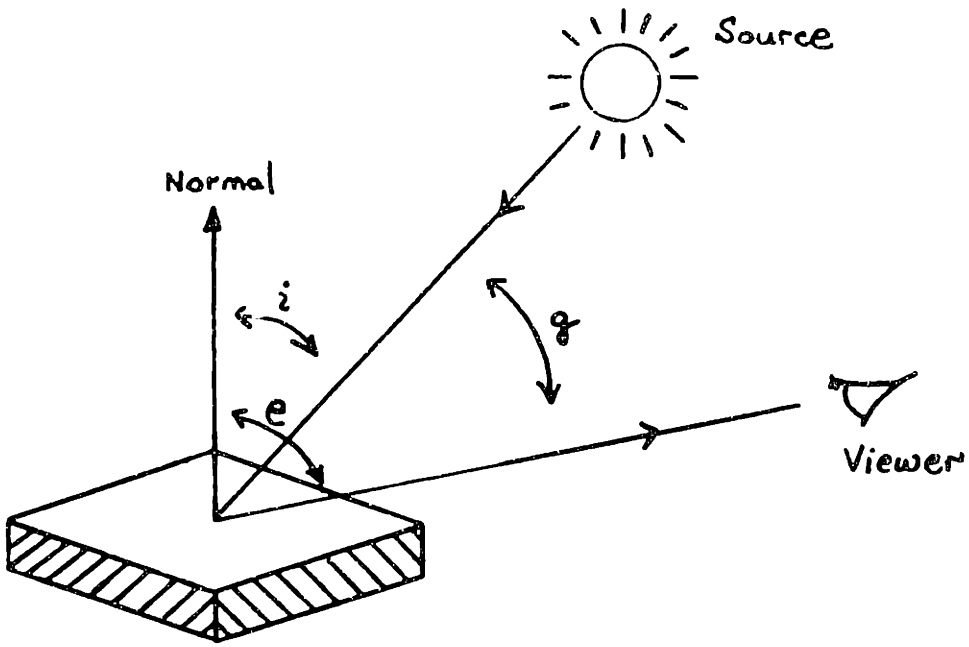

Figure 2-2 Defining the three photometric angles i, e and g. The incident angle i is the angle between the incident ray and the surface normal. The view angle e is the angle between the emergent ray and the surface normal. The phase angle g is the angle between the incident and emergent rays.

perspective projection can be approximated as an *orthographic projection* as illustrated in figure 2-3(b).

Consider an image forming system that performs an orthographic projection. To further simplify the mathematics, assume a scaling of the image plane that takes object point (x,y,z) to image point (u,v) where u = x and v = y. With this imaging geometry, the use of separate image coordinates (u,v) is redundant. Henceforth, image coordinates (x,y) and object coordinates (x,y) will be referred to interchangeably.

Consider an imaging situation in which each object point receives the same incident illumination. In such a situation, the amount of the incident light reflected in a particular direction depends only on the surface orientation. Further, consider an imaging situation in which the viewing direction is constant for all object points. (This is true for an orthographic projection.) Then, for a given distribution of incident illumination, a given surface-viewer geometry and a given object material, the image intensity corresponding to a surface point with gradient (p,q) is unique. The *reflectance map* R(p,q) corresponds to the intensities recorded at each (p,q). If an image point (x_0,y_0) is known to correspond to gradient point (p_0,q_0), then it is possible to normalize the image intensity values I(x,y) with respect to the reflectance map R(p,q) so that the image forming equation (2.1) becomes:

$$I(x,y) = R(p,q) \qquad (2.3.1)$$

Notice what has happened. The reflectance map captures the surface photometry of the object for a particular light source, object surface and viewer geometry. The two assumptions necessary to write (2.1) as (2.3.1) are:

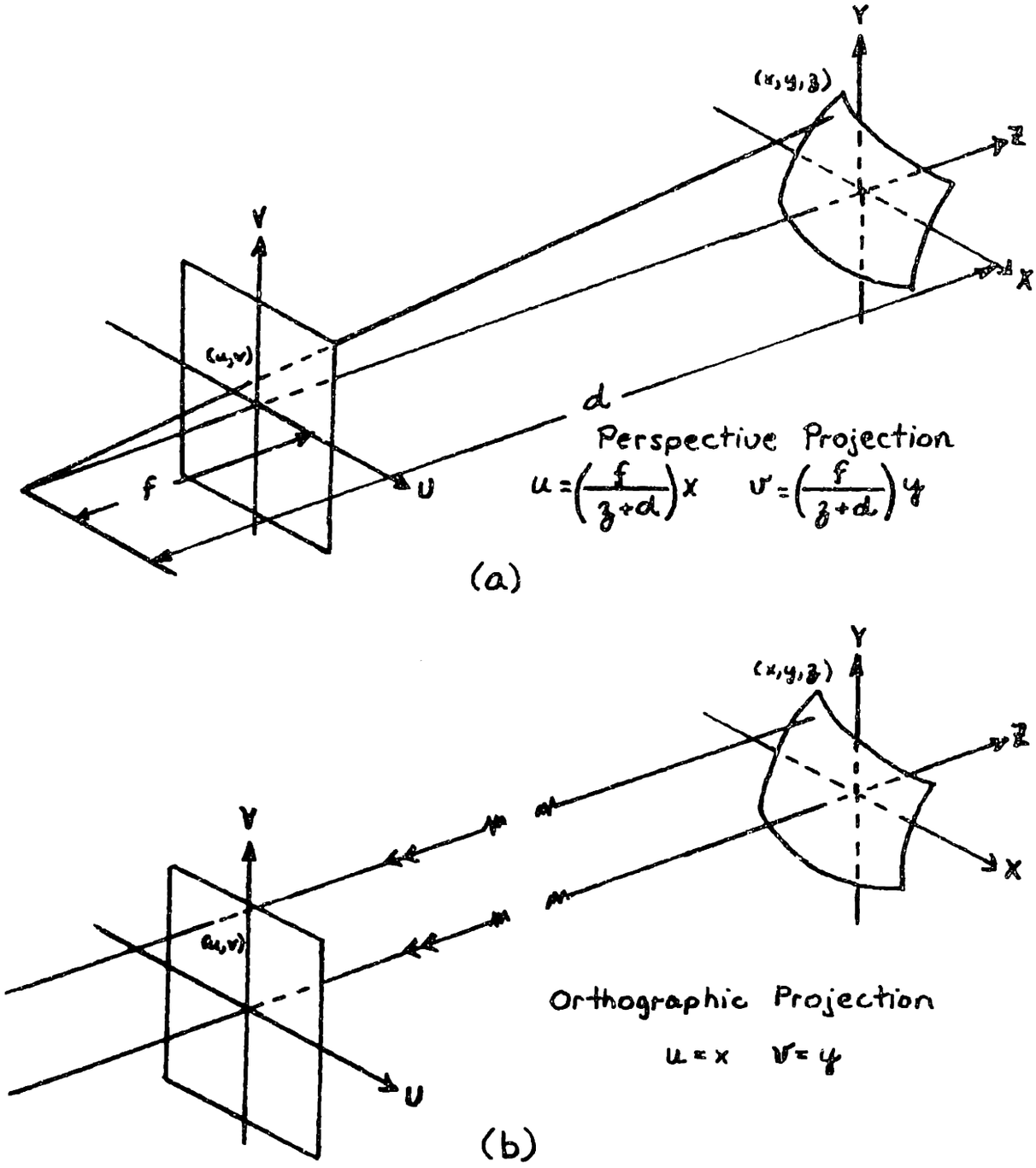

Figure 2-3 Characterizing image projection. Figure 2-3(a) illustrates the well-known perspective projection. [Note: to avoid image inversion, it is convenient to assume that the image plane lies in front of the lens rather than behind it.] For objects that are small relative to the viewing distance, the image projection can be modeled as the orthographic projection illustrated in figure 2-3(b). In an orthographic projection, the focal length f is infinite so that all rays from object to image are parallel.

1. Each object point receives the same incident illumination.
2. The image forming projection is orthographic.

The important simplification inherent in the assumption of an orthographic projection is that the viewing direction, and hence the phase angle g, is constant for all object points. This is what allows one to transform a surface photometric function $\phi(i,e,g)$, a function of three variables, into a reflectance map R(p,q), a function of two variables. In addition, the assumption that the size of the objects is small compared to the viewing distance allows one to relate the amount of light reflected per unit solid angle in the direction of viewer directly to image intensity. The variation in distance from the viewer at individual object points is assumed small compared to the total object distance. Thus, it is not necessary to explicitly account for the inverse square fall-of in radiant intensity.

Reflectance maps can be determined empirically, derived from phenomenological models of surface reflectivity or derived from analytic models of surface micro-structure. Once determined, however, the reflectance map is independent of the shape of the objects being viewed. A reflectance map is not an image. It represents explicit knowledge of intensities that can be recorded from objects made of a given material and viewed under a particular light source and viewer geometry.

Equation (2.3.1) is the basic equation used to relate image intensity to the geometry of the image forming process. It is one equation in the two unknowns p and q. Thus, the problem of determining surface orientation from intensity becomes the problem of finding the point in gradient space (p,q) corresponding to the image intensity point I(x,y).

The simplest case for incident illumination is that of a single distant point source. Choose such a source and place it so that object space vector $(p_s, q_s, -1)$ points in the direction of the source. That is, the source is located at gradient space point (p_s, q_s). Object space vector (0,0,-1) points in the direction of the viewer. That is, the viewer is located at gradient space point (0,0). Recall that, object space vector (p,q,-1) is a normal to the surface point (x,y,z). That is, (p,q) is the gradient point corresponding to the surface point (x,y,z). Note that, with the imaging geometry of figure 2-3(b), (p,q,-1) defines an outward surface normal facing the viewer.

Then, using standard vector algebra, the expressions for cos(i), cos(e) and cos(g) become:

$$\cos(i) = \frac{1 + pp_s + qq_s}{\sqrt{1 + p_s^2 + q_s^2}\ \sqrt{1 + p^2 + q^2}}$$

$$\cos(e) = \frac{1}{\sqrt{1 + p^2 + q^2}}$$

$$\cos(g) = \frac{1}{\sqrt{1 + p_s^2 + q_s^2}}$$

Specifying a single distant point source is not a fundamental restriction on the development. Non-point sources can be modeled as the superposition of single point sources. The development does, however, assume equal illumination at all surface points. For non-convex surfaces, the reflectance map does not account for the fact that certain surface points can be shadowed with respect to one or more of the sources nor for the fact that certain surface points can receive additional illumination due to light reflected from other sections of surface (mutual illumination).

Using the above expressions, it is clear that one can transform an arbitrary surface photometric function $\phi(i,e,g)$ into a reflectance map $R(p,q)$. By now, it should also be clear how points in gradient space correspond to orientations in object space. However, it is possible to be more explicit about the correspondence between movement in gradient space and changes in surface orientation.

Using elementary trigonometry, the expression for cos(e) can be rewritten as:

$$\tan(e) = \sqrt{p^2 + q^2}$$

This says that the inclination of the surface with respect to the viewing direction varies monotonically with the distance from the origin in gradient space. Specifically, the distance from the origin is the tangent of the angle between the surface normal and the view vector. As the gradient (p,q) moves away from the origin, the inclination of the surface with respect to the viewer increases.

The view angle e characterizes one of the two degrees of freedom associated with an arbitrary orientation in space. Note that the locus of points in object space having a constant view angle e defines a right circular cone oriented along the viewing direction. The angular position $\tan^{-1}(q/p)$ of each gradient (p,q) on the circle $p^2 + q^2 = \tan^2(e)$ determines the direction of steepest descent in image space along this cone. This says that the angular position of a point (p,q) in gradient space corresponds to the direction of steepest descent in image space along the original surface. As a consequence, rotating object space about the view vector induces an equal rotation in gradient space.

2.4 RE-EXAMINING PHYSICAL CONSTRAINTS

One can formulate the problem of determining the point in gradient space (p,q) corresponding to the image intensity point I(x,y) analytically as has been done in <Horn 75> <Horn 77a>. This work is reviewed briefly in Appendix: A.1. For the moment, the formal nature of the problem will be put aside in order to re-examine its basis in the physical world.

Two constraints of importance can be identified:

1. A given point on a physical surface has a unique orientation in space.
2. Matter is cohesive. It is separated into objects. The surfaces of objects are generally smooth compared with their distance from the viewer.

These are essentially the same two constraints <Marr & Poggio 76> use as a basis for their method to compute stereo disparity. As in their paper, the problem is to translate the above two physical constraints into rules for how points in an image can be matched to points in gradient space.

In their most general form, these rules can be expressed as:

1. UNIQUENESS:

   Each image point may be assigned to at most one location in gradient space.

2. CONTINUITY:

   Surfaces vary smoothly almost everywhere. Only a small fraction of the area of an image is composed of boundaries that correspond to discontinuities of range or surface orientation.

The task ahead is to demonstrate that these rules can be explicitly embedded in a computation. The result is an algorithm which attempts to achieve a global correspondence between image points and points in gradient space via propagation of local constraints.

Such methods have been called cooperative algorithms <Marr & Poggio 76> or relaxation labelling <Rosenfeld, Hummel & Zucker 76>. Although the implementation has some intrinsic interest, what is most important here is to understand the physical basis for the local constraints used and to get the flavor of how these local constraints can propagate back and forth to constrain globally possible matches between image points and points in gradient space.

2.5 SPECIFYING LOCAL CONSTRAINT

The basic image forming equation

$$I(x,y) = R(p,q)$$

is one equation in the two unknowns p and q. By this equation alone, the gradient corresponding to a particular image point is constrained to lie on a one parameter (family of) contour(s) in gradient space. The goal is to apply further constraint in order to assign a unique location in gradient space to each image point.

The essential physical constraint to be exploited is the assumption that, compared to the viewing distance, surfaces vary smoothly almost everywhere. This surface smoothness assumption is translated into monotonicity rules on changes to view angle and changes to direction of steepest descent permitted between (closely spaced) image points.

One can illustrate how physical constraint adds additional constraint to the possible gradient space solutions to the basic equation $I(x,y) = R(p,q)$. Suppose, two (closely spaced) image points (x_1,y_1) and (x_2,y_2) are hypothesized to correspond to object points on the same section of smooth surface. Further, suppose that the view angle increases in going from (x_1,y_1) to (x_2,y_2) and that the angular position, corresponding to the direction of steepest descent, decreases in going from (x_1,y_1) to (x_2,y_2). Let (p_1,q_1) and (p_2,q_2) be the gradient locations corresponding to (x_1,y_1) and (x_2,y_2).

Suppose, further, that the basic equation $I(x,y) = R(p,q)$ constrains (p_1,q_1) and (p_2,q_2) to lie on the contours C_1 and C_2 respectively as shown in figure 2-4.

Figure 2-5 shows both the gradient space circle corresponding to the maximum view angle interpretation of (p_2,q_2) (i.e., the circle passing through the point on C_2 furthest from the origin) and the gradient space line corresponding to the minimum direction of steepest descent interpretation of (p_2,q_2) (i.e., the line passing through the point on C_2 with minimum angular position). Since the view angle is assumed to increase in going from (x_1,y_1) to (x_2,y_2), the contour of permissible (p_1,q_1) can be restricted to include only those gradient points on C_1 lying on or within the circle of the maximum view angle interpretation of (p_2,q_2). Similarly, since angular position is assumed to decrease in going from (x_1,y_1) to (x_2,y_2), the contour of permissible (p_1,q_1) can be restricted to include only those gradient points on or above the line of the minimum direction of steepest descent interpretation of (p_2,q_2). Thus, without any additional constraint on (p_2,q_2), the assumed monotonicity relations between (x_1,y_1) and (x_2,y_2) have been applied to the reflectance

map contours to constrain the possible interpretation of (p_1, q_1) to include only those points of C_1 indicated by the solid line of figure 2-5.

Let (r,θ) denote the polar representation of the gradient space point (p,q). That is:

$$r = \sqrt{p^2 + q^2}$$

$$\theta = \tan^{-1}(q/p)$$

Generalizing from the above illustration, the following two rules are stated:

RULE I: CHANGES IN VIEW ANGLE

Let $I_1, I_2, \ldots, I_n$ be a set of (closely spaced) image points hypothesized to correspond to object points on the same section of smooth surface that are monotonically non-decreasing in view angle. Let $C_1, C_2, \ldots, C_n$ be the corresponding set of gradient contours determined from the reflectance map. Then, each contour C_i can be further constrained such that, for each $(r,\theta) \in C_i$, $i = 2,3,\ldots,n-1$

$$\min \{r \mid (r,\theta) \in C_{i-1}\} \leq r \leq \max \{r \mid (r,\theta) \in C_{i+1}\}$$

Similarly, if $I_1, I_2, \ldots, I_n$ is hypothesized to correspond to a set of object points on the same section of smooth surface that are monotonically non-increasing in view angle, then each contour C_i can be further constrained such that, for each $(r,\theta) \in C_i$, $i = 2,3,\ldots,n-1$

$$\min \{r \mid (r,\theta) \in C_{i+1}\} \leq r \leq \max \{r \mid (r,\theta) \in C_{i-1}\}$$

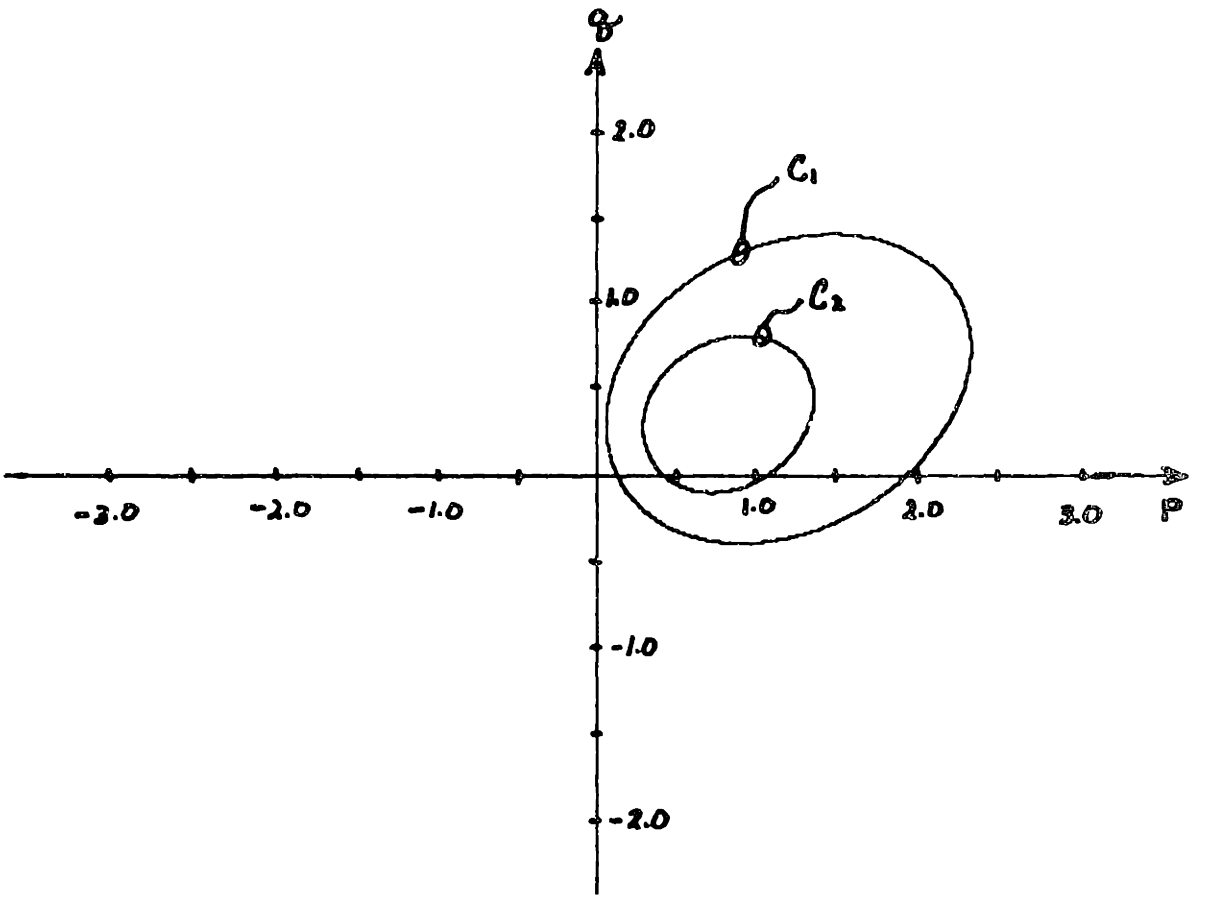

Figure 2-4 The two reflectance map contours C_1 and C_2 which determine possible surface orientations at image points (x_1, y_1) and (x_2, y_2).

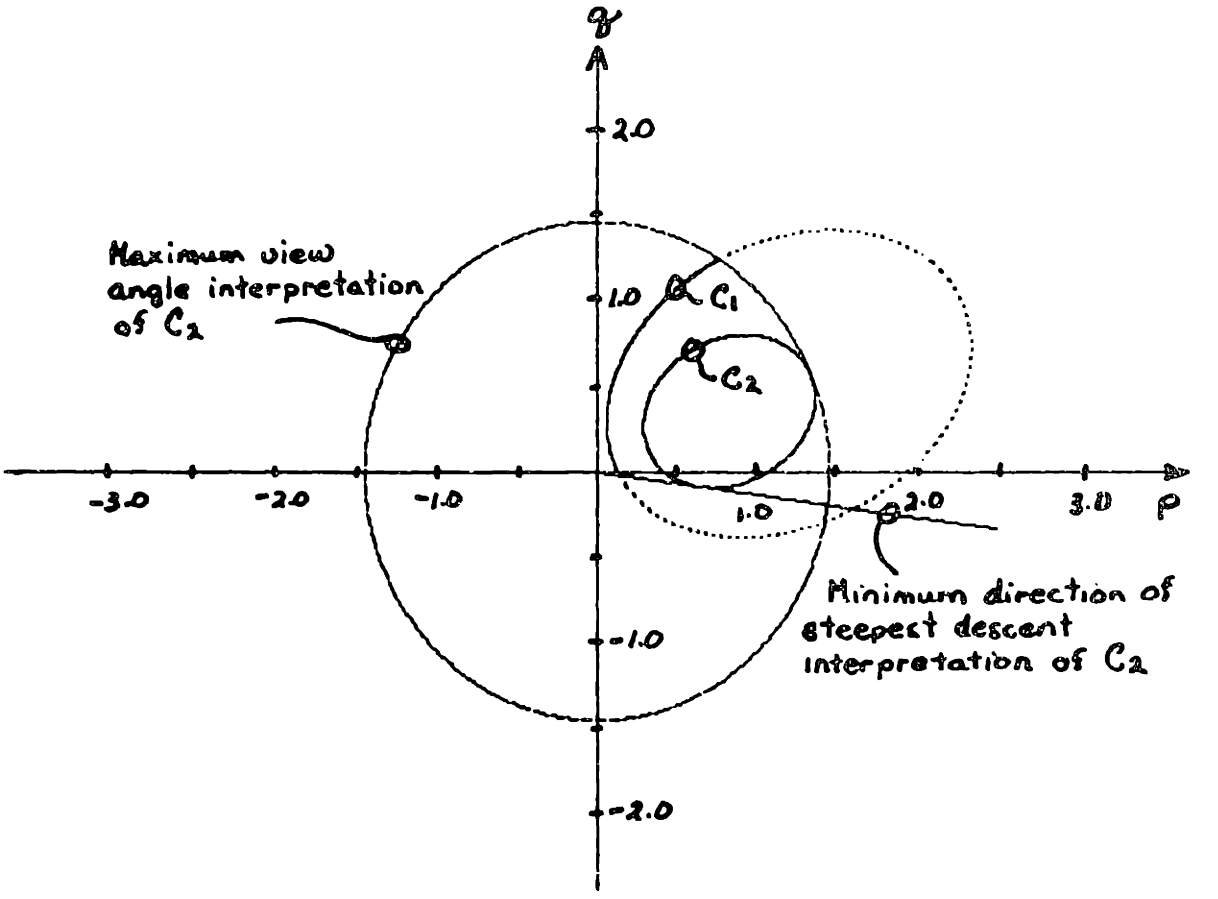

Figure 2-5 The restricted subsection of contour C_1 that is consistent with the hypothesis that the view angle increases and the direction of steepest descent decreases in going from (x_1, y_1) to (x_2, y_2).

RULE II: CHANGES IN DIRECTION OF STEEPEST DESCENT

Let $I_1, I_2, \ldots, I_n$ be a set of (closely spaced) image points hypothesized to correspond to object points on the same section of smooth surface that are monotonically non-decreasing in direction of steepest descent. As above, let $C_1, C_2, \ldots, C_n$ be the corresponding set of gradient contours. Then, each contour C_i can be further constrained such that, for each $(r,\theta) \in C_i$, $i = 2,3,\ldots,n-1$

$$\min \{\theta \mid (r,\theta) \in C_{i-1}\} \leq \theta \leq \max \{\theta \mid (r,\theta) \in C_{i+1}\}$$

Similarly, if $I_1, I_2, \ldots, I_n$ is hypothesized to correspond to a set of object points on the same section of smooth surface that are monotonically non-increasing in direction of steepest descent, then each contour C_i can be further constrained such that, for each $(r,\theta) \in C_i$, $i = 2,3,\ldots,n-1$

$$\min \{\theta \mid (r,\theta) \in C_{i+1}\} \leq \theta \leq \max \{\theta \mid (r,\theta) \in C_{i-1}\}$$

2.6 HYPOTHESIZING MONOTONICITY RELATIONS

It is now time to turn to the question of how to hypothesize monotonicity relations between selected image points. To begin with, consider the worst possible approach. For some small value of n, one might explore all possible orderings, with respect to both view angle and direction of steepest descent, of selected (closely spaced) image points $I_1, I_2, \ldots, I_n$. The hope would be that only a small fraction of those orderings would have admissable interpretations (i.e., interpretations that included at least one gradient point for each image point). The constraints imposed by each interpretation would propagate to neighboring sets of selected image points to provide further mutual constraint. Again,

the hope would be that propagation of local constraint would converge to a correct global interpretation while "incorrect" propagations would (quickly) die out.

Consider a second possible approach. Suppose a particular surface interpretation is forced onto the data. Such an interpretation would provide a framework to (partially) order selected (closely spaced) image points with respect to changes in both view angle and direction of steepest descent. Instead of allowing all possible orderings to compete, this second approach pursues a particular interpretation. Again, the hope would be that propagation of local constraint would converge to a single global interpretation that represents a simple distortion of the particular interpretation being forced. (Here, simple distortion implies any surface that preserves the assumed monotonicity relations concerning changes to view angle and changes to direction of steepest descent.)

The method actually implemented corresponds to this second approach. The program has a small set of interpretations it is willing to pursue. Some are quite rigid, others are quite flexible. In the next section, a specific example is presented. For now, a brief analysis is given to show how convexity can be used to hypothesize monotonicity relations between (closely spaced) image points. In the process, an important theory will be developed. (See Appendix: A for a more rigorous formulation of the results presented here.)

By taking partial derivatives of the basic equation $I(x,y) = R(p,q)$ with respect to x and y two equations are obtained which can be written as the single matrix equation:

$$\begin{bmatrix} I_x \\ I_y \end{bmatrix} = \begin{bmatrix} p_x & q_x \\ p_y & q_y \end{bmatrix} \begin{bmatrix} R_p \\ R_q \end{bmatrix} \qquad (2.6.1)$$

(Throughout, subscripts are used to denote partial differentiation). Similarly, the two first-order equations

$$dp = p_x dx + p_y dy$$

$$dq = q_x dx + q_y dy$$

can be written as the single matrix equation:

$$\begin{bmatrix} dp \\ dq \end{bmatrix} = \begin{bmatrix} p_x & p_y \\ q_x & q_y \end{bmatrix} \begin{bmatrix} dx \\ dy \end{bmatrix} \qquad (2.6.2)$$

For smooth surfaces, the order of differentiation can be interchanged. Thus, recalling the original definitions of p and q, observe that

$$p_y = q_x$$

One can define a matrix H by:

$$H = \begin{bmatrix} \frac{\partial^2 f(x,y)}{\partial x^2} & \frac{\partial^2 f(x,y)}{\partial x \partial y} \\ \frac{\partial^2 f(x,y)}{\partial x \partial y} & \frac{\partial^2 f(x,y)}{\partial y^2} \end{bmatrix}$$

H is the standard Hessian matrix of the function $z = f(x,y)$. Here, H is called the *image Hessian matrix* of the surface $z = f(x,y)$. H captures the notion of surface curvature (in a viewer-centered representation). The image Hessian matrix H can be related directly to an object-centered definition of curvature (see Appendix: A.5).

Equation (2.6.2) can be written in the form:

$$[dp,dq]^T = H\,[dx,dy]^T$$

to emphasize that it is the image Hessian matrix H that relates movement in the image to the corresponding movement in gradient space.

The particular result of importance to this section is that a property of the image Hessian matrix H can be related to the convexity (concavity) of the object surface $z = f(x,y)$.

> The object surface $z = f(x,y)$ is convex (with respect to the viewer) if and only if the corresponding image Hessian matrix H is positive semidefinite.

Similarly,

> The object surface $z = f(x,y)$ is concave (with respect to the viewer) if and only if the corresponding image Hessian matrix H is negative semidefinite.

Suppose $z = f(x,y)$ is convex. Then, H is positive semidefinite. Multiplying the two matrix equations (2.6.1) and (2.6.2) on the left by $[R_p \; R_q]$ and $[dx \; dy]$ respectively, gives rise to the two inequalities:

$$I_x R_p + I_y R_q \geq 0 \qquad (2.6.3)$$

$$dp\, dx + dq\, dy \geq 0 \qquad (2.6.4)$$

Two similar inequalities hold, with the sense of the inequality reversed, if $z = f(x,y)$ is concave. Note, however, that concavity need not be treated as a separate case. Indeed, ignoring shadows and mutual illumination, the classic indentation/protrusion ambiguity has a simple expression in this framework.

> If $I(x,y)$ is the image corresponding to a concave surface $z = f(x,y)$ illuminated by a single point source at gradient point (p_s, q_s) then $I(x,y)$ is also the image corresponding to the convex surface $z = -f(x,y)$ illuminated by a single point source at gradient point $(-p_s, -q_s)$.

The first inequality (2.6.3) can be viewed as an additional *a priori* constraint on the contour in gradient space of possible solutions to the basic equation $I(x,y) = R(p,q)$ for a convex surface $z = f(x,y)$. The normal vector $[R_p, R_q]$ to the contour of constant reflectance at any point (p,q) hypothesized to be a solution to the basic equation $I(x,y) = R(p,q)$ must have a non-negative component in the direction of the normal vector $[I_x, I_y]$ to the contour of constant intensity at (x,y).

The second inequality (2.6.4) can be viewed as an additional constraint on the possible movement [dp,dq] in gradient space corresponding to a movement [dx,dy] in the image. As above, the vector [dp,dq] must have a non-negative component in the direction [dx,dy]. Thus, by choosing [dx,dy] appropriately, it is possible to guarantee either the sign of the change to the view angle or the sign of the change to the direction of steepest descent. (See Appendix: A.2)

2.7 ACHIEVING GLOBAL CONSTRAINT

Regardless of what mechanism is used to hypothesize (local) monotonicity relations between points in image space, it is still necessary to embed that mechanism in a computation to achieve global constraint. The implementation approach taken here is somewhat ad hoc. The program selects nine points in a simple 3 x 3 square pattern as its basic set of (closely spaced) image points. This pattern serves as the set $I_1, I_2, \ldots, I_n$ for applying the local constraint criteria (Rules I and II). First, however, the set $I_1, I_2, \ldots, I_n$ is passed to the chosen hypothesizing routines to be (partially) ordered with respect to view angle and direction of steepest descent. The reflectance map $R(p,q)$ is then used to determine the initial contour of possible gradient space locations for each point I_i. Rules I

and II are iteratively applied to these contours until no further mutual constraint is provided.

The above describes the basic application of local constraint to each 3 x 3 template. The selection of successive 3 x 3 square patterns is allowed to overlap. Thus, each image point I_i will eventually belong to nine templates. Each time a particular image point I_i is further constrained by the application of local constraint to a template of which it is a member, each of its eight other templates is marked for reconsideration. Before moving on to a previously unconsidered template local constraint is applied iteratively to each marked template, with additional marking added as required, until no marked templates remain to be reconsidered. Each time an image point I_i is considered, any additional constraint on the gradient space contour of possible solutions to the basic equation $I(x,y) = R(p,q)$ propagates through this local filtering mechanism to all other image points under consideration.

The next issue to arise is the question of how to terminate the growth of templates. Currently, the program terminates on one of two conditions:

1. One or more of the image points under consideration has no admissable gradient space interpretation. This means the algorithm can no longer assign surface orientations to image points consistent with the hypotheses about surface curvature used to generate the (partial) orderings with respect to changes to view angle and changes to direction of steepest descent. In this case, the "forced" interpretation is deemed to have failed.

2. Any new templates will cross either a contour of range discontinuity (OCCLUSION boundary) or a contour of discontinuity of surface normal (CONVEX or CONCAVE edge). OCCLUSION boundaries are detected by noting when boundary points to existing templates have a view angle greater than some preassigned value. (That is, e is approaching $\pi/2$). CONVEX or CONCAVE edges, on the other hand, can not be detected while templates are being expanded. Unless external knowledge is provided about the existence of such edges, templates will propagate across discontinuities in surface normal. Depending on the nature of the discontinuity, it may lead to failure due to condition 1 above or it may never be noticed.

2.8 AN ILLUSTRATIVE EXAMPLE

Consider the simple example of a "Lambertian" sphere illuminated by a single distant light source. The intensity space to gradient space correspondence will be derived analytically and then it will be used as a basis for judging the performance of the algorithm.

The first task is to determine the reflectance map. To do this, a surface photometric function must be specified. The term Lambertian refers to a phenomenological model of a perfect diffuse reflector such that the surface appears equally bright from all viewing directions. For such a surface, the intensity recorded in an image depends only on the foreshortening effect of the varying angle of incidence. In particular, the surface photometric function $\phi(i,e,g)$ is given by:

$$\phi(i,e,g) = k \cos(i)$$

Since image intensity is to be normalized with respect to the reflectance map, one can, without loss of generality, let k = 1. Thus, this surface photometric function can be transformed into a reflectance map R(p,q) by simply recalling the expression derived earlier for cos(i). The reflectance map R(p,q) is given by:

$$R(p,q) = \frac{1 + pp_s + qq_s}{\sqrt{1 + p_s^2 + q_s^2}\ \sqrt{1 + p^2 + q^2}}$$

The second task is to determine the surface orientation of each image point. In the example, this result is particularly easy to obtain. Let the object sphere be centered at the origin and have radius r. Then, the equation of the sphere is given implicitly by:

$$x^2 + y^2 + z^2 = r^2$$

Elementary calculus will verify that the vector (x,y,z) defines an (outward) normal at each point (x,y,z) on the surface. The appropriate gradient is obtained by rewriting this normal as (-x/z,-y/z,-1). For each (x,y), there are actually two possible z values to be considered. Note, however, that with the viewer looking in the direction of the positive z-axis, the hemisphere actually in view corresponds to negative values of z (recall figure 2-3(b)). Thus, the equation of the sphere is also given explicitly by:

$$z = -\sqrt{r^2 - x^2 - y^2}$$

The parameters of the image forming system can be factored out by assuming that the image I(x,y) has been normalized to the corresponding reflectance map R(p,q). In this case, the intensity synthesized for each image point (x,y) is equal to the value of the reflectance map at the corresponding (p,q). Thus, the equation for image intensity is:

$$I(x,y) = R(-x/z,-y/z) \text{ where } z = -\sqrt{r^2 - x^2 - y^2}$$

Finally, the mechanism by which monotonicity relations were hypothesized for this example must be specified. One additional assumption was used. The algorithm assumes that it knows at least one image point corresponding to an object point oriented directly facing the viewer. Now, let such a point define a *pseudo-origin* in image space. Since the view angle is assumed to be zero at the pseudo-origin, the only possible interpretation is that, in a particular direction, the view angle is locally non-decreasing with increasing image distance from the pseudo-origin. In general, one can not hope to assert any local monotonicity relation on direction of steepest descent based on angular position about the pseudo-origin. If, however, the surface is known to be convex, the direction of steepest descent is (locally) non-decreasing with increasing angular position about the pseudo-origin. For the example, the set of image points $I_1, I_2, \ldots, I_n$ was ordered in view angle according to their distance in image space from the pseudo-origin and ordered in direction of steepest descent according to their angular position about the pseudo-origin. Applied together, these hypotheses are equivalent to the strong assumption that the surface in question is a convex solid of revolution (with the axis of revolution in the direction of the view vector).

For the example, $p_s = 0.7$, $q_s = 0.3$ and $R = 60$. A 128 x 128 synthesized image was considered (where $-64 \leq x \leq 63$ and $-64 \leq y \leq 63$). The algorithm was applied to this image using 3 x 3 square templates sampled at an image spacing of 5 points (in both X and Y). The pseudo-origin was defined as $x = 0$ and $y = 0$. The results are first presented as a series of figures. Figure 2-6 is the synthesized image. Figure 2-7 shows the points in gradient space corresponding to the sampled

image points. Figure 2-8 shows the reflectance map $R(p,q) = \cos(i)$ drawn as a series of contours (spaced 0.1 units apart). Figure 2-9 redraws figure 2-7 but with the gradient points corresponding to the self-shadowed portion of the sphere excluded. (All gradient points to the left of the contour $R(p,q) = 0$ correspond to surface points oriented more than 90^0 away from the direction of incident illumination.)

Figure 2-10 shows the restricted subsection of contour determined by the algorithm for each sampled point of figure 2-6. Finally, figure 2-11 superimposes the correct gradient point on each subsection of contour of figure 2-11 to illustrate how well the algorithm has performed. The crosses mark the correct gradient points, determined analytically, while the corresponding subsection of contour marks how well the algorithm has isolated those points.

2.9 DISCUSSION

How well did the algorithm perform on this example? To answer this question, the freedom remaining in each subsection of contour C_i can be examined. This freedom has been measured in two ways.

First, since each point in gradient space defines a surface orientation, the maximum angle subtended between points remaining in the gradient contour C_i can be measured. Define the angular spread in surface orientation at image point I_i as:

$$\max\{\theta \mid \cos(\theta) = \frac{(p_i, q_i, -1)\cdot(p_j, q_j, -1)}{|(p_i, q_i, -1)||(p_j, q_j, -1)|} \text{ and } (p_i, q_i), (p_j, q_j) \in C_i\}$$

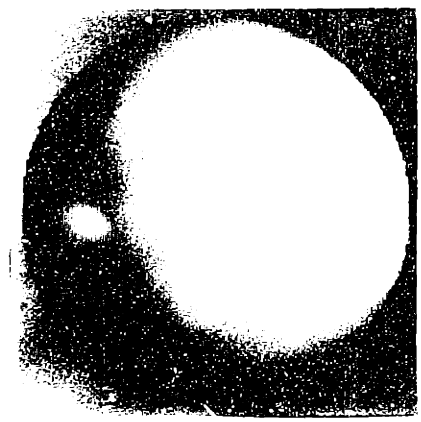

Figure 2-6 The synthesized image of a sphere. The surface reflectance is assumed to be Lambertian with the light source placed at gradient point $p_s = 0.7$ and $q_s = 0.3$.

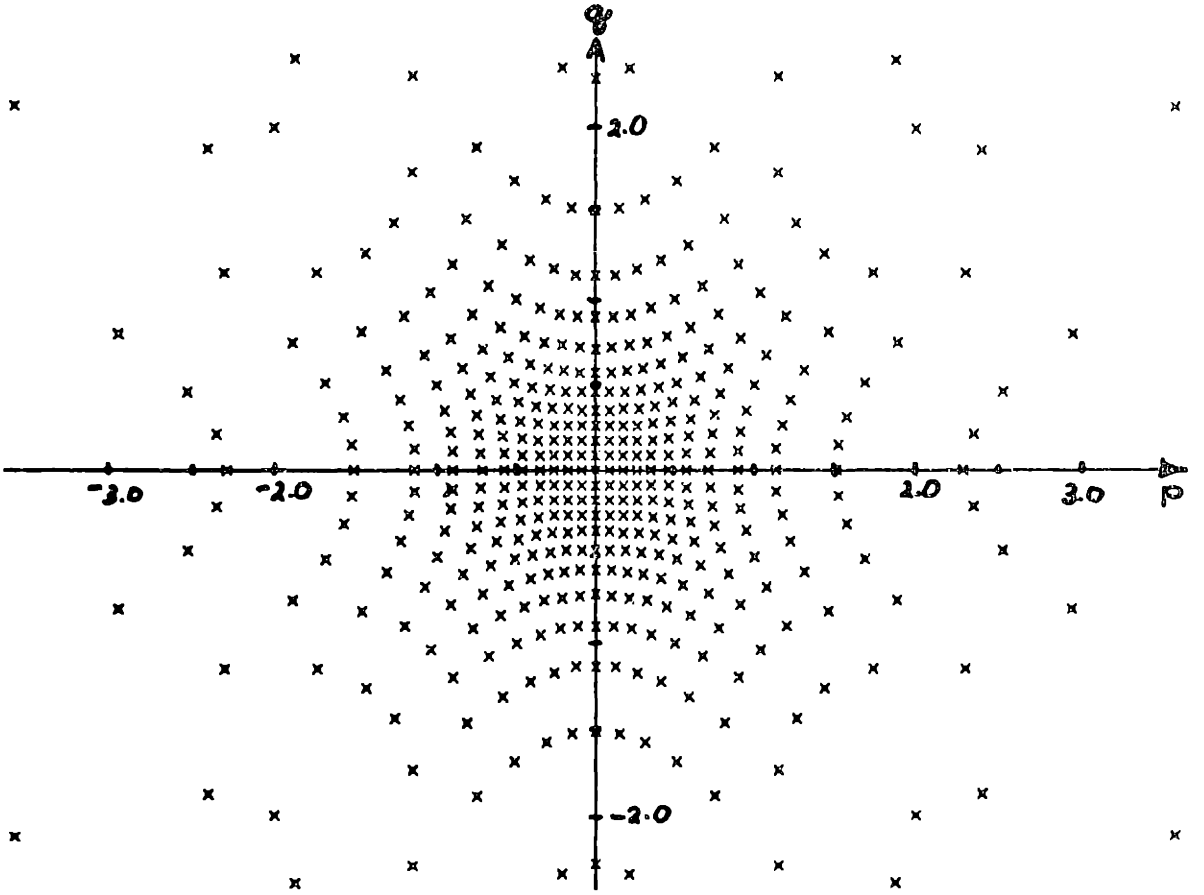

Figure 2-7 The points in gradient space corresponding to the sampled image points (determined analytically).

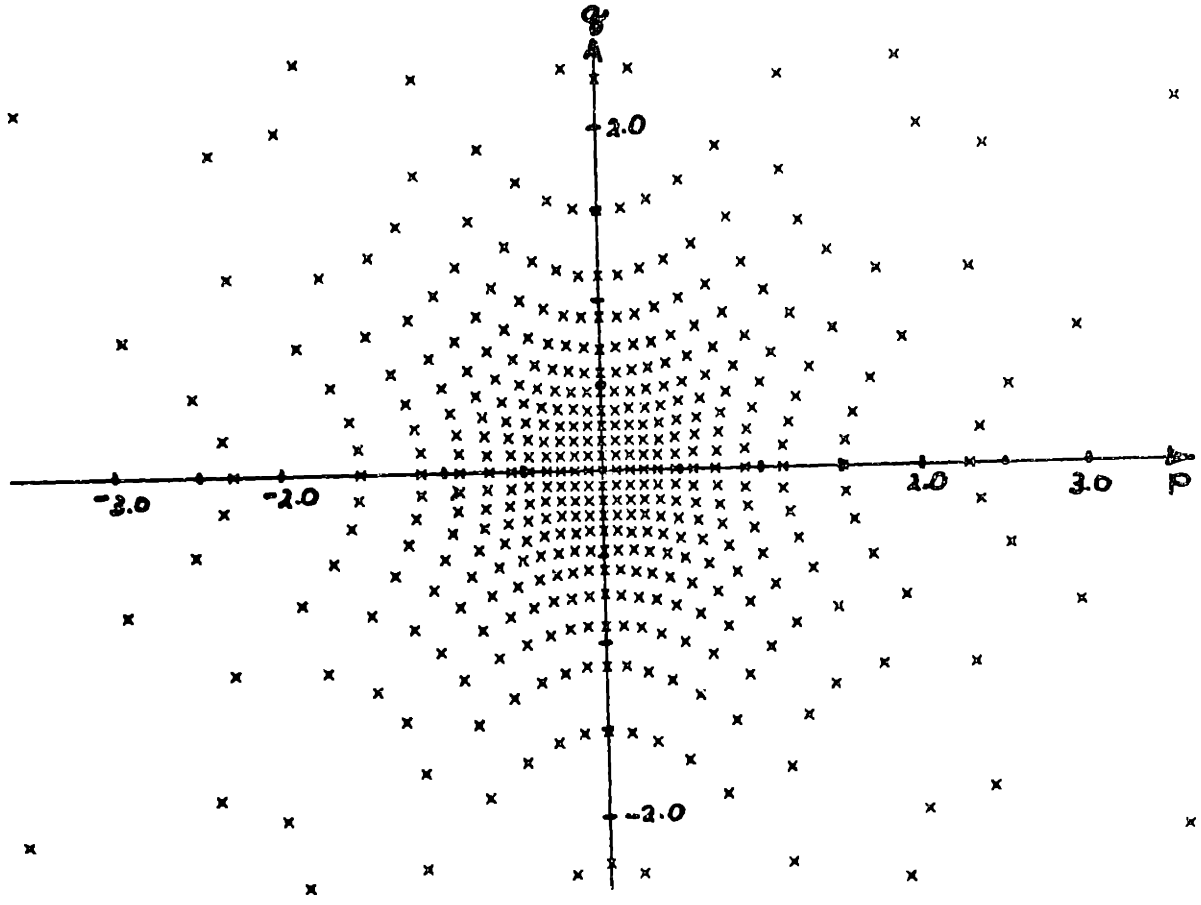

Figure 2-7 The points in gradient space corresponding to the sampled image points (determined analytically).

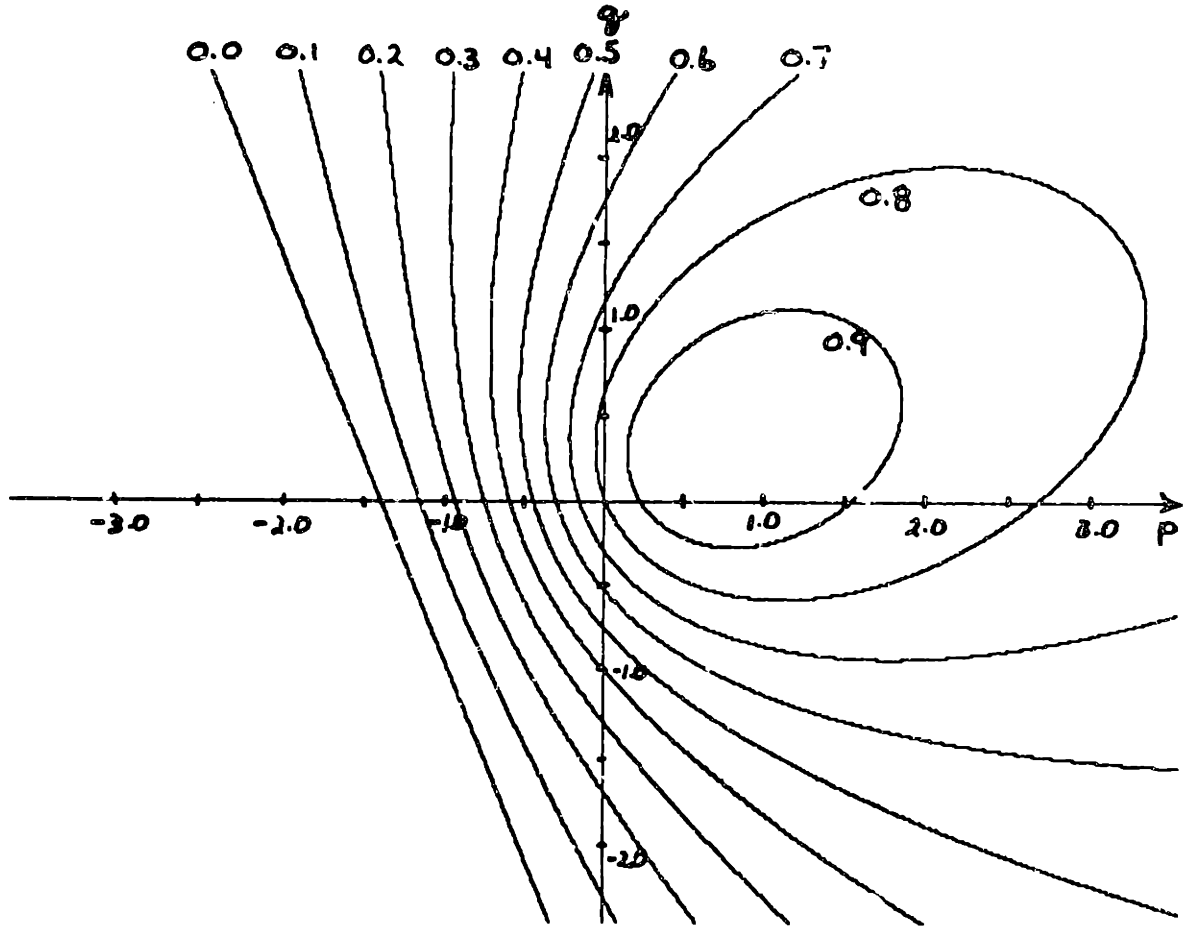

Figure 2-8 The reflectance map for a Lambertian surface illuminated from gradient point $p_s = 0.7$ and $q_s = 0.3$ plotted as a series of contours (spaced 0.1 units apart).

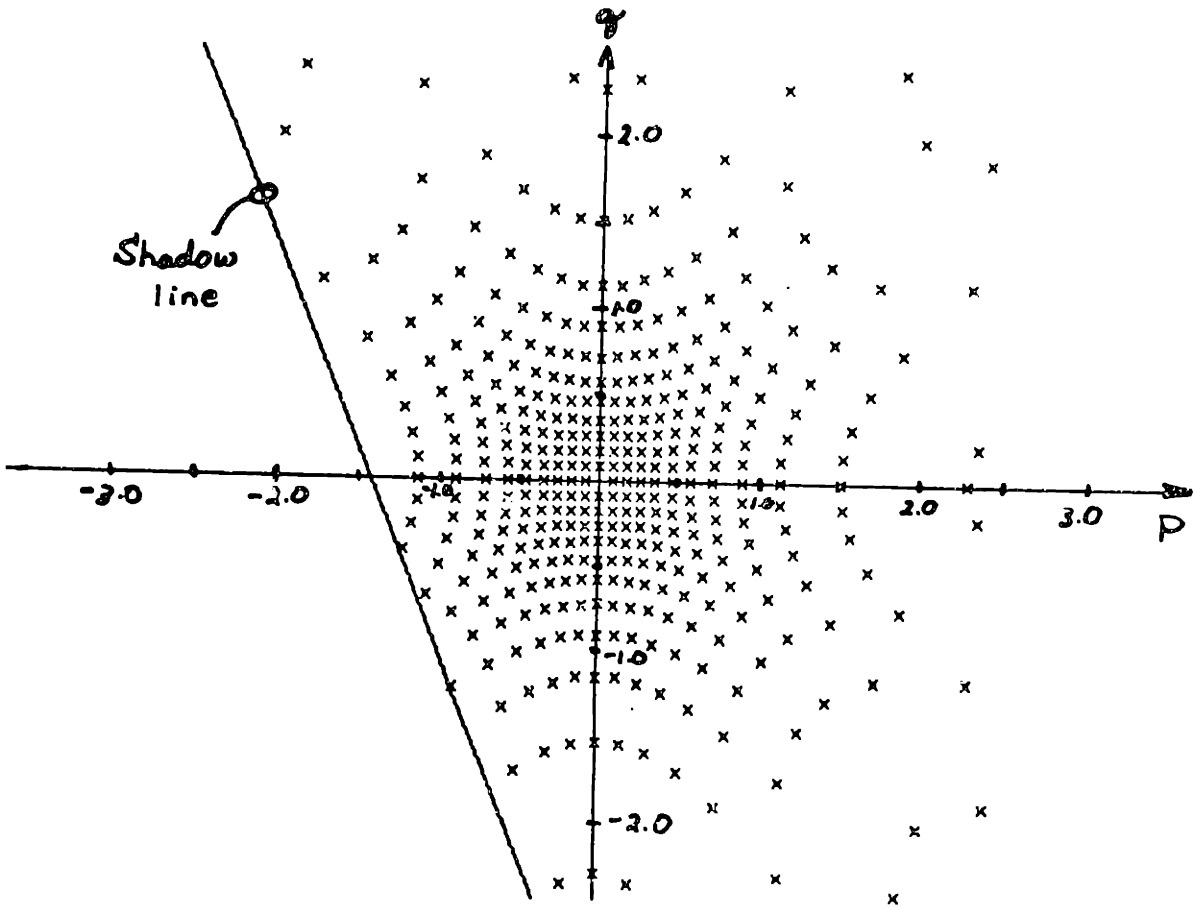

Figure 2-9 The points in gradient space corresponding to sampled image points which are illuminated by the light source (ie. image points corresponding to object points with $i < \pi/2$).

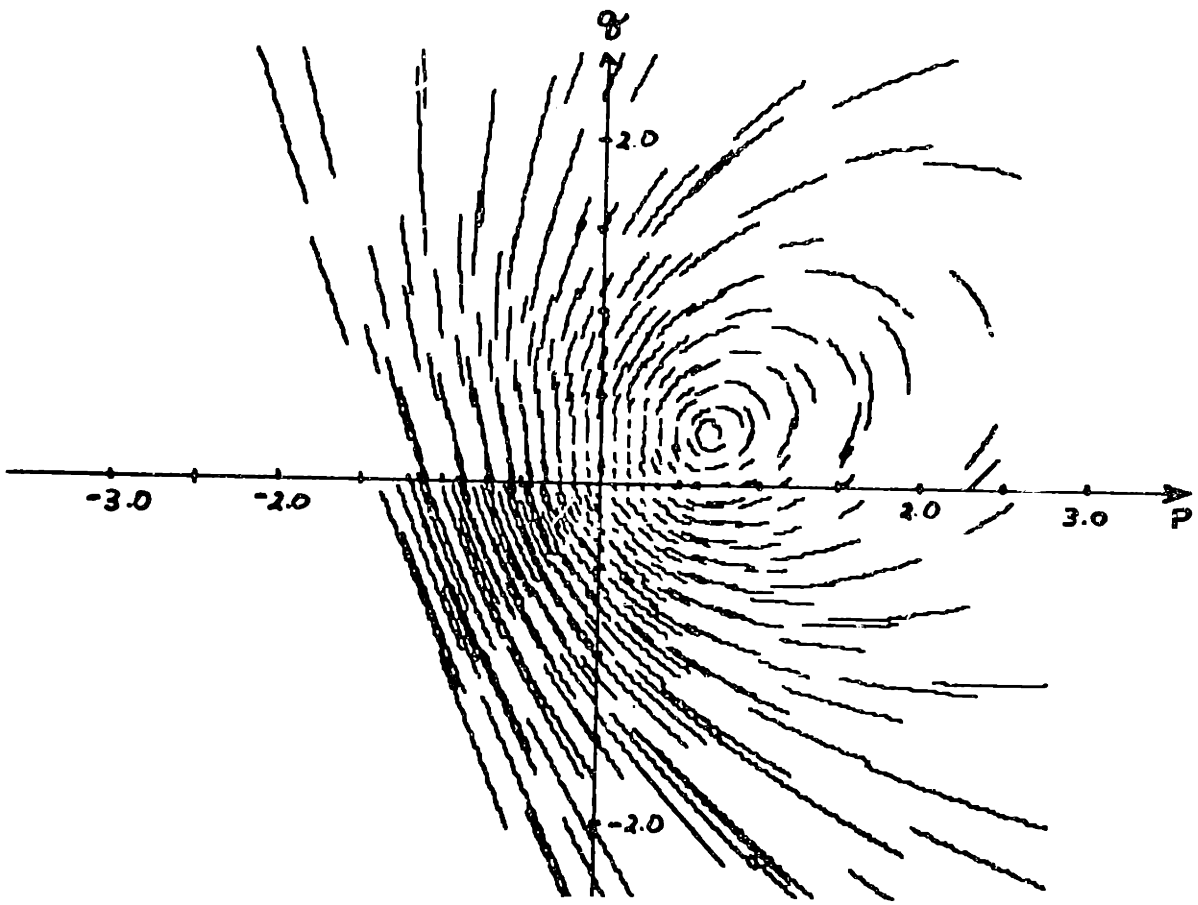

Figure 2-10 The restricted subsection of contour determined for each sampled image point.

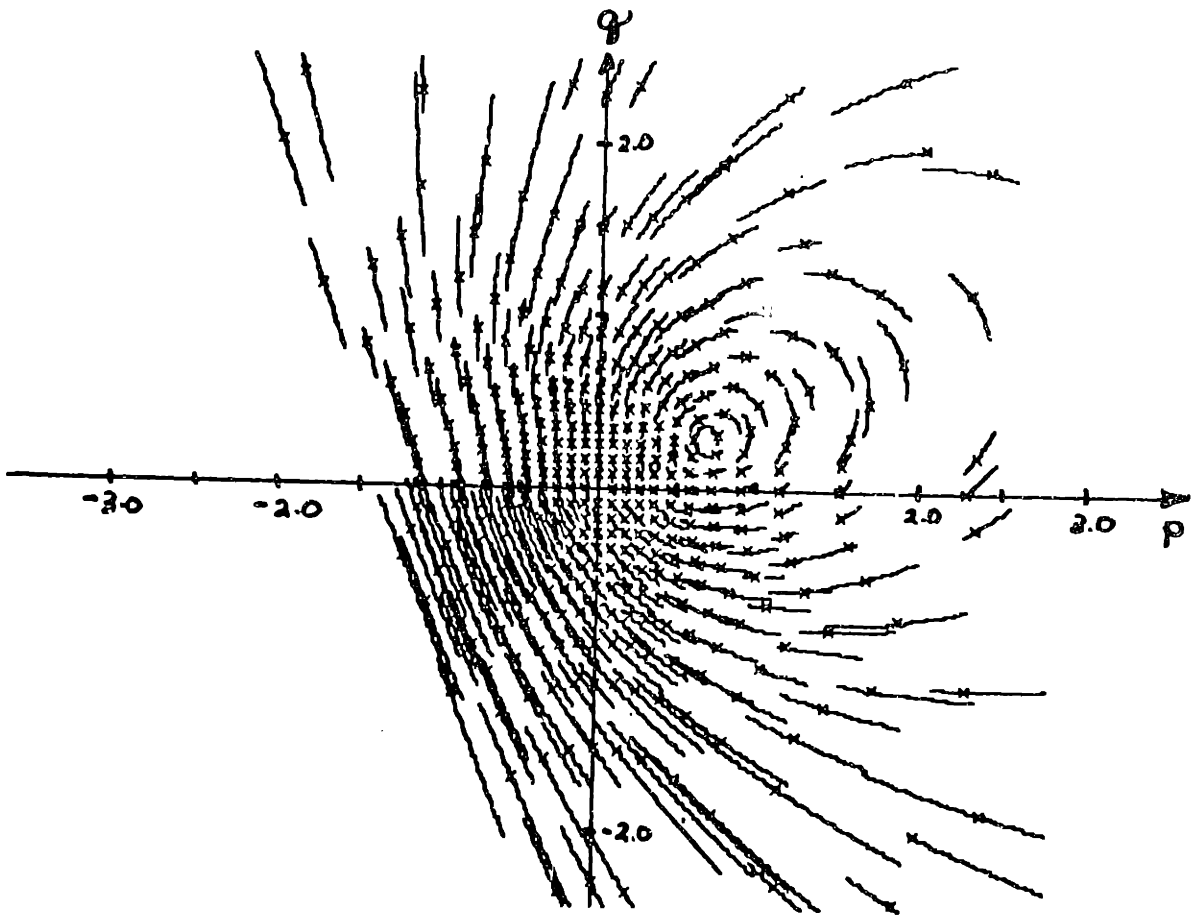

Figure 2-11 The superposition of figure 2-9 and figure 2-10. Crosses mark the exact gradient points (determined analytically) while each subsection of contour marks how well the program has determined that point.

Second, define the angular spread in view angle e at image point I_i:

$$\max\{(e_1-e_2) \mid \tan(e_1)=\sqrt{p_1^2+q_1^2}, \tan(e_2)=\sqrt{p_2^2+q_2^2} \text{ and } (p_1,q_1),(p_2,q_2)\in C_i\}$$

Note: view angle is useful because it determines the degree of surface forshortening at each image point. Knowing the view angle, one can calculate the area of surface equivalent to a given area of image.

To tabulate the results, the sampled image points were split into two classes. First, consider all sample points within 45° view angle (i.e., lying within gradient space circle $p^2 + q^2 = 1$). Second, consider all sample points within 60° view angle (i.e., lying within gradient space circle $p^2 + q^2 = 3$). Table 2-1 summarizes the results:

	Points Within 45° View Angle	Points Within 60° View Angle
Surface Orientation:		
Mean Angular Spread	8.9°	9.9°
Standard Deviation	6.1°	7.0°
Best Case	0.5°	0.5°
Worst Case	36.3°	41.7°
View Angle:		
Mean Angular Spread	4.7°	5.0°
Standard Deviation	2.4°	2.5°
Best Case	0.5°	0.5°
Worst Case	10.9°	11.9°

TABLE 2-1

Note that these measures refer to total angular spread. If a choice algorithm is adopted which selects the "correct" answer to be at the midpoint of the angular spread, this choice is guaranteed to be no more than half the angular spread in error. Thus, the upper right portion of table 2-1 can be interpreted as follows:

> *On the average, by sampling at an image spacing of 5 points in X and Y, the algorithm was able to position image points, corresponding to surface points less than 60° in view angle, to within 5° of their true orientation in space. The standard deviation of this measure over all such points was 3.5° while the worst case point was located to within 21° of its true orientation in space.*

Why did the algorithm not do better? The performance of the algorithm depends critically on three factors: the ability to hypothesize monotonicity relations between selected image points, the nature of constraint propagation and the topography of the reflectance map. Hypothesis based mechanisms are always faced with a chicken and egg dilemma. If one has no *a priori* constraint on object curvature, one can say nothing about ordering image points with respect to changes in view angle and changes to direction of steepest descent. On the other hand, the more constraint on object curvature, the more reliably one can order image points with respect to changes in view angle and changes to direction of steepest descent. The discussion of convexity gives some indication of how one can use general *a priori* assumptions about surface geometry to specify monotonicity relations. In the next chapter, situations are explored in which additional physical constraint can be exploited to simplify image analysis.

But, in the example above, the hypothesis mechanism used was guaranteed always to order (totally) each of the nine template points. Still, the algorithm did not pin down each gradient point exactly. In some sense, it ought to have. (For a solid of revolution, with axis of rotation about the view vector, the direction of steepest descent at each image point is given by $\theta = \tan^{-1}(y_p/x_p)$ where (x_p, y_p) is a pseudo-origin as defined above.) The algorithm propagates constraint by casting away sections of contour that are inconsistent with the current hypothesis

criteria. If the hypothesis criteria are valid, the algorithm will never cast away a correct solution to the equation $I(x,y) = R(p,q)$. On the other hand, this does not imply that each point remaining on a subsection of contour is a possible solution to the equation $I(x,y) = R(p,q)$ consistent with the current hypothesis criteria. The algorithm, as implemented, does no point by point analysis. Any case analysis is a risky business in a numerical algorithm which is, in principle, dealing with a continuous rather than discrete domain. The ability to achieve a tight global constraint is, unfortunately, related to the ability to achieve a tight local constraint. This, in turn, is related not just to the success of the hypothesis mechanism but also to the topography of the reflectance map.

In the example, surface orientation was most poorly constrained in the third and fourth quadrants of gradient space. In the third quadrant, the reflectance map contours locally approximate sections of circles centered at gradient space origin. Here, view angle is tightly constrained but the shape of the reflectance map contours provides little constraint on direction of steepest descent. In the fourth quadrant, the reflectance map contours locally approximate radial lines emanating from the gradient space origin. Here, the direction of steepest descent is tightly constrained but the shape of the reflectance map contours provides little constraint on view angle.

The topography of a reflectance map is determined by two factors: the surface photometry of the surface being viewed and the light source, object surface and viewer geometry. In general, one would not expect to have much control over the surface photometry of the objects being viewed. In principle, however, one is free to vary the light source geometry to achieve optimal results with the algorithm. This idea is the basis for the

method of photometric stereo which determines surface orientation using multiple images taken under the same object surface and viewer geometry but with different light source positions (see Chapter: 3.4).

The notions of local surface orientation, gradient space and the reflectance map are important tools for image analysis. The beauty of the gradient space formulation is that it allows physical constraints on the object surface to be expressed as simple geometric constraints on the gradient space contour of possible solutions to the image forming equation $I(x,y) = R(p,q)$. The algorithm discussed in this chapter provides a simple mechanism for propagating these geometric constraints.

3. EXPLOITING ADDITIONAL CONSTRAINT

In this chapter, situations are considered for which known physical properties of the object surface can be used to simplify the image analysis problem. Earlier, it was demonstrated how convexity and concavity constrain the possible matches between image points and their corresponding gradient points. Here, this analysis is extended to explore situations in which additional physical properties of the object surface can be exploited in image analysis. Finally, a method is presented for determining surface orientation which exploits the additional information provided from a second image taken with the same object surface and viewer geometry but with varying light source position.

This chapter serves three functions. First, the results developed here will deepen the theoretical foundation for the problem of interpreting image intensities. Second, since many surfaces occurring in industrial parts design and manufacture are also constrained by the assumptions introduced here, the results developed in this chapter are of immediate practical importance to the parts inspection problem. Third, an initial attempt is made to relate the image analysis problem to a higher level representation of object shape. In particular, an attempt is made to relate the results developed here to the generalized cone representation of <Agin & Binford 73>, <Marr 76a>, <Marr 77>.

Elsewhere, Horn has considered situations in which special properties of the surface photometric function can simplify image analysis <Horn 75>,<Horn 77a>. For example, the material of the maria of the moon (and of other rocky, dusty objects) when viewed from great distances has a surface photometric function which is constant for constant cos(i)/cos(e). This results in a reflectance map whose contours of constant R(p,q) are a

family of parallel straight lines. This results in a great simplification to the image analysis problem since the base characteristics become a predetermined family of straight lines, independent of the particular surface topography. (See Appendix: A.1 for a brief summary of Horn's method.)

This chapter presents a complementary study. Horn considered simplifications due to the special properties of certain surface photometric functions. These properties constrain the reflectance map. Here, an arbitrary reflectance map is allowed. Instead, simplifications are considered which arise from special properties of surface curvature. These properties constrain surface topography.

3.1 SURFACES WITH CONSTANT IMAGE HESSIAN

The purpose of this section is to examine the case for which the image Hessian matrix H is constant. This is important for two reasons. First, if indeed the Hessian matrix H is constant throughout a region of the image, then local information gathered about the Hessian becomes global to that region. This fact allows one to combine local evidence about the Hessian and determine it completely. Second, using the assumption that H can be considered constant over a small (enough) region of the image, one can use the intensity values present in that region to define a "best fit" approximation to the curvature of the surface over that region.

Throughout this work, an effort has been made to stress the fact that the reflectance map ought not be thought of as an image but rather as a convenient representation of how surface orientation determines intensity values for a particular object material and object surface, light source and viewer geometry. This is the one section of the thesis in which the

reflectance map will be treated as an image. Thinking of it this way will help motivate the analysis to follow.

For the reflectance map to be an image of some object, its surface must satisfy the two differential equations:

$$p = \frac{\partial f(x,y)}{\partial x} = x$$

$$q = \frac{\partial f(x,y)}{\partial y} = y$$

The (family of) paraboloids

$$z = \frac{x^2 + y^2}{2} + C \qquad (3.1.1)$$

satisfy the two differential equations. For these surfaces, the basic image forming equation becomes:

$$I(x,y) = R(p,q) = R(x,y)$$

Thus, the reflectance map may be thought of as the image of a paraboloid. As a first observation, this suggests that a paraboloid would make an ideal calibration object for empirically determining a reflectance map. Actually, a sphere, which is generally easier to come by, serves almost as well if one is willing to live with a loss of accuracy as the viewing angle increases.

For present purposes, it is not so much of interest that the reflectance map is the image of a paraboloid, but rather that, for such a surface, the image Hessian matrix H is constant. Indeed, for the family of paraboloids described by (3.1.1), The Hessian matrix H is the 2 x 2 identity matrix. In general, in order to have a constant Hessian H, a surface with explicit representation $z = f(x,y)$ must have no terms of higher than second order (in x and y). That is, the surface can be described by the form:

$$z = Ax^2 + By^2 + 2Cxy + Dx + Ey + F \qquad (3.1.2)$$

The corresponding Hessian becomes:

$$H = 2\begin{bmatrix} A & C \\ C & B \end{bmatrix}$$

To rule out degenerate situations, assume that the surface described by (3.1.2) is fully second order. That is, assume $AB - C^2 \neq 0$. (This assumption guarantees that H is nonsingular.) Subject to this assumption, (3.1.2) describes either an elliptic paraboloid or a hyperbolic paraboloid.

Suppose, first, that the surface in view is of the form (3.1.2). In order to determine the image Hessian matrix H, it is sufficient to determine the movement in gradient space corresponding to two linearly independent movements in the image. Suppose that an image point (x_o, y_o) is known to correspond to the gradient point (p_o, q_o). If [dx,dy] is chosen to be in the direction $[R_p, R_q]$, then the corresponding [dp,dq] is in the direction $[I_x, I_y]$ (see Appendix: A.1). This gives one piece of information about the Hessian matrix H. This information is the basis for Horn's method of characteristic strip expansion <Horn 75>, <Horn 77a>. As a characteristic strip is expanded, additional pieces of information are obtained. In general, these pieces of information can not be combined since the Hessian itself changes along the characteristic strip. But, if the surface is of the form (3.1.2), then these pieces can be combined.

For most regions of a reflectance map, the direction defined by $[R_p, R_q]$ does not change very rapidly along a characteristic strip. Nevertheless, it does not require much change to determine H to high accuracy. But, nota a paradox. The situation in which Horn's method achieves its greatest simplification (i.e., lunar topography) is the

situation for which the base characteristics are predetermined *straight lines* in the image. If, in fact, the base characteristics are straight lines then it will never be possible to obtain linearly independent movements in the image by characteristic strip expansion! In such a case, it is not possible to say anything about how H behaves in directions other than the direction defined by the base characteristic (even in the cases for which H is constant over the whole image). Thus, in some sense, the ability to approximate the Hessian H locally at an image point (x_0,y_0) is related to the curvature of the base characteristic passing through (x_0,y_0). If the base characteristic has high curvature at (x_0,y_0) then good conditioning (with respect to linear independence) is achieved between closely spaced image points (i.e., over areas in the image where the approximation of constant H is likely to be a resonable one).

There are two factors which act together to determine how the image Hessian matrix H maps a (small) movement [dx,dy] in the image into the corresponding movement [dp,dq] in gradient space. First, in moving from an image point (x_0,y_0) to an adjacent point (x_1,y_1) there is a change in local surface orientation due to an actual change in the object curvature. Second, because the object surface is viewed obliquely, the rate of change in local surface orientation can appear arbitrarily expanded due to the foreshortening of the surface in image projection. Fortunately, it is possible to decouple object curvature from the surface foreshortening induced by the view angle e.

If an image point (x,y) is known to correspond to the gradient point (p,q), then the Hessian matrix H at (x,y) can be written as the matrix product:

$$H = 1/\cos(e)\begin{bmatrix} p^2+1 & pq \\ pq & q^2+1 \end{bmatrix} C \qquad (3.1.3)$$

where the matrix C is given as:

$$C = \begin{bmatrix} \cos(\alpha) & -\sin(\alpha) \\ \sin(\alpha) & \cos(\alpha) \end{bmatrix} \begin{bmatrix} 1/r_1 & 0 \\ 0 & 1/r_2 \end{bmatrix} \begin{bmatrix} \cos(\alpha) & \sin(\alpha) \\ -\sin(\alpha) & \cos(\alpha) \end{bmatrix} \qquad (3.1.4)$$

The first two terms of the right-hand side of equation (3.1.3) account for the "distortion" in H due to the oblique viewing angle e. The first term can be interpreted as due to area foreshortening. The second can be interpreted as due to path length foreshortening (see Appendix: A.5 for details). The matrix C, given by equation (3.1.4), describes the two principal curvatures associated with the object surface $z = f(x,y)$. The values r_1 and r_2 are the two principal radii of curvature of the object surface at (x,y) and α is the direction (in the image) corresponding to the principal radius of curvature r_1. The direction corresponding to principal radius of curvature r_2 is orthogonal to α. Note that the values r_1 and r_2 are independent of the imaging geometry and depend only on the actual surface topography at (x,y). The matrix C corresponds to an object-centered definition of surface curvature while the matrix H corresponds to a viewer-centered definition of surface curvature. Equation (3.1.3) relates these two definitions of surface curvature.

Constraints on object curvature are constraints on the matrix C. Equation (3.1.3) must be used to translate any such constraints into equivalent constraints on H. Some idea of the effect of surface foreshortening can be seen by examining the structure of H in more detail. First, from (3.1.3) and (3.1.4) above, the determinant of H is given as:

$$\det|H| = \frac{1}{\cos^4(e)} \frac{1}{r_1 r_2}$$

Roughly speaking, H contains a "scale factor" of approximately $1/\cos^2(e)$ due to the oblique viewing angle e. More precisely, the product

$$1/\cos(e)\begin{bmatrix} p^2+1 & pq \\ pq & q^2+1 \end{bmatrix}$$

has eigenvalue $1/\cos^3(e)$ in the direction of steepest decent and eigenvalue $1/\cos(e)$ in the direction of the contour of constant e.

Elliptic and hyperbolic paraboloids are the (unique) surfaces for which the "increase" in H due to an increasing view angle e is precisely offset by the increase in r_1 and r_2 due to the changing object curvature.

3.1.1 APPROXIMATING THE IMAGE HESSIAN LOCALLY

Let us see how the assumption that H is constant over a small region of the image can be used to define a "best fit" approximation to the image Hessian at an image point (x,y) known to correspond to the gradient point (p,q). The basic observation used here is that multiplication by a constant H defines a 1-1 continuous mapping between a circle in the image centered at (x,y) and an ellipse in gradient space centered at (p,q) (see Appendix: A.3). If two linearly independent directions $[dx_1, dy_1]$ and $[dx_2, dy_2]$ and the corresponding $[dp_1, dq_1]$ and $[dp_2, dq_2]$ are known, then H is determined by:

$$H = \begin{bmatrix} dp_1 & dp_2 \\ dq_1 & dq_2 \end{bmatrix} \begin{bmatrix} dx_1 & dx_2 \\ dy_1 & dy_2 \end{bmatrix}^{-1} \qquad (3.1.5)$$

One correspondence can be tied down immediately. If $[dx,dy] = [R_p, R_q]$ then $[dp,dq] = [I_x, I_y]$. Thus, (3.1.5) can be rewritten as:

$$H = \begin{bmatrix} I_x & dp \\ I_y & dq \end{bmatrix} \begin{bmatrix} R_p & dx \\ R_q & dy \end{bmatrix}^{-1} \qquad (3.1.6)$$

Equation (3.1.6) still admits an infinite number of solutions. However, for any particular second choice [dx,dy], linearly independent from $[R_p, R_q]$, the geometric constraints developed in Chapter: 2.6 can be used to constrain the set of [dp,dq] that can correspond to the given [dx,dy]. Each [dp,dq] not eliminated by geometric constraint defines a possible solution to (3.1.6). For each possible solution, one can proceed to sample the intensity values along the image circle centered at (x,y) and of radius $ds = \sqrt{dx^2 + dy^2}$. For each point on this circle, the corresponding reflectance map value R(p+dp,q+dq), where $[dp,dq]^T = H\,[dx,dy]^T$, can also be sampled. The "best fit" Hessian at (x,y) is defined to be that choice of [dp,dq] which minimizes the least square error between the sampled intensity values and the corresponding sampled reflectance map values.

Consider an example. Suppose image point (x_0, y_0) is known to correspond to gradient point (p_0, q_0) on a section of surface assumed to be convex. Then, for a particular choice of ds, the image is sampled at the four points:

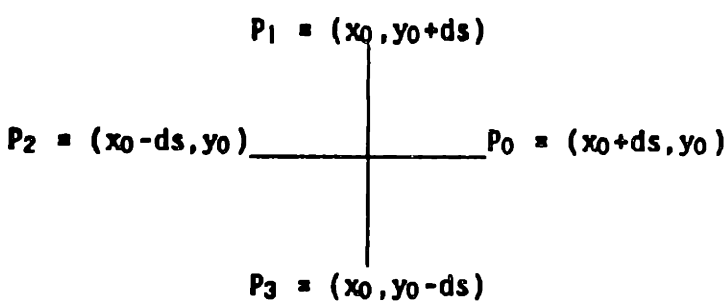

From the four intensity values thus obtained, the four reflectance map contours, corresponding to the four image points P_0, P_1, P_2 and P_3, are determined. (Note: if bounds on the eigenvalues of H are already known, then the range in gradient space used in the initial determination of the four reflectance map contours can be tightly constrained.) Figure 3-1 illustrates the four contours obtained for a particular choice of (x_0,y_0), (p_0,q_0) and ds (using the Lambertian sphere example of Chapter: 2.8) No *a-priori* constraint is assumed on the magnitude of the eigenvalues of H. Convexity allows us to assert the two inequalities:

$$I_x R_p + I_y R_q \geq 0$$

$$dxdp + dydq \geq 0$$

After applying these two inequalities to each of the four contours of figure 3-1, the constrained contours of figure 3-2 are obtained.

There is one additional constraint available. H defines a linear transformation. For the particular choice of P_0, P_1, P_2 and P_3 above, observe that the [dx,dy] used to move from (x_0,y_0) to P_0 is the negative of the [dx,dy] used to move from (x_0,y_0) to P_2. (Similarly, for P_1 and P_3.) Thus the corresponding [dp,dq]'s must be the negative of each other. In particular, the magnitude of the [dp,dq]'s must be equal and they must be π radians out of phase. Each point in the contour of possible (p,q) for P_0 which does not have a match in P_2 whose distance from (p_0,q_0) is the same and whose angular position with respect to (p_0,q_0) is π radians out of phase can be excluded. Similarly, each point in the contour of possible (p,q) for P_2 which does not have a match in P_0 whose distance from (p_0,q_0) is the same and whose angular position with respect to (p_0,q_0) is π radians out of phase can be excluded. (Note: these criteria must be applied somewhat conservatively otherwise all points will be excluded due to the

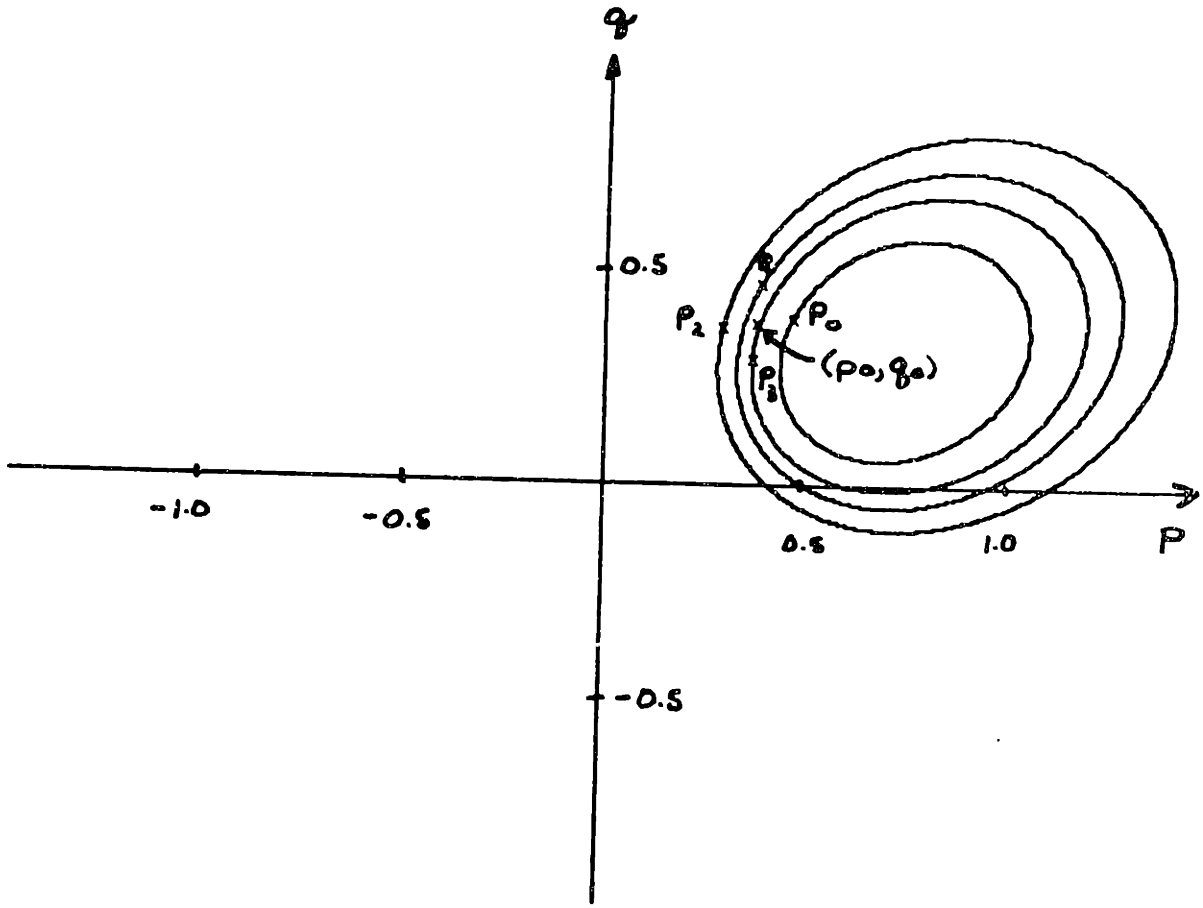

Figure 3-1 The four reflectance map contours P_0, P_1, P_2 and P_3 corresponding to the four sampled image points. Crosses mark the exact location of (p_0, q_0) and P_0, P_1, P_2 and P_3.

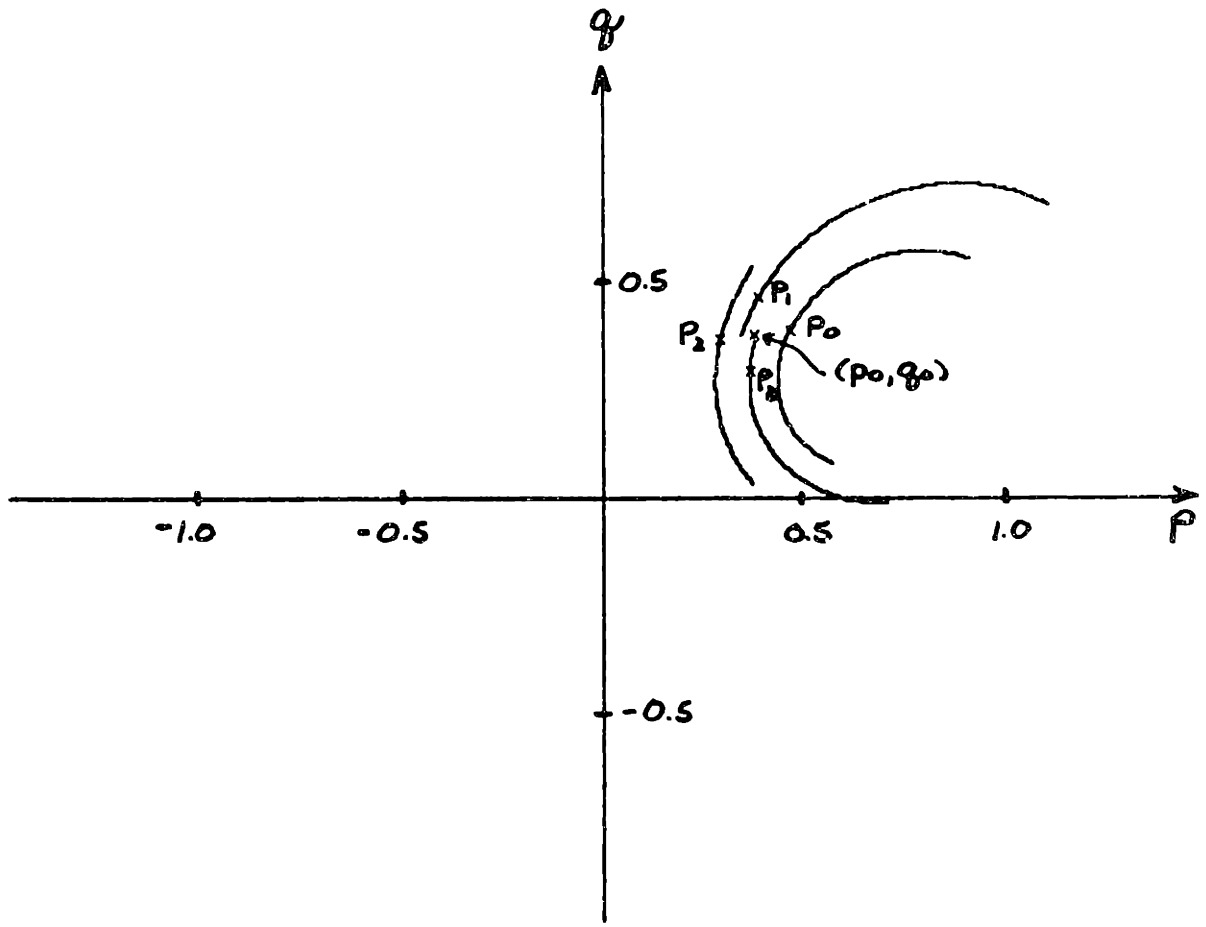

Figure 3-2 The restricted subsection of contour obtained if the section of surface under consideration is convex.

fact that H is not really constant.) The identical constraint holds between P_1 and P_3. Figure 3-3 shows the contour remaining when the above criteria are applied to exclude "obvious" bad matches.

Of the two pairs of contour, corresponding to P_0 and P_2 and to P_1 and P_3, select the pair that is closest to being $\pi/2$ radians out of phase with the direction $[I_x, I_y]$. (This choice is to guarantee superior conditioning in the estimation of H.) For each [dp,dq] remaining in the most highly constrained contour from the selected pair, use (3.1.6) to estimate H. Figure 3-4 shows the (family of) ellipses generated by the contour remaining for P_3. The vector superimposed on figure 3-4 points in the direction $[I_x, I_y]$. Figure 3-5 shows least squares "best fit" Hessian matrix at (x_0, y_0).

The "best fit" Hessian matrix of figure 3-5 has done a good job of solving for the curvature of the object surface at (x_0, y_0). It is important, however, to recall exactly what it is that has been computed. There are two assumptions underlying the computation. First, it is assumed that the Hessian matrix H is constant over the area in the image determined by the circle centered at (x_0, y_0) and of radius ds. Second, it is assumed that the gradient point (p_0, q_0) corresponding to image point (x_0, y_0) is known. Equation (3.1.3) tells how to choose ds to compensate for the foreshortening due to an oblique viewing angle e and thus achieve uniform sampling resolution over the entire surface. (Actually, a slightly more sophisticated scheme is required, since by sampling equally spaced points around the image circle, no matter what its radius, one is actually applying different weight to different directions along the surface.) The more serious restriction, however, is related to the second assumption. If the center of the ellipse has not been accurately positioned then a least

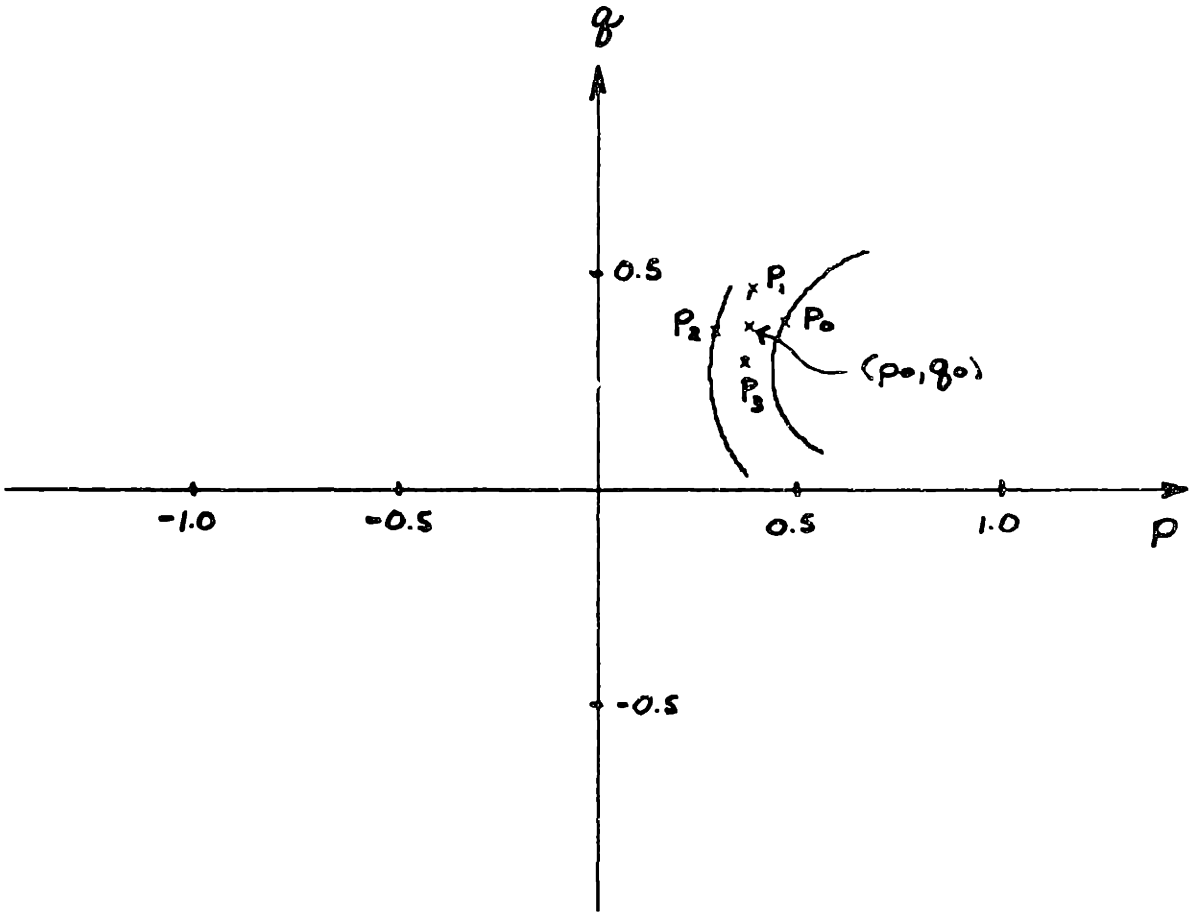

Figure 3-3 The restricted subsection of contour obtained when linearity is used to exclude "obvious" bad matches.

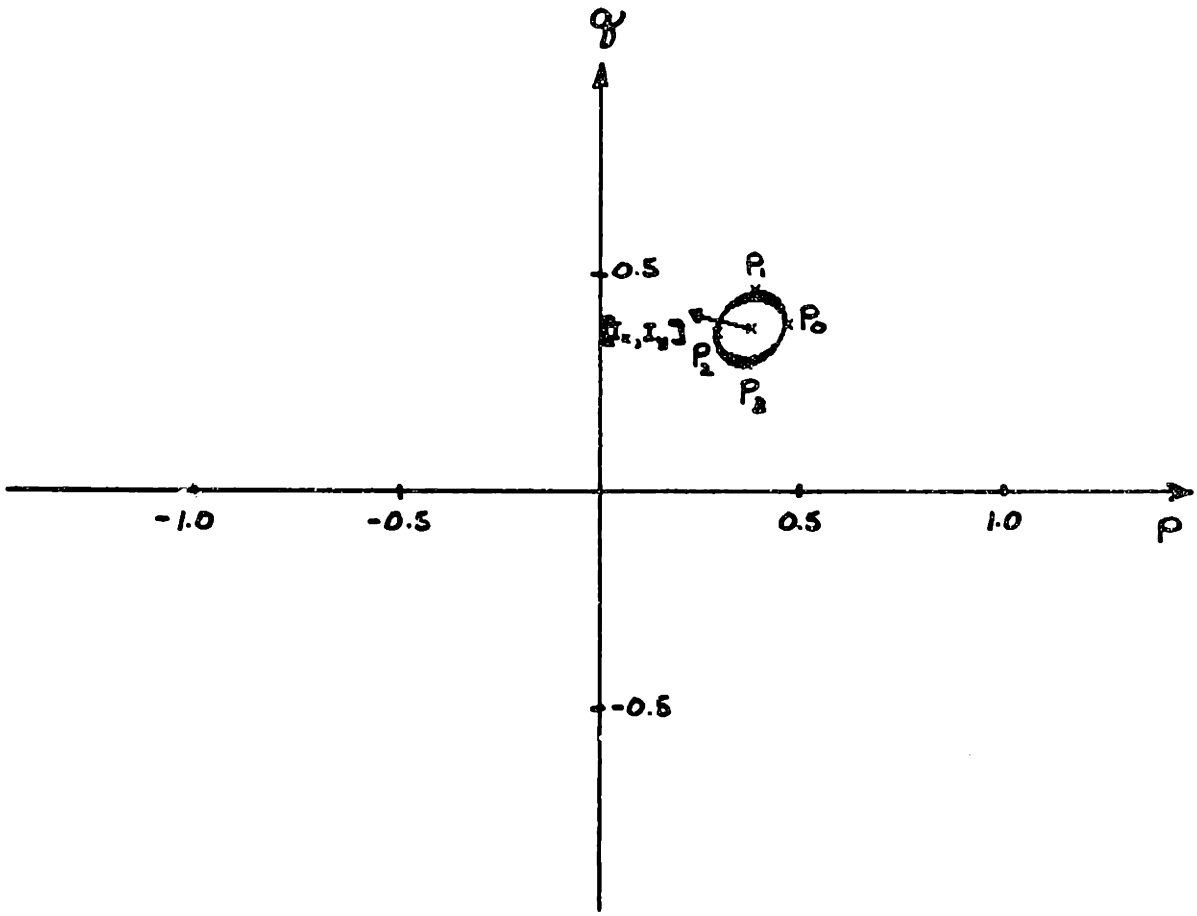

Figure 3-4 The (family of) ellipses which characterize the uncertainty remaining about the exact value of the image Hessian H. The vector at (p_0, q_0) is in the direction of the normal to the contour of constant intensity in the image at (x_0, y_0)

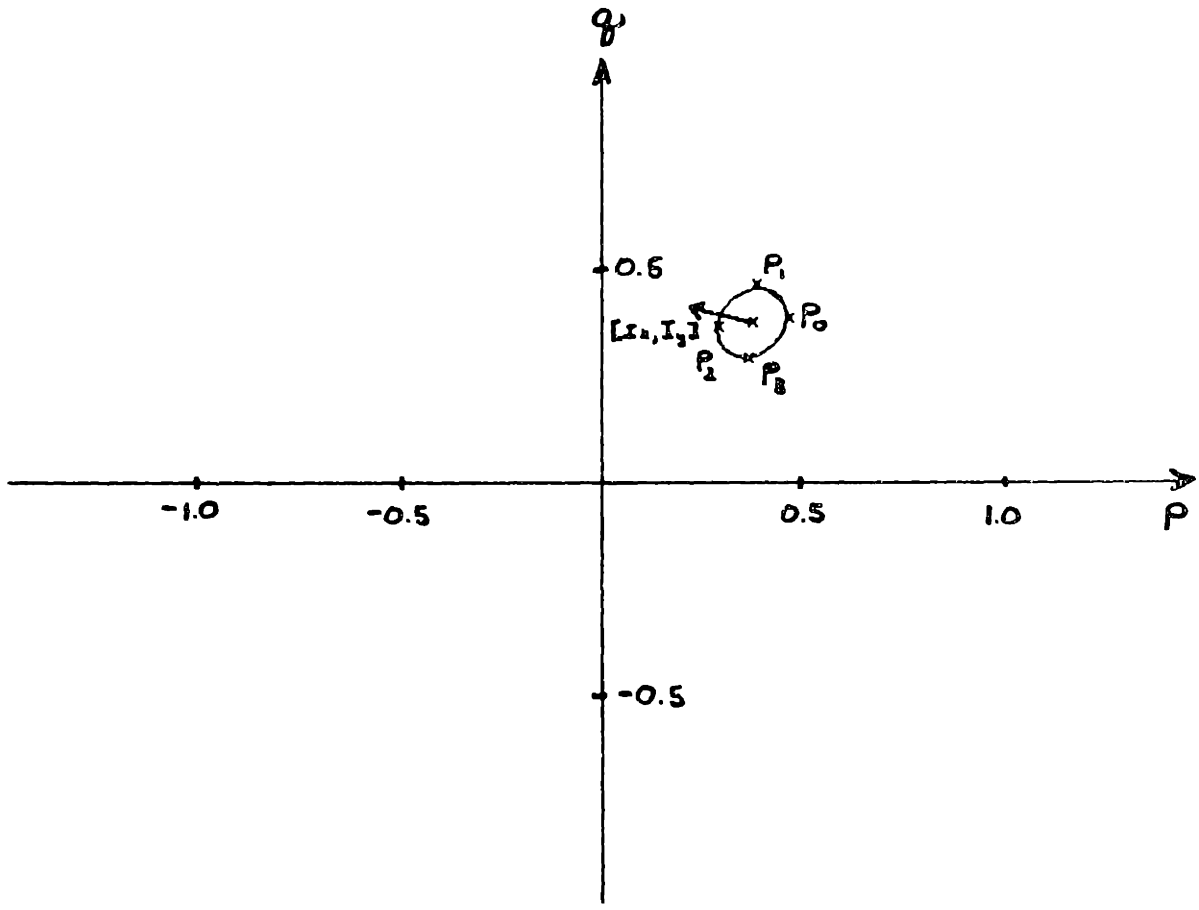

Figure 3-5 The ellipse corresponding to the "best fit" image Hessian at (x_0, y_0).

squares "best fit" is akin to groping around in the dark. This example illustrates not so much a useful method for finding the gradient points corresponding to a set of image points but the fact that the intensity values in an image can be used locally to constrain the behavior of the image Hessian matrix H in directions other than those defined by the current $[I_x, I_y]$.

3.2 SINGLY CURVED SURFACES

An important class of surfaces in differential geometry are those which have the property that, through every point on the surface, there passes at least one straight line lying entirely on it. Such a surface is called a *ruled surface*. The straight line lying entirely on the surface is called a *ruling*. If a ruled surface has the additional property that all points on a given ruling have the same tangent plane, then the surface is called a *developable surface* (or a *torse*). <Huffman 75> charmingly refers to developable surfaces as "paper" surfaces and proposes that such surfaces possess a complexity that is midway between that of a completely general surface and that of a plane surface. (See <Huffman 75> for an interesting characterization of properties of "paper" surfaces in terms of Gaussian curvature and the Gaussian sphere.)

Here, the notion of a singly curved surface is developed in terms of properties of the Hessian matrix H. Singly curved surfaces are shown to be equivalent to developable surfaces (except that a planar surface, while certainly developable, will not be considered singly curved). Finally, the image analysis of singly curved surfaces is discussed. The result will demonstrate that, from an image processing standpoint, singly curved surfaces do indeed possess a complexity that is between that of a

completely general surface and that of a plane surface.

> **Definition.** Let $z = f(x,y)$ describe a smooth surface and let λ_1 and λ_2 be the two eigenvalues of the corresponding Hessian matrix H at an image point (x_0,y_0). The surface is said to be *singly curved at* (x_0,y_0) if and only if exactly one of λ_1 and λ_2 is equal to zero. The surface is said to be *singly curved* if it is singly curved at each image point (x,y) on the surface.

This viewer-centered definition of a singly curved surface can be related to the object-centered principal radii of curvature. From equations (3.1.3) and (3.1.4) above, it can be shown that one of the eigenvalues λ_1 and λ_2 of H is zero if and only if one of the principal radii of curvature r_1 and r_2 is infinite (see also Appendix: A.5).

For surfaces expressed in the form $z = f(x,y)$, the equation:

$$\frac{\partial^2 f(x,y)}{\partial^2 x}\,\frac{\partial^2 f(x,y)}{\partial^2 y} = \left[\frac{\partial^2 f(x,y)}{\partial x \partial y}\right]^2 \qquad (3.2.1)$$

is the differential equation characterizing developable surfaces. In the current notation, this equation is equivalent to the equation:

$$\det|H| = 0 \qquad (3.2.2)$$

Equation (3.2.2) is satisfied at an image point (x,y) if and only if (at least) one of the eigenvalues of the corresponding H is zero at (x,y). Thus, (3.2.1) is satisfied for all surface points (x,y) if and only if (at least) one of the eigenvalues of H is zero at each image point (x,y). If both eigenvalues of H are zero for all image points (x,y), then the corresponding equation $z = f(x,y)$ describes a plane. For convenience, assume that at least one of λ_1 and λ_2 is non-zero at each image point (x,y). Thus, a non-planar surface $z = f(x,y)$ is developable if and only if

it is singly curved.

Let $z = f(x,y)$ be a singly curved surface. Suppose that a point (x_0,y_0) in the image is known to correspond to a point (p_0,q_0) in gradient space. Then, the Hessian matrix H at (x_0,y_0) is completely determined. Indeed, H is given as the matrix product:

$$H = \begin{bmatrix} \cos(\alpha) & -\sin(\alpha) \\ \sin(\alpha) & \cos(\alpha) \end{bmatrix} \begin{bmatrix} \lambda & 0 \\ 0 & 0 \end{bmatrix} \begin{bmatrix} \cos(\alpha) & \sin(\alpha) \\ -\sin(\alpha) & \cos(\alpha) \end{bmatrix} \qquad (3.2.3)$$

where

$$\lambda = \frac{\sqrt{I_x^2 + I_y^2}}{R_p \cos(\alpha) + R_q \sin(\alpha)}$$

and

$$\tan(\alpha) = \frac{I_y}{I_x}$$

As before, I_x and I_y denote the first partial derivatives of $I(x,y)$ at image point (x_0,y_0) and R_p and R_q denote the first partial derivatives of $R(p,q)$ at the corresponding gradient point (p_0,q_0).

Thus, given any initial image point (x_0,y_0) known to correspond to gradient point (p_0,q_0), the Hessian matrix of $z = f(x,y)$ at (x_0,y_0) is determined by (3.2.3). The Hessian matrix H so determined can then be used to find the new gradient corresponding to an arbitrary (small) movement [dx,dy] in the image according to the equation:

$$[dp,dq]^T = H\,[dx,dy]^T \qquad (3.2.4)$$

The operations embodied in (3.2.3) and (3.2.4) above can be iterated to trace out an arbitrary family of curves on the surface. For singly curved surfaces, one is not confined to tracing out the characteristics of Horn's original method for obtaining shape from shading information <Horn 75>, <Horn 77a>.

This result should not be terribly surprising. The fact that H has one zero eigenvalue means that there is one direction of movement in the image which results in no change to surface orientation. The orthogonal direction α is determined by the vector $[I_x, I_y]$. The component of any (small) movement [dx,dy] perpendicular to $[I_x, I_y]$ is in the direction of a ruling on the developable surface $z = f(x,y)$ and thus does not cause a change to the gradient (p,q). The component of [dx,dy] in the direction $[I_x, I_y]$ causes a change [dp,dq] to the gradient in the direction α where the "scale factor" for that change is given by the value of λ.

The points in gradient space corresponding to points on an arbitrary singly curved surface $z = f(x,y)$ are constrained to lie on a (one-dimensional) curve in gradient space. This is just another manifestation of the observation that singly curved surfaces possess a complexity midway between that of a plane surface (where surface points map into a single point in gradient space) and that of a completely general surface (where surface points map into a two-dimensional region in gradient space).

Figure 3-6 is the image of a right circular cone of base radius b and height h generated using the reflectance map of figure 2-8. (For this example, $h = 2b$.) It can be shown that the points in gradient space corresponding to points on a right circular cone lie on the (one-dimensional) curve in gradient space given parametrically by:

$$p = \tan(t) \tag{3.2.5}$$

$$q = \frac{b}{h} \frac{1}{\cos(t)} \tag{3.2.6}$$

where $-\pi/2 < t < \pi/2$. The parameter t has a physical interpretation. The (circular) cross-section of the cone can be represented, in cylindrical

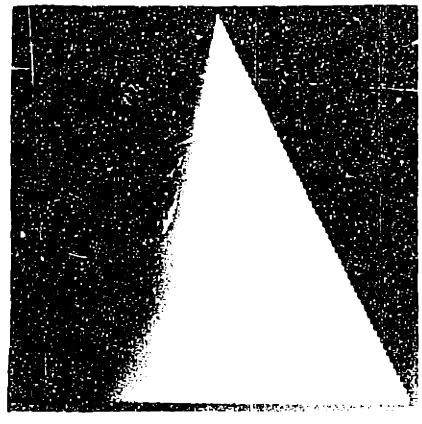

Figure 3-6 The synthesized image of a right circular cone (with height equal to twice the base radius and axis parallel to the image plane). The surface reflectance is assumed to be Lambertian with the light source placed at gradient point $p_s = 0.7$ and $q_s = 0.3$.

coordinates, by the function $\rho(\theta) = 1$ (where θ measures angular position about the y-axis). If θ is chosen so that $\theta = 0$ points in the direction of the viewer, then the parameter t in (3.2.5) and (3.2.6) is this angle θ.

Figure 3-7 shows the curve in gradient space determined by the parametric equations (3.2.5) and (3.2.6) superimposed on the reflectance map used to generate the image of figure 3-6. There exists a 1-1 continuous mapping between any horizontal image intensity profile from figure 3-6 and the curve in gradient space determined by (3.2.5) and (3.2.6). Thus, finding the point (p_0,q_0) in gradient space corresponding to any image intensity point $I(x_0,y_0) = \alpha$ from figure 3-6 simplifies to the problem of determining reflectance map values on the curve given by (3.2.5) and (3.2.6) for which $R(p,q) = \alpha$. If an intensity profile is scanned sequentially from left to right then possible multiple solutions can be resolved by chosing the solution which is "closest" to the previous solution in the direction of increasing t. This follows as a consequence of the general fact that all 1-1 continuous mappings are monotonic and the particular observation, for this case, that the mapping is monotonically non-decreasing.

3.3 (RIGHT) GENERALIZED CONES (WITH CIRCULAR CROSS-SECTION)

The previous section considered the imaging of singly curved surfaces. This section extends that work to consider a more general class of surfaces called generalized cones. Generalized cones are doubly curved. The curvature of a generalized cone, however, conveniently decouples (in its object-centered representation). For appropriate viewing conditions, this decoupling carries over to images of generalized cones. These images can be analyzed "almost" as if the surface were singly curved. The first

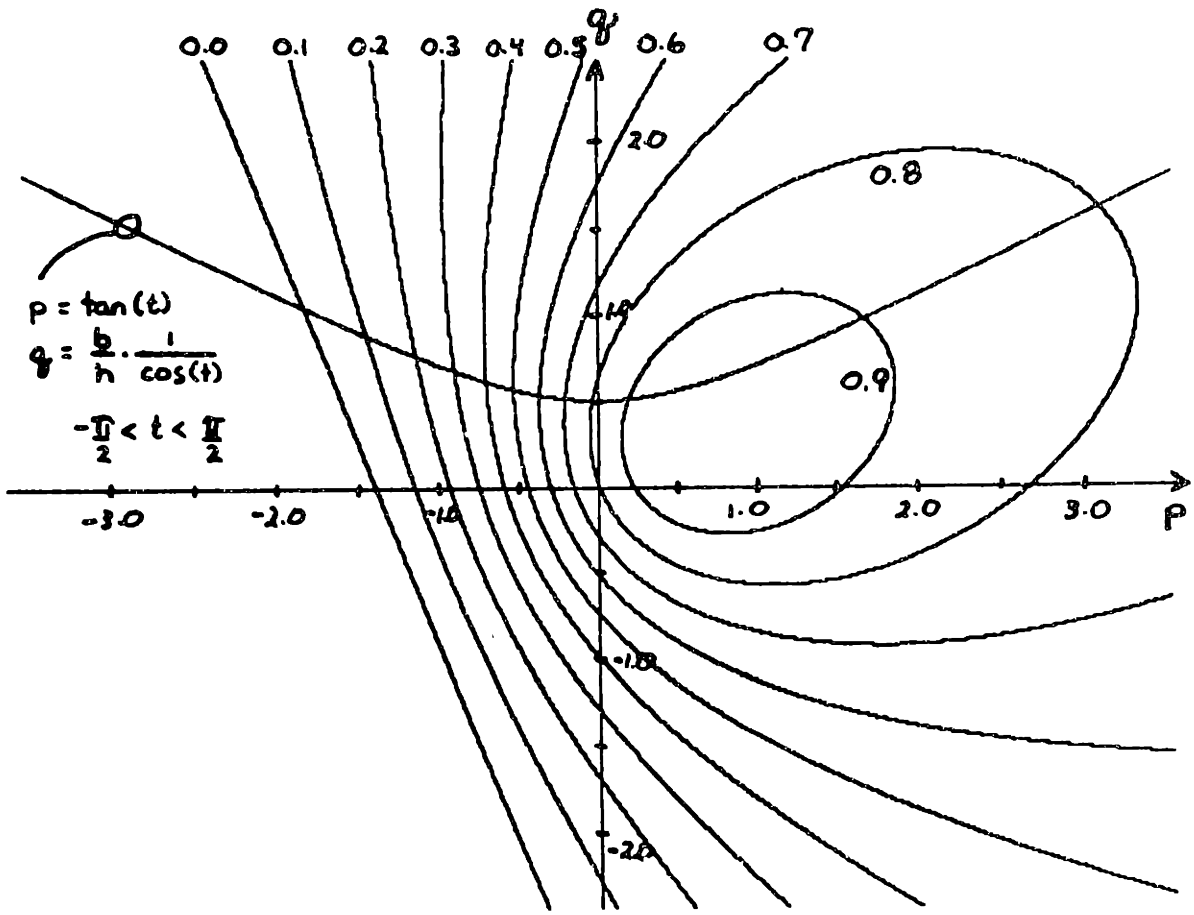

Figure 3-7 The one parameter curve in gradient space corresponding to points on the cone of figure 3-6.

result of this section is to demonstrate that, if the cone axis is parallel to the viewing plane, then images of right generalized cones with circular cross-section can be analyzed exactly as if the surface were singly curved. In this case, the additional information required to account for the second degree of freedom in curvature is not embedded in the intensity values present in the image but rather in the object silhouette. The more general case in which the cone axis makes a non-zero angle with the viewing plane is more difficult to analyze. The same decoupling of curvature holds but this decoupling is more difficult to recover. Finally, a few results are given for the case in which the cross-section is allowed to be an arbitrary convex function.

This section is important for two reasons. First, it extends the approach taken in the previous section to a broader class of surfaces. Second, it is an initial attempt to construct a bridge between methods of determining surface topography by analyzing the intensity variation across smooth sections of object surface and methods for determining object shape by analyzing the occluding contours present in an image.

This section is preliminary. Here, the question asked is, if the object is a generalized cone then how does this constrain the intensity values recorded in an image of the object. The question one really wants to ask is, how can the intensity values recorded in an image be used to determine whether the object is a generalized cone and, if so, determine its axis and cross-section function (in object space). At best, the results here correspond to a method for checking the consistency of hypotheses about surface shape determined from an analysis of the object silhouette against the actual intensity values recorded over smooth sections of the object surface.

The concept of a generalized cone has its genesis in the generalized cylinder representation of <Agin & Binford 73>. There, generalized cylinders were used as convenient representation scheme for describing complex shapes. Generalized cones, on the other hand, appear in the work of <Marr 76a>, <Marr 77>. Here, a generalized cone emerges not so much as a convenient representation scheme but rather as an interpretation that is forced if one tries to develop a theory of people's ability to infer the shape of objects from their silhouettes.

A *generalized cone* is defined to be the surface swept out by moving a simple smooth cross-section $\rho(\theta)$ along a straight axis Λ, at the same time magnifying or contracting it in a smoothly varying way. Let $h(\lambda)$ be the axial scaling function where λ denotes distance along the Λ axis. The angle ψ between the axis Λ and a plane containing a cross-section is called the eccentricity of the cone. For this section, it will be convenient to add two additional simplifying assumptions. First, assume that the eccentricity $\psi = \pi/2$. With this first assumption, the cone is called a *right generalized cone*. Second, assume that the cross-section is circular (with the axis Λ passing through the center of the circle). With this second assumption, the cone is called a *right generalized cone with circular cross-section*.

<Marr 76a> has defined methods for finding the projection of the axis Λ on the image plane of a generalized cone from an analysis of its occluding contour. The goal here is to provide a complementary study to interpret the intensity values recorded from the interior smooth sections of a generalized cone.

Let us begin with one further simplification. Assume that the axis Λ is parallel to the image plane. Since a rotation of object space induces and equal rotation in gradient space, one can, without loss of generality, assume that the axis Λ coincides with the image y-axis. This last assumption about the viewing direction will allow for the convenient decoupling of the generalized cone's curvature so that the image analysis problem becomes equivalent to that of analyzing a singly curved object. Distance along the axis Λ is equal to distance along the image y-axis so that the axial scaling function can be denoted as h(y). Let the circular cross-section function be denoted by $\rho(\theta) = 1$ (where $\theta = 0$ points in the direction of the viewer). It can be shown that the points in gradient space corresponding to points on such a right generalized cone with circular cross-section lie in the (two-dimensional) region in gradient space given parametrically by:

$$p = \tan(\theta) \tag{3.3.1}$$

$$q = \frac{-h'(y)}{\cos(\theta)} \tag{3.3.2}$$

where h'(y) denotes the derivative of h(y) with respect to y and $-\pi/2 < \theta < \pi/2$.

Figure 3-6 was an example of a (right) generalized cone (with circular cross-section). A right circular cone of base radius b and height h has axial scaling function h(y) where

$$h'(y) = \frac{-b}{h}$$

In general, (3.3.1) and (3.3.2) define a two parameter region in gradient space. One of the parameters is θ and the other is h'(y). (Of course, if

h'(y) is constant, as in figure 3-6, then the surface is singly curved.) The interesting observation, however, is that when the axis Λ is parallel to the viewing plane, the value of $h'(\lambda)$ can always be determined directly from the boundary contour. For a particular value of y, the curve in gradient space generated by (3.3.1) and (3.3.2) is a scaled version of the curve illustrated in figure 3-7. Differing values of -h'(y) introduce a different scale factor in q. Thus, finding the point (p_0,q_0) in gradient space corresponding to an image intensity point $I(x_0,y_0) = \alpha$ simplifies to a two step process. First, for the particular value of y_0, determine $h'(y_0)$ as the rate of change of object radius with respect to y (or equivalently as one half the rate of change of object diameter with respect to y) at the object boundary points along the image profile $y = y_0$. Second, as in the case of a singly curved object, scan a horizontal intensity profile to determine the correct reflectance map value on the curve given by (3.3.1) and (3.3.2).

Figure 3-8(a) is a more general example. Here, the axial scaling function is a sinusoid while the cross-section function remains circular. The surface depicted in figure 3-8(a) is doubly curved. Yet, the curvature decouples so that, from a image processing point of view, the surface behaves as if it were singly curved. Figure 3-8(b) superimposes a collection of these curves on the reflectance map used to generate figure 3-8(a). (Note: The sphere example of Chapter: 2.8 is also a right generalized cone with circular cross-section with an axis Λ that can always be chosen parallel to the viewing plane !)

Now consider the case in which the axis Λ of a right generalized cone with circular cross-section is not parallel to the viewing plane. Once again, a rotation of object space induces and equal rotation in gradient

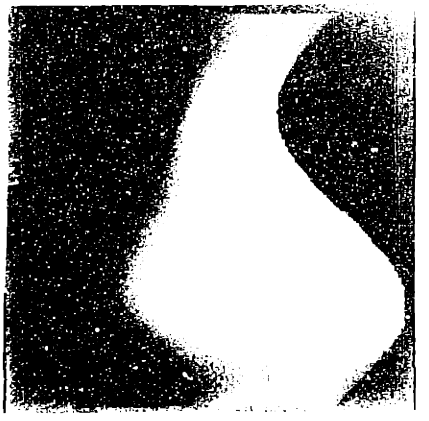

Figure 3-8(a) The synthesized image of a right generalized cone with circular cross-section (and axis Λ parallel to the image plane). The axial scaling function h(y) is a sinusoid. The surface reflectance is assumed to be Lambertian with the light source placed at gradient point $p_s = 0.7$ and $q_s = 0.3$.

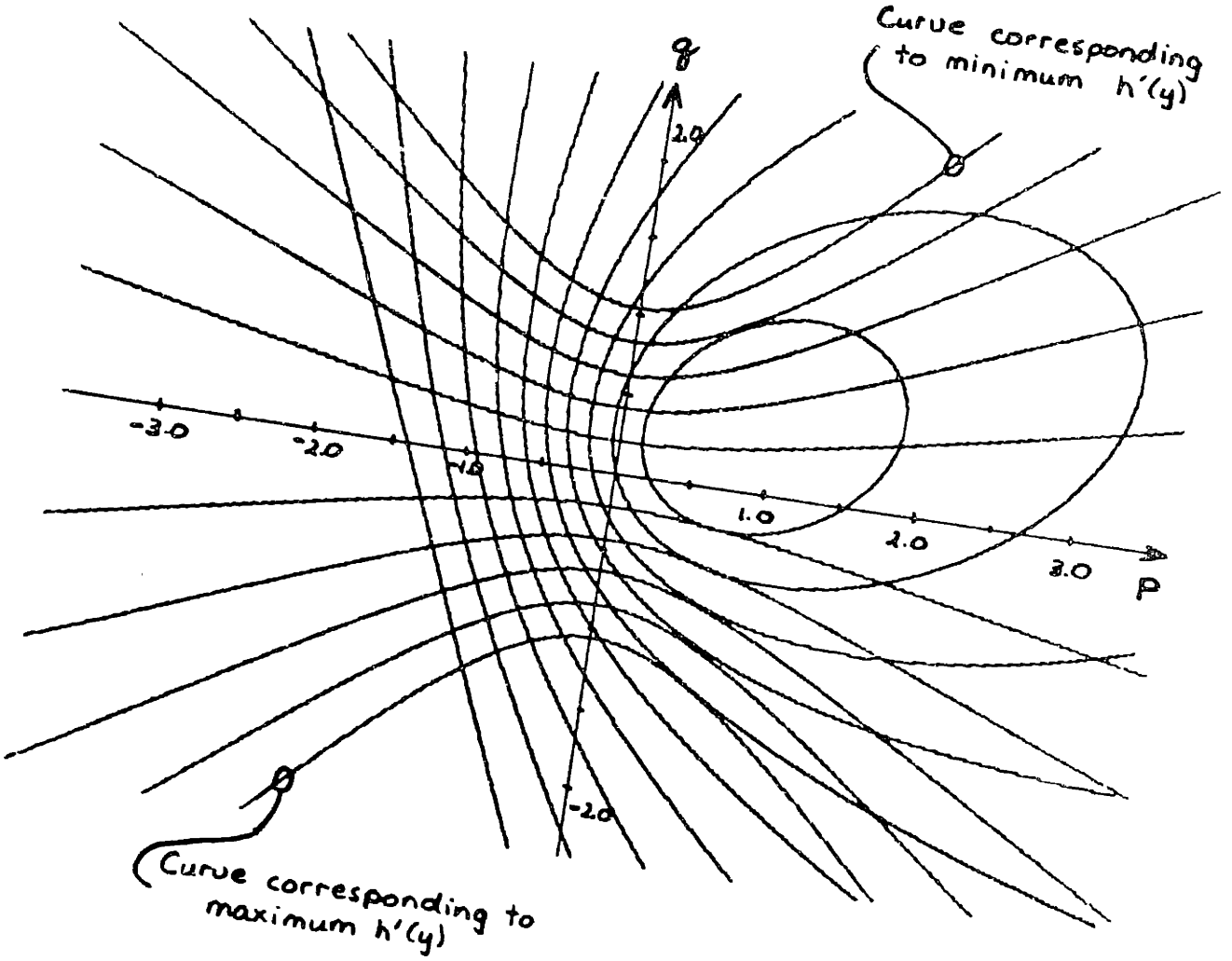

Figure 3-8(b) The region in gradient space corresponding to points on the right generalized cone of figure 3-8(a) (plotted as a family of curves). Note that the region in gradient space lies below the curve determined by the minimum value of h'(y) and above the curve determined by the maximum value of h'(y).

space so that, without loss of generality, assume that the projection of the cone's axis Λ on the image plane coincides with the image y-axis. Let the angle between the Λ axis and the viewing plane be ϕ (measured so that positive ϕ implies that the Λ axis is tilted towards the viewer). In this situation, distance along the image y-axis is simply a foreshortened version of distance along Λ. In particular,

$$y = \lambda \cos(\phi)$$

so that the derivative of the axial scaling function $h(\lambda)$ is given by:

$$h'(\lambda) = \cos(\phi)\, h'(y) = \cos(\phi)\, \frac{\text{rate of change of image diameter}}{2}$$

Now, tilting object space an angle ϕ about the x-axis takes gradient point (p,q) onto gradient point (p',q') where

$$p' = \frac{p}{\cos(\phi) + q \sin(\phi)}$$

$$q' = -\frac{\sin(\phi) - q \cos(\phi)}{\cos(\phi) + q \sin(\phi)}$$

Thus, the points in gradient space corresponding to points on a (right) generalized cone (with circular cross-section) lie in the (two-dimensional) region in gradient space given parametrically by:

$$p = \frac{\sin(\theta)}{\cos(\phi)[\cos(\theta) - \sin(\phi)h'(y)]} \qquad (3.3.3)$$

$$q = -\tan(\phi) + \frac{-h'(y)}{\cos(\phi)[\cos(\theta) - \sin(\phi)h'(y)]} \qquad (3.3.4)$$

where $h'(y)$ denotes the derivative of $h(y)$ with respect to y and $-\pi/2 < \theta < \pi/2$. For a particular value of y, the points corresponding to a cross-section on a (right) generalized cone (with circular cross-section) again lie on a one-parameter curve in gradient space. If ϕ is known, then

one can proceed as before, with only a slight complication in the mathematical expressions required. In general, however, the value of ϕ is unknown. This leads to two difficulties. First, without knowing ϕ, the curve in gradient space generated by (3.3.3) and (3.3.4) can not be determined. Second, without knowing ϕ, the intensity profile in the image corresponding to this curve can not be determined.

Consider a fixed value of $y = y_0$. Let (x_L, y_0) denote the "left" boundary point and (x_R, y_0) denote the "right" boundary point determined by the intersection of the line $y = y_0$ with the image silhouette. By the way the image axes have been aligned with respect to the cone, it must be the case that $x_L = -x_R$. Now, the image intensity profile corresponding to the curve generated by (3.3.3) and (3.3.4) lies on the ellipse centered at $(0, y_0)$ with major axis x_R, parallel to the image x-axis, and minor axis $|x_R \sin(\phi)|$, parallel to the image y-axis. If $\phi > 0$ (i.e., the cone is tilted toward the viewer), then the correct profile corresponds to the lower half of the ellipse. If $\phi < 0$ (i.e., the cone is tilted away from the viewer), then the correct profile corresponds to the upper half of the ellipse.

Thus, for any hypothesized value of ϕ, it is possible to determine a family of profiles in image space and the corresponding family of curves in gradient space. The gradient corresponding to each image point can then be determined once again as if the surface were singly curved. The gradients so determined can be integrated to determine a range profile across each image profile. These range profiles can be analyzed to see how well they correspond to a circular cross-section (tilted by an angle ϕ). In this way, an analysis of image intensity can be used to verify the choice of ϕ. A "best fit" ϕ can be determined in much the same fashion as the best-fit

image Hessian was found in Chapter: 3.1 above. That is, one can find that value of ϕ which is most consistent with the hypothesis that the image corresponds to a (right) generalized cone (with circular cross-section).

Finally, consider the case for which the cross-section is allowed to be an arbitrary smooth convex function. This result to be established here is essentially a negative one. Although the curvature of a (right) generalized cone decouples in its object-centered representation, the assumption of an arbitrary convex cross-section function no longer permits that decoupling to be achieved by an analysis of the object silhouette. This, in turn, does not allow for the simplification in image analysis that is achieved when the cross-section function is known *a priori*.

Let the cross-section function be given, in cylindrical coordinates, by $r = \rho(\theta)$. To avoid unecessary complication, this discussion will be restricted to the case in which the cone's axis Λ is parallel to the viewing plane. Once again, let the smoothly varying axial scaling function be $h(\lambda)$. It can be shown that the points in gradient space corresponding to points on such a (right) generalized cone lie in the (two-dimensional) region in gradient space given parametrically by:

$$p = \frac{\rho(\theta)\sin(\theta) - \rho'(\theta)\cos(\theta)}{\rho(\theta)\cos(\theta) + \rho'(\theta)\sin(\theta)} \qquad (3.3.5)$$

$$q = -h'(\lambda)\frac{\rho(\theta)}{\rho(\theta)\cos(\theta) + \rho'(\theta)\sin(\theta)} \qquad (3.3.6)$$

where $h'(\lambda)$ denotes the derivative of $h(\lambda)$ with respect to λ and $\rho'(\theta)$ denotes the derivative of $\rho(\theta)$ with respect to θ.

Again, (3.3.5) and (3.3.6) define a two parameter region in gradient space in the parameters θ and $h'(\lambda)$. The decoupling between these two (object-centered) parameters remains. For a fixed value of $h'(\lambda)$, (3.3.5)

and (3.3.6) determine a one-dimensional curve in gradient space. Differing values of $h'(\lambda)$ again simply scale this curve in q. Unfortunately, for an arbitrary convex cross-section function $\rho(\theta)$, it is not possible to conveniently discover this decoupling from the image silhouette. It is no longer necessarily true that the "left" occluding contour corresponds to $\theta = -\pi/2$ and the "right" occluding contour corresponds to $\theta = \pi/2$. Thus, even for the case in which Λ lies parallel to the viewing plane, $h'(\lambda)$ can no longer be determined directly from the silhouette.

If the left occluding contour corresponds to the value θ_L (where $-\pi < \theta_L < 0$) and the right occluding contour corresponds to the value θ_R (where $0 < \theta_R < \pi$). Then, $h'(\lambda)$ is given by:

$$h'(\lambda) = \frac{\text{rate of change of object diameter}}{[\sin(-\theta_L) + \sin(\theta_R)]}$$

The information required to determine $h'(\lambda)$ is still contained in the silhouette but it can be used only if the values θ_L and θ_R are known. The values of θ_L and θ_R, in turn, depend on $\rho(\theta)$.

3.4 PHOTOMETRIC STEREO: ANALYZING MULTIPLE IMAGES USING MULTIPLE LIGHT SOURCES

This section develops a rather obvious extension to the methods for determining the surface orientation corresponding to a given image point. The equation $I(x,y) = R(p,q)$ is one equation in the two unknowns p and q. The theoretical machinery developed in this thesis has been oriented towards seeking ways to exploit additional constraint in order to solve this underdetermined equation. Another approach is to somehow get more equations.

What can be varied? If either the object or viewer is moved then one has stereo. This no longer is a photometric method but a triangulation technique. The difficult problem then is the determination of the correspondence between points in one image and points in the other. Stereo techniques are not suited for sections of smoothly varying object surface. Fortunately, there is a third component in the image forming process, the position of the light source(s).

Suppose that the object is first viewed with the light source placed at gradient point (p_{s1},q_{s1}). Call the corresponding reflectance map $R_1(p,q)$. This generates a first image $I_1(x,y)$ which satisfies the equation:

$$I_1(x,y) = R_1(p,q)$$

Now, suppose the object is viewed a second time with the light source placed at gradient point (p_{s2},q_{s2}). Call the corresponding reflectance map $R_2(p,q)$. This generates a second image $I_2(x,y)$ which satisfies the equation:

$$I_2(x,y) = R_2(p,q)$$

The important observation is that there has been no change in the imaging geometry. Thus, there is no problem in determining which points in the first image match those in the second. Each (x,y) corresponds to the same object point and thus to the same gradient (p,q) in both images. There are now two independent equations in the two unkowns p and q:

$$\begin{aligned} I_1(x,y) &= R_1(p,q) \\ I_2(x,y) &= R_2(p,q) \end{aligned} \qquad (3.4.1)$$

These two (non-linear) equations will have at most a finite number of solutions.

But, are two reflectance maps really required? Suppose that the phase angle g is held constant in both views. That is, suppose (p_{s1},q_{s1}) and (p_{s2},q_{s2}) are chosen so that

$$\sqrt{p_{s1}^2 + q_{s1}^2} = \sqrt{p_{s2}^2 + q_{s2}^2}$$

Then, the corresponding two reflectance maps $R_1(p,q)$ and $R_2(p,q)$ are related by a simple rotation. Indeed, if θ is the angle of rotation that takes (p_{s1},q_{s1}) to (p_{s2},q_{s2}), then

$$R_2(p,q) = R_1(p',q') \qquad \text{where}$$

$$\begin{bmatrix} p' \\ q' \end{bmatrix} = \begin{bmatrix} \cos(\theta) & -\sin(\theta) \\ \sin(\theta) & \cos(\theta) \end{bmatrix} \begin{bmatrix} p \\ q \end{bmatrix}$$

For example, if $\theta = 90^\circ$, then the two equations become:

$$I_1(x,y) = R(p,q)$$

$$I_2(x,y) = R(-q,p)$$

There are three ways to proceeed. If image point (x,y) is known to correspond to the gradient point (p,q) and if $[R_{1p},R_{1q}]$ and $[R_{2p},R_{2q}]$ are linearly independent, then the image Hessian matrix H is uniquely determined as:

$$H = \begin{bmatrix} I_{1x} & I_{2x} \\ I_{1y} & I_{2y} \end{bmatrix} \begin{bmatrix} R_{1p} & R_{2p} \\ R_{1q} & R_{2q} \end{bmatrix}^{-1}$$

(Here, the first subscript identifies the image and the second subscript denotes partial differentiation.) Thus, one way to proceed is to start at an image point (x_0,y_0) known to correspond to gradient point (p_0,q_0) and expand a complete solution over a section of smooth surface using the equation

$$[dp,dq]^T = H\,[dx,dy]^T$$

(Since, at each step, H is completely determined, the direction chosen for

the movement [dx,dy] is arbitrary.)

A second way to proceed is to determine the (finite number of) solutions to (3.4.1). In general, the number of solutions will be greater than one. These solutions, however, can be used as the input to the relaxation algorithm discussed in Chapter: 2.7. Such *a priori* constraints as convexity and concavity can be used to quickly nail down a unique surface interpretation.

An even simpler way to proceed is to use additional light sources to overdetermine the solution. Suppose the object is viewed a third time with the light source placed at gradient point (p_{s3},q_{s3}). Call the corresponding reflectance map $R_3(p,q)$. This generates a third image $I_3(x,y)$ which satisfies the equation:

$$I_3(x,y) = R_3(p,q)$$

Again, if the phase angle g is held constant, then the three reflectance maps $R_1(p,q)$, $R_2(p,q)$ and $R_3(p,q)$ are simply rotations of each other. The set of equations:

$$I_1(x,y) = R_1(p,q)$$

$$I_2(x,y) = R_2(p,q)$$

$$I_3(x,y) = R_3(p,q)$$

is now overdetermined, and, barring degeneracy, will have at most one solution.

Now, there are actually two distinct ways to exploit the additional information in multiple images from multiple light source positions. First, as has been the primary goal, this technique can be used to determine the local surface orientation of the object point corresponding to a given image point. Interestingly enough, this technique can also be used to determine points in an image whose corresponding object points have

a given local surface orientation (This corresponds to picking an orientation (p,q) and then finding image points (x,y) corresponding to object points having this orientation.)

3.4.1 DETERMINING THE SURFACE ORIENTATION AT AN OBJECT POINT

Suppose three images $I_1(x,y)$, $I_2(x,y)$ and $I_3(x,y)$ are taken under a fixed object surface viewer geometry but with a varying light source position. Suppose the corresponding reflectance maps are $R_1(p,q)$, $R_2(p,q)$ and $R_3(p,q)$. Choose a particular image point (x_0,y_0) and suppose that the intensities at (x_0,y_0) in the three images are given by $I_1(x_0,y_0) = \alpha_1$, $I_2(x_0,y_0) = \alpha_2$ and $I_3(x_0,y_0) = \alpha_3$. Assume that image intensity has been normalized with respect to the reflectance map so that

$$I_i(x,y) = R_i(p,q)$$

in each of the three images. Now, plot, in gradient space, the three contours $R_1(p,q) = \alpha_1$, $R_2(p,q) = \alpha_2$ and $R_3(p,q) = \alpha_3$. Any gradient point (p,q) lying on all three contours is a possible gradient corresponding to the image point (x_0,y_0). If there is only one such (p,q), then this (p,q) uniquely determines the local surface orientation at the object points corresponding to the given image point (x_0,y_0).

Figure 3-9 illustrates this technique. The example once again uses the Lambertian sphere of Chapter: 2.8. The first light source was placed at $p_s = 0.7$, $q_s = 0.3$ as before. The second and third sources were positioned each a 120° (anti-clockwise) rotation from the previous source. The image point x = 15, y = 20 was sampled in each of the three images so generated. The three (normalized) intensity values determined were: $I_1(x,y) = 0.942$, $I_2(x,y) = 0.723$ and $I_3(x,y) = 0.505$. Figure 3-9 plots the three corresponding contours from the corresponding reflectance maps. They

intersect at $p = 0.275$, $q = 0.367$ which is the gradient corresponding to the image point $x = 15$, $y = 20$.

3.4.2 DETERMINING OBJECT POINTS WITH A GIVEN SURFACE ORIENTATION

Again, suppose three images $I_1(x,y)$, $I_2(x,y)$ and $I_3(x,y)$ are taken under a fixed object surface viewer geometry but with a varying light source position. Suppose the corresponding reflectance maps are $R_1(p,q)$, $R_2(p,q)$ and $R_3(p,q)$. Choose a particular gradient point (p_0,q_0) and suppose that the reflectance values at (p_0,q_0) in the three reflectance maps are given by $R_1(p_0,q_0) = \alpha_1$, $R_2(p_0,q_0) = \alpha_2$ and $R_3(p_0,q_0) = \alpha_3$. Again, assume that image intensity has been normalized with respect to the reflectance map so that

$$I_i(x,y) = R_i(p,q)$$

in each of the three images. Now, plot, in image space, the three (normalized) contours $I_1(x,y) = \alpha_1$, $I_2(x,y) = \alpha_2$ and $I_3(x,y) = \alpha_3$. These three contours may intersect in zero, a finite number or an infinite number of points. If they do not intersect in at least one point, then there is no object point in view with surface orientation given by the gradient (p_0,q_0). If they intersect in a finite number of points, then, barring degeneracy, each image point (x,y) in the intersection corresponds to an object point with local surface orientation given by the gradient (p_0,q_0). If the surface is not doubly curved, then the intersection will either be empty or will include an infinite number of points.

Figure 3-10 shows how to use this technique to determine a pseudo-origin (i.e., an image point corresponding to an object point whose surface normal points directly at the viewer). The three images of the previous example were used. This time, the goal is to find object points

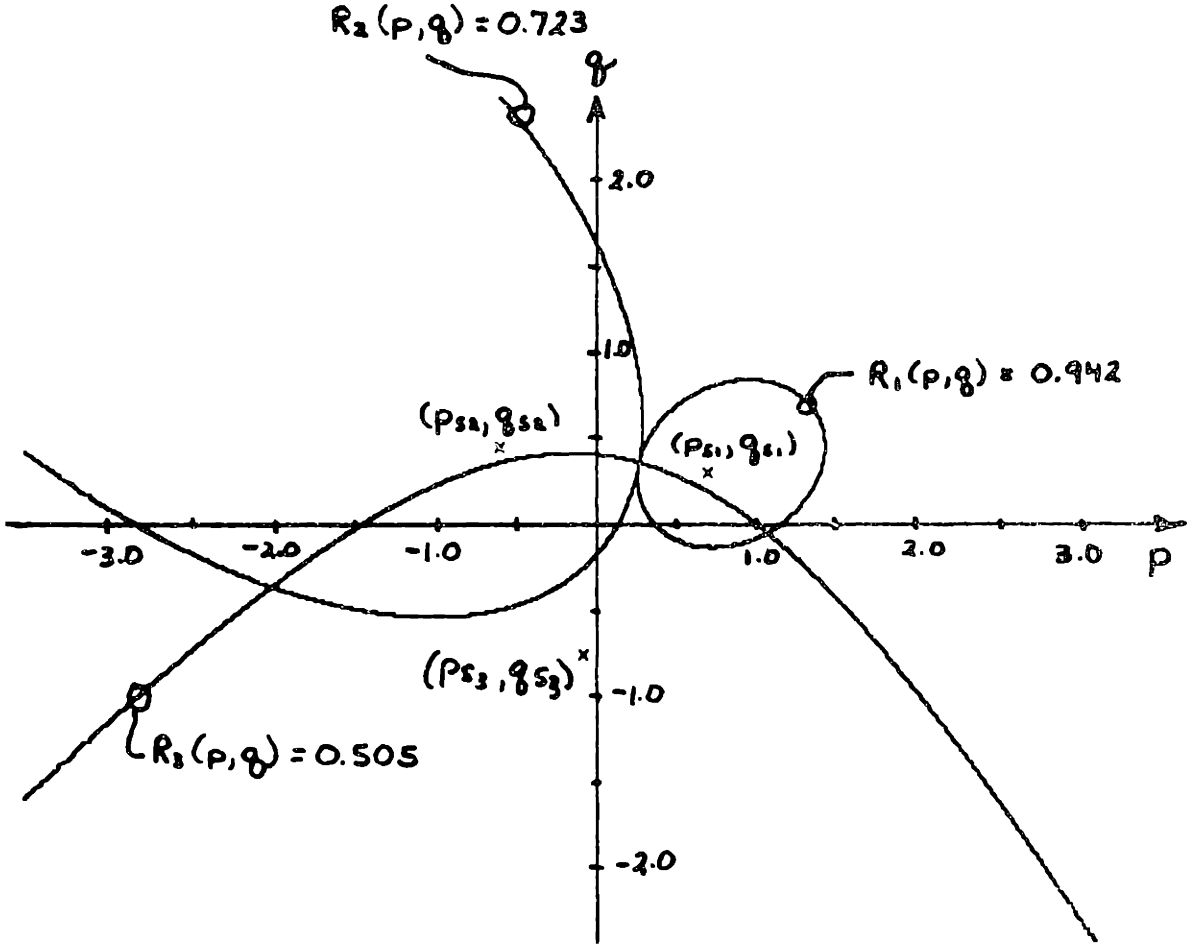

Figure 3-9 Determining the surface orientation at a given image point (x,y). Three (superimposed) reflectance map contours are intersected where each contour corresponds to an intensity value at (x,y) obtained from three separate images (taken under the same imaging geometry but with different light source position).

with gradient p = 0, q = 0. The three reflectance map values determined were:

$$R_1(x,y) = R_2(x,y) = R_3(x,y) = 0.796$$

Note: p = 0, q = 0 is the (unique) gradient whose reflectance map value is preserved by a rotation about the view vector (of either the light source or the object itself). Figure 3-10 plots the three corresponding intensity contours from the three images. They intersect at x = 0, y = 0 which is the correct pseudo-origin used in the example of Chapter: 2.8.

Figure 3-11 is a slightly more general example. The desired gradient was p = 0.5, q = 0.5. The three reflectance map values determined were: $R_1(x,y) = 0.974$, $R_2(x,y) = 0.600$ and $R_3(x,y) = 0.375$. Figure 3-11 plots the three corresponding intensity contours from the three images. They intersect at x = 24.5, y = 24.5 which is the image point with corresponding gradient is p = 0.5, q = 0.5.

3.4.3 USING PHOTOMETRIC STEREO

In practice, one has to be careful. As in any "stereo" technique, there is an inherent trade-off to acknowledge. Choosing a large phase angle g allows one to achieve a better "conditioning" of the gradient contours that must be intersected from each image. At the same time, a large phase angle g puts more of gradient space into the shadow region of one or more of the sources. In practice, it is convenient to use four point sources (each a 90° rotation from its two neighbors). In the example below, the first source was again positioned at $p_s = 0.7$, $q_s = 0$ 0.3 (this corresponds to a phase angle of 37.3°). This allows one to guarantee that all object points within 61.7° view angle are illuminated by at least three of the sources. (Further, in the case of Lambertian reflectance, in

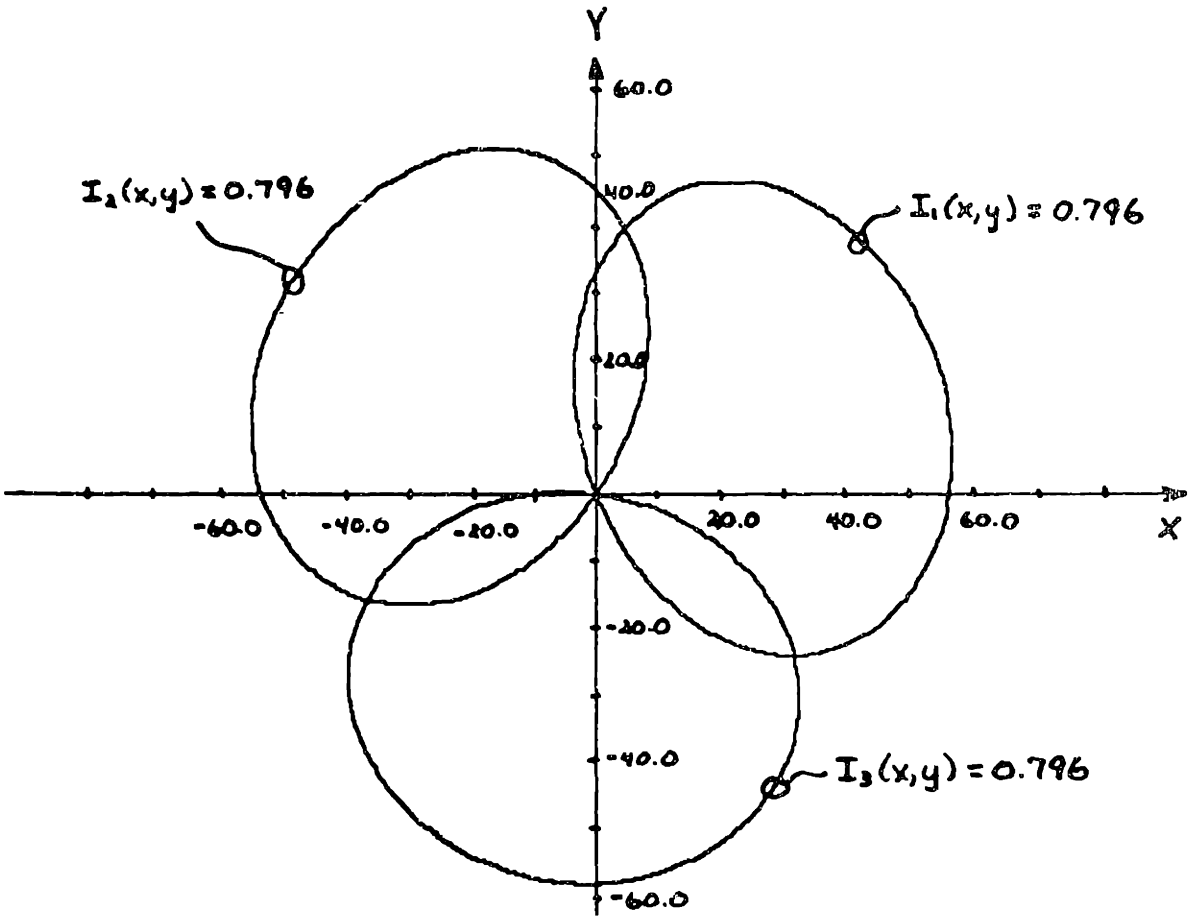

Figure 3-10 Determining image points whose surface normal directly faces the viewer. Three (superimposed) image intensity contours are intersected where each contour corresponds to the value at (0,0) obtained from three separate reflectance maps. (Each reflectance map characterizes the same imaging geometry but corresponds to a different light source position.)

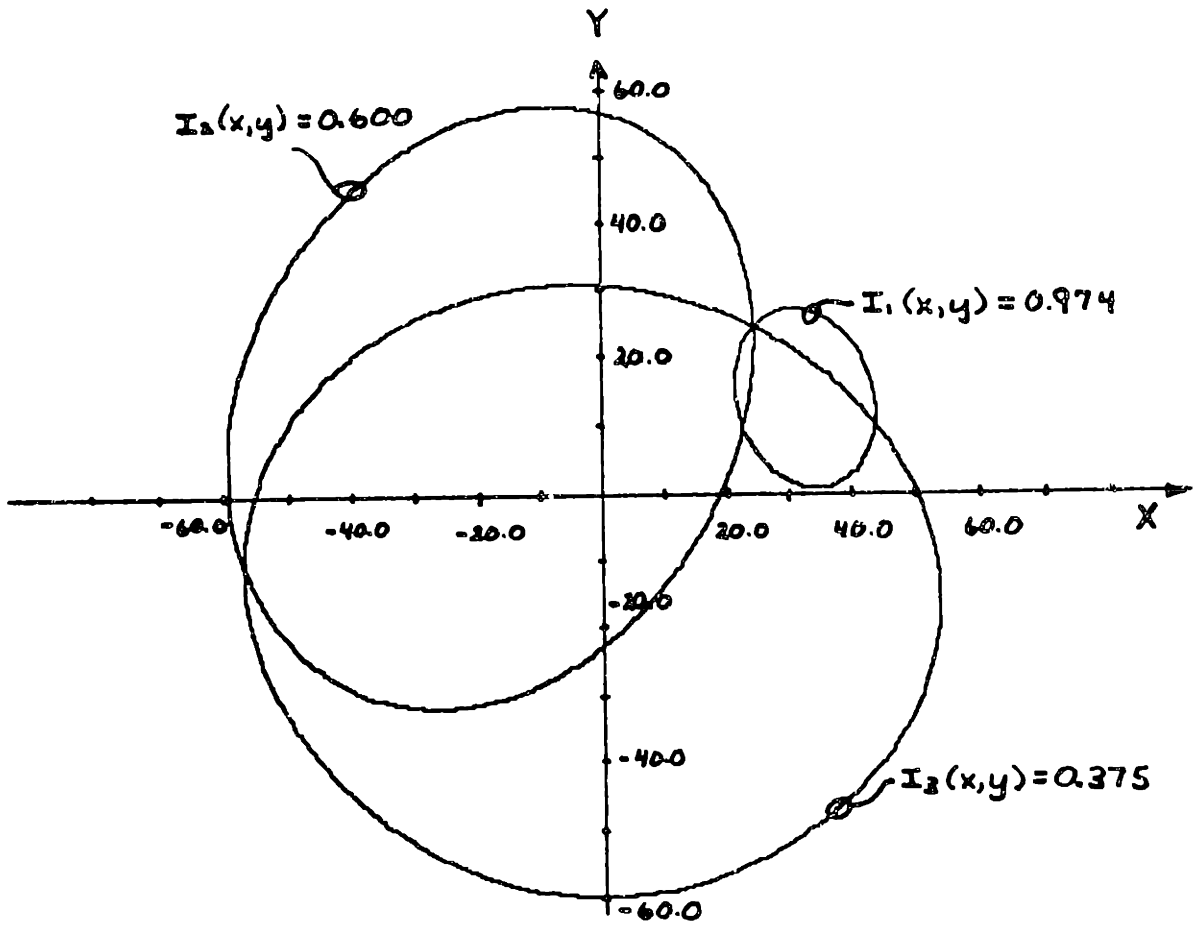

Figure 3-11 Determining image points whose surface normal is given by the gradient (p,q). Three (superimposed) image intensity contours are intersected where each contour corresponds to the value at (p,q) obtained from three separate reflectance maps. (Each reflectance map characterizes the same imaging geometry but corresponds to a different light source position.)

sections of gradient space illuminated by only two sources, contours intersect uniquely.) Thus, with this four source scheme, one can always determine the gradient corresponding to a selected image point.

Figure 3-12 illustrates this four source scheme applied to the sample sphere of Chapter: 2.8. Here, all gradient points corresponding to sampled image points have been pinned down exactly. Figure 3-13 superimposes on figure 3-12 the light source positions and corresponding shadow-lines. These shadow-lines divide gradient space into nine regions, each illuminated by a different combination of the four sources.

Photometric stereo is interesting in that it is fast and dumb. In inspection situations in which one has control over the nature and position of the incident illumination and in which one is dealing with objects of uniform photometric properties, it has the potential to be a practical scheme for determining surface topography. This, in turn, solves the major problems associated with the early processing of image intensities, namely, factoring out the effects of image illumination and surface photometry.

Engineering implementation of photometric stereo can be achieved by explicitly moving a single light source, by using multiple light sources calibrated with respect to each other or by rotating the object surface and imaging hardware together (thus simulating the effect of a moving light source).

Of course, photometric stereo works well using synthesized images. What difficulties might one expect in practice? First of all, the method is subject to the same restrictions that apply to the analysis of a single image using an equation of the form

$$I(x,y) = R(p,q)$$

(see Chapter: 2). Non-uniformities in imaging hardware, surface photometry

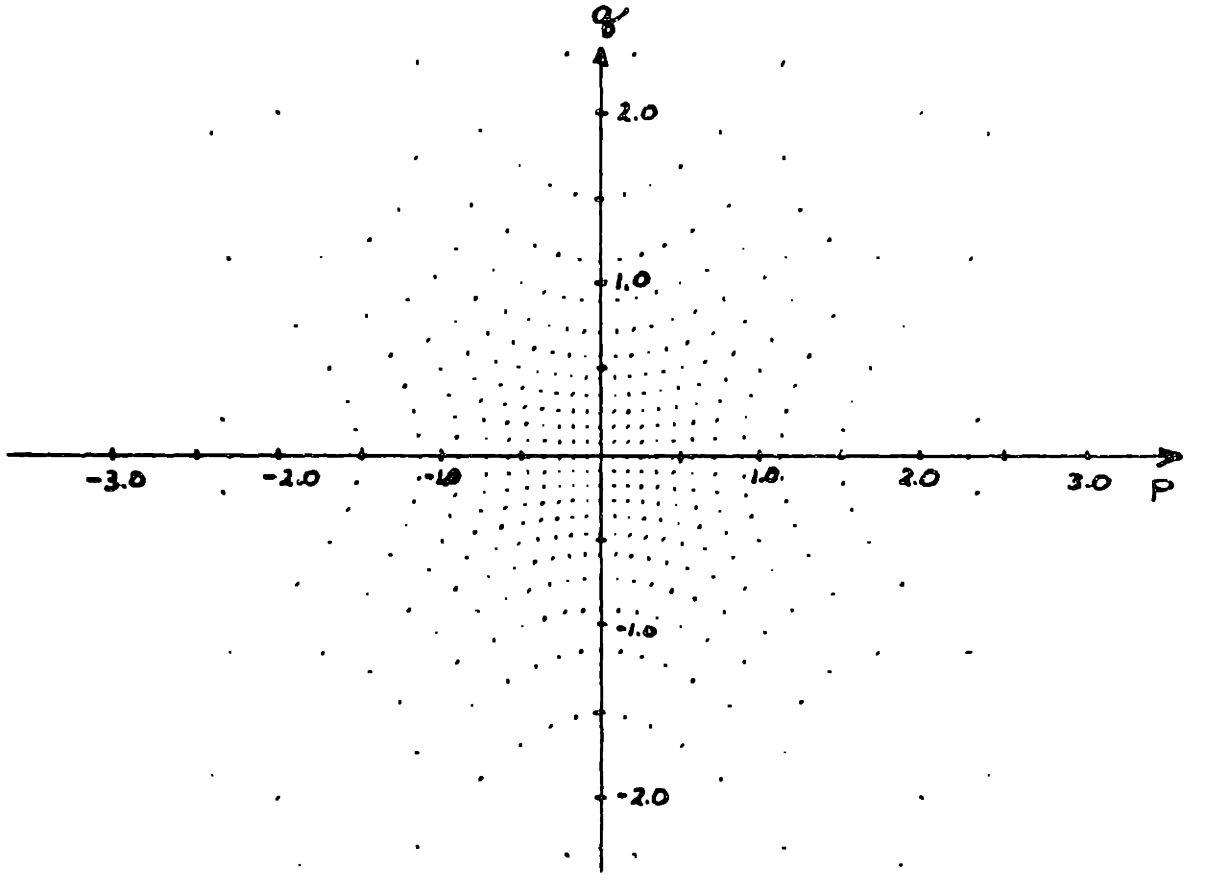

Figure 3-12 Applying photometric stereo to four synthesized images of a sphere. The surface reflectance is assumed to be Lambertian. The points mark the gradients determined at each sampled image point. [Compare this figure with the single image result of Figure 2-10.]

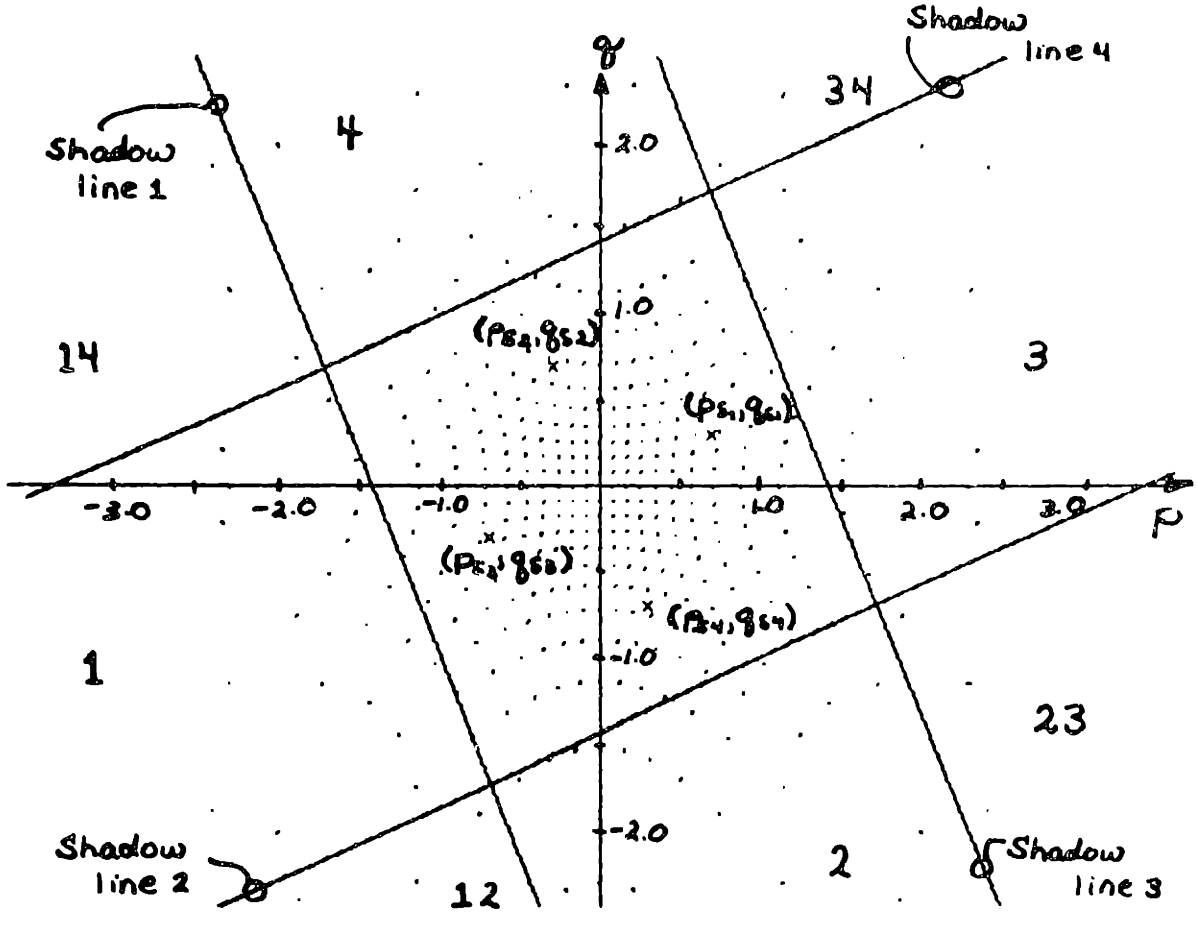

Figure 3-13 Superimposing the light source (and corresponding shadow-line) positions used to determine figure 3-12. This four source configuration divides gradient space into nine regions. The numbers in each region indicate which sources can not illuminate that region.

and incident illumination (due to mutual illumination) will all lead to inaccuracies. One can gain some further insight into how such inaccuracies will affect photometric stereo. Figure 3-14 plots the contours associated with a two source Lambertian configuration (spaced 0.1 units apart) when the light sources are separated by 90°. Each region of Figure 3-14 corresponds to a region of equal error. The configuration depicted in figure 3-14 is quite tolerant of errors for image points whose corresponding gradient lies in the third quadrant of gradient space. On the other hand, slight errors in the measurement of intensity for image points whose gradient lies in the first or second quadrant can lead to substantial errors in the solution determined for that gradient. Figure 3-15 repeats figure 3-14 but for the case when the light sources are separated by 180°. Here, reasonable accuracy is achieved in the second and fourth quadrants.

This analysis is purposely quite qualitative. In any numerical solution to an over determined problem (which is likely to be subject to errors in estimation) one can expect to achieve no exact solution. Figure 3-14 and figure 3-15 give some indication about about how one might select which light source combinations to "believe" with accuracy and which to hold suspect. In practice, the particular nature of the reflectance map must also be taken into account.

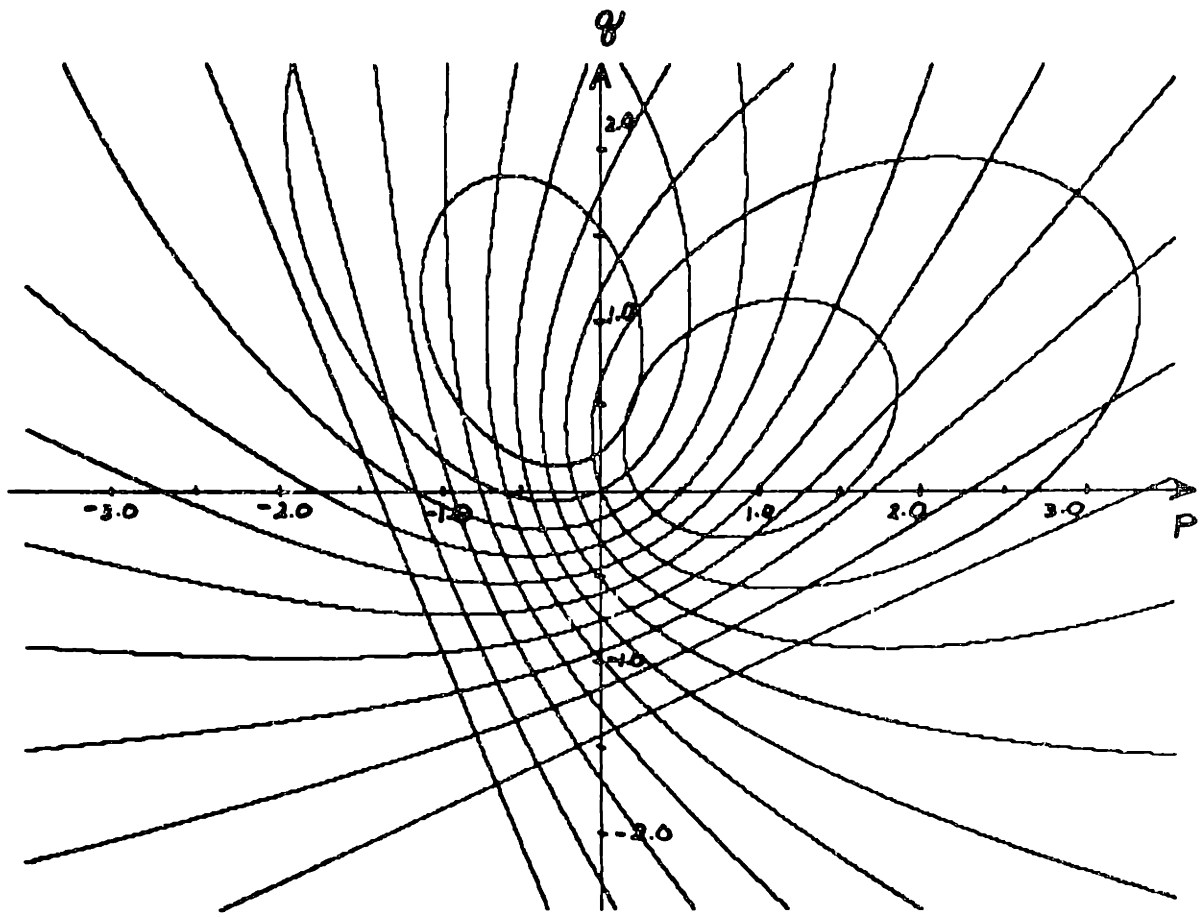

Figure 3-14 Error regions for two (superimposed) reflectance maps corresponding to Lambertian surfaces illuminated by separate sources rotated 90° with respect to the other ($g = 37.3°$). Each region indicates (qualitatively) how a fixed error in intensity maps into a corresponding error in the determination of surface orientation.

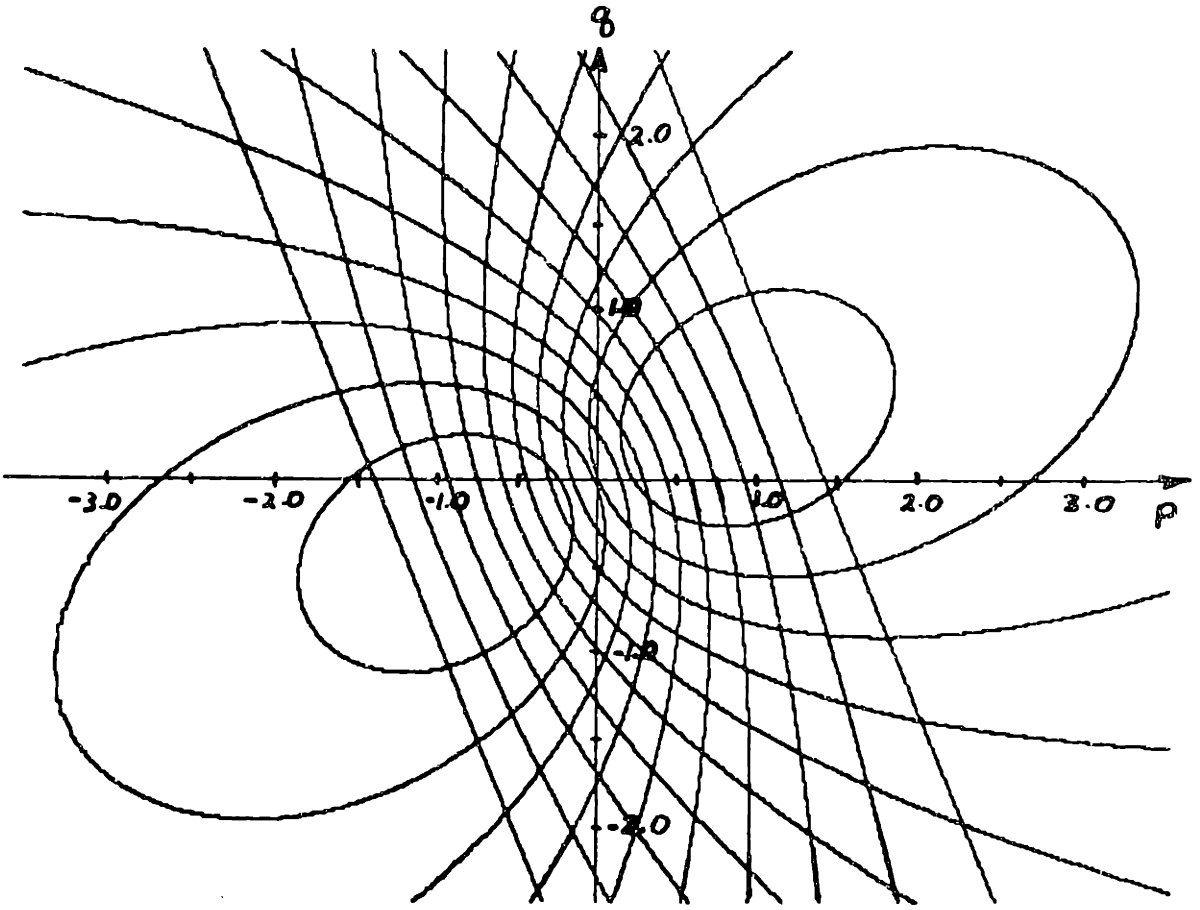

Figure 9-15 Error regions for two (superimposed) reflectance maps corresponding to Lambertian surfaces illuminated by separate sources rotated 180° with respect to the other ($g = 37.3°$). Each region indicates (qualitatively) how a fixed error in intensity maps into a corresponding error in the determination of surface orientation

4. TWO CASTING APPLICATIONS

In order to understand the inspection requirements of the casting industry, it is vital to obtain actual exposure to realistic foundry environments. In the course of this work, two foundries were visited. These two foundries represent two extremes of the metal castings industry. The first was an experimental foundry for the development of precision investment cast turbine blades and vanes for aircraft jet engines. The second was a large batch-oriented green sand mold production foundry.

In this chapter, an attempt is made to detail the inspection requirements representative of the metal casting industry. This serves both as a general introduction to casting inspection and as a motivation for the particular inspection tasks addressed in subsequent chapters.

4.1 PRECISION INVESTMENT CASTING

Investment casting is the most sophisticated casting process commercially available. It permits the reproduction of finer detail, greater dimensional accuracy, and smoother finished surfaces than can be obtained by any other casting process. It permits mass production of complex shapes that are difficult or impossible to produce by conventional casting processes or by machining. Castings can be produced that require little or no finishing for completion, thus minimizing the importance of selecting easy-to-machine metals.

Investment casting allows close control of grain size, grain orientation and other solidification conditions which results in close control of mechanical properties. The process is adaptable to almost any metal that can be melted and poured. It is also adaptable to the melting and casting of alloys that must be poured in a vacuum or under the

protection of an inert atmosphere.

4.1.1 ONE PART IN THE MAKING

The first class of parts to be discussed is that of turbine blades and vanes for aircraft jet engines. Initially, turbine airfoils were made by forging. Now, however, forging has been replaced by investment casting. The reasons for this switch are twofold:

- A gas turbine becomes more efficient as its operating temperature is raised. Alloy development for superior high-temperature performance made forging impractical.
- Sophisticated air cooling schemes have been developed to permit operation at even higher temperatures. The internal passageways necessary for cooling can be produced only by casting.

The particular turbine blades and vanes studied here are made of a special high temperature nickel-base alloy using a precision shell investment casting process. The initial tooling cost for this type of casting is substantial. Consequently, in this environment, one typically deals with relatively few part types produced at a relatively high volume (or, as is the case here, a part type for which there is no alternative manufacturing process available).

Casting is basically the process of pouring molten metal into a mold, letting the metal solidify and then separating the part from the mold. In certain casting processes, such as die casting, the mold is not destroyed each time a part is produced. In other casting processes, such as green sand mold casting discussed below, the mold is destroyed when the part is removed. In such processes, part reproducibility is maintained in the

pattern used to produce the mold.

In investment casting, both the pattern and the mold are destroyed for each part made. In this case, part reproducibility is maintained in the accurately machined metal dies used to produce each pattern. Investment casting employs a cermaic mold. The mold is produced by surrounding an expendable pattern, made of wax or plastic, with a refractory slurry. After the mold has set, the pattern is melted or burned out, creating the mold cavity. Finally, the mold is kiln hardened.

In this particular application, the inside of each turbine airfoil is hollowed out in an elaborate pattern. (This pattern produces the internal passageways used for air cooling.) To cast these passageways, a core (i.e., a negative image of the volume to be hollowed out) is itself produced out of a silica material. This core is fixed in the wax pattern by inserting it between the pattern die halves prior to the injection of the wax. Thus, after the wax has been burned away from the ceramic mold, the core becomes part of the mold.

The ceramic shell mold is prepared by alternately dipping the pattern assembly (pattern and core) into slurries of ceramic powders suspended in a liquid, draining the excess, stuccoing the wetted surface with a dry refractory grain and drying the resultant coating. This process is repeated until the desired mold thickness is achieved (generally 1/4" to 1/2"). The initial coating employs a slurry that is made up of particles finely ground to provide the desired surface smoothness. Subsequent coatings contain increasingly coarser refractory grains.

The mold is dried after each dipping operation to allow bonding of its individual layers. Moisture removal is regulated by control of wet and dry bulb temperatures, air flow and time. The completed mold is allowed to dry

for a minimum of 24 hours. When the mold has dried out, the wax is burned off leaving the silica core suspended in the mold cavity. Final curing of the mold is achieved by kiln hardening.

Most high-temperature superalloys are melted using a vacuum-induction furnace. Vacuum melting reduces the amount of dissolved gases in the metal. It also prevents contamination of the metal by the gaseous elements present in normal air atmospheres and actually helps purify the metal through volatilization of existing impurities. Vacuum melting reduces the number of resulting inclusions in the casting and thus improves the mechanical properties of the metal.

The molds are readied in a preheat furnace and then moved to the mold locker chamber. After this chamber has been evacuated, the interlock between it and the main furnace chamber is opened and the mold is moved into pouring position. When the specified pouring temperature has been reached, the metal is poured into the mold at a controlled rate. The mold is then withdrawn back into the mold locker chamber and the interlock closed. The mold chamber is then opened to allow removal of the filled mold.

After solidification, the ceramic mold material is broken away and the casting is cleaned by simple sand blasting. A first visual inspection is performed to catch obvious defects (for example, the mold may have cracked). Passing this inspection, the casting is immersed in a strong caustic solution to eat away the silica core which, at this point, is still embedded in the casting.

Each casting then undergoes exhaustive inspection. In an application as critical as the production of components for aircraft jet engines, part integrity is of paramount importance. In the United States, castings for

aircraft engines are 100% inspected (i.e., each casting undergoes each inspection operation). The inspection operations performed are summarized below:

- A coordinate gauging machine is used to verify the outer dimensions of the casting.
- Ultrasonic transducers are applied to selected points on the casting to verify the inner dimensions of the casting. (In this case, it is to verify that the core was positioned correctly.)
- The casting is X-rayed from multiple views and the resulting images are checked for indications of inclusions and other internal defects.
- Flourescent penetrant inspection is performed on all visible surfaces of the casting to check for surface cracks, tears, porosity and inclusions.
- The casting is acid-etching to verify grain structure.
- Pressure/leak testing is performed on the internal passageways of the casting to verify that none are blocked due to residual core material or due to excess metal resulting from collapsed core material.

Detailed quality standards are used for each of the above inspection operations. The basic format of these quality standards is to divide the casting into areas, each of which is judged by a portion of the standard written specifically for it. Important considerations include the absolute size of each imperfection, the total number of imperfections and the relative spacing between imperfections. This division of the casting into areas is based upon the actual service requirements of the various

subsections of the casting. For example, critical areas, subject to high stresses, are inspected to tighter criteria than are areas subject to lesser degrees of stress.

It is important to realize that these quality standards can not be implemented by simple detection devices. Detection devices may be used to enhance the delineation of an imperfection, but, the mere presence of imperfections does not lead to an ACCEPT/REJECT decision. Rather, imperfections must be interpreted in the context of the part as a whole. The ability to automate existing industry standards ultimately requires the ability to relate the imperfections detected to a higher-level representation of the object shape.

4.2 GREEN SAND MOLD CASTING

Green sand molding is the most versatile and inexpensive casting process commercially available. Typical green sand mold foundries are batch-oriented, producing many different castings at low to medium production volumes. At the particular foundry visited, approximately 40% of the castings produced were to meet the internal manufacturing demands of the parent company. The remaining 60% were cast on a contract basis for outside customers. The foundry maintains a library in excess of 100,000 patterns, any one of which can be scheduled for production. Orders range from fewer than 10 parts to as many as 250,000.

In preparing a casting for production, extensive inspection and destructive test facilities are available to eliminate systematic design flaws. In each application, however, there is an inevitable trade-off reached between design cost and production cost. A decision must be made as to whether the production quantity involved warrants further effort to

modify the casting design. In a batch-oriented foundry, many of the process variables (such as alloy composition, pouring temperature and sand composition) must be considered fixed since they can not be modified from part to part. Thus, the most economical compromise often tolerates a high rejection rate during production. The rejection rates for castings produced at the foundry visited typically vary between 6% and 30%, depending principally on the size, shape and complexity of the part.

Green sand mold casting has the advantage that all the materials required can be recycled. The pattern is reusable. The sand used to make the mold is reusable. Should the casting be defective, the metal is also reusable. Thus, a high rate of rejection is not that expensive. The cost of manufacturing a defective part is the cost of the energy required to re-melt the metal and the cost in time and labor associated with the loss in production capacity.

The principal goal of inspection is to find defective castings before investing expensive machining operations on a bad part. Approximately 85% to 90% of the casting defects are sufficiently gross in nature that they are easily found by unskilled inspectors immediately following mold removal and cleaning. These human inspectors perform a cursory examination of each casting as it comes out of the sandblast machines. Ones that pass this first visual inspection are sorted into appropriate bins. The remaining ones are catalogued by an inspection foreman and then recycled to the melting furnace.

A second level of visual inspection is achieved by making it profitable for in-house machinists to find defective castings. Machinists are employed to smooth away residual traces of gating and other minor surface imperfections from the castings. These machinists are paid on a

piecework basis. They are paid for each piece they grind and for each piece they find to be defective. Thus, a few seconds of visual inspection can earn as much as several minutes of grinding. (One of the major problems the foundry foreman has is that a few unnoticed swings with a hammer can make a machinist as much money as a half an hour of "regular" work.)

Castings that leave the foundry have a reasonable chance of being free of defects on all visible surfaces. No inspection, however, is provided to verify the internal integrity of the part. Such castings are not produced on a "guaranteed" basis. Defects are often found during subsequent machining operations. A potential disagreement between a foundry and its customers centers around the cost of machining defective parts. The foundry does not pay for machining operations performed after a part has left the foundry. The customer, however, will often argue that the foundry should absorb these machining costs since, after all, the part was defective.

Green sand molding is chosen precisely because it is the cheapest and most flexible process available for the batch-oriented requirements of this foundry. With current technology, a more thorough inspection of each casting is cost prohibitive. Rejection rates of 6% to 30% must be tolerated in order to keep the cost per casting down to the desired level.

Before presenting the second class of parts discussed, it will be useful to give a short introduction to the green sand mold casting process. These comments are useful because they are, in fact, independent of the particular part geometry.

Sand, combined with a suitable binder, is packed rigidly about a pattern, so that when the pattern is removed, a cavity corresponding to the shape of the pattern remains. Molten metal poured into this cavity and solidified develops a cast replica of the pattern. The sand that forms the mold cavity can be readily broken away for subsequent removal of the casting.

The materials used for pattern making differ greatly in their characteristics and therefore in the applications to which they are best suited. Patterns can be made of wood, metal or other suitable materials, such as wax, polystyrene or epoxy resin. The decision as to what material to use depends on: the stage of development of the design of the casting; the expected production quantity; the dimensional accuracy required; the size and shape of casting; and the molding process to be employed (hand ramming, automatic jolt machine, jolt-squeeze machine, sand slinger, etc.).

Green sand molding is the most widely used of all sand molding processes. A green sand mold is made of sand, clay, water and other materials. ("Green" here means that the sand mixture remains moist.) Green sand molds are not oven dried or otherwise hardened. The mold is used directly without further conditioning.

The problems associated with green sand mold casting fall into roughly two categories: those associated with metal-to-mold interactions and those associated with pouring and feeding the molten metal. Defects during production runs are minimized by careful control of sand properties, metal handling and pouring rates. Table 4-1, taken from <ASM 70>, illustrates typical casting defects that result when sand properties are above or below specified limits. The foundry visited maintains an extensive laboratory for the testing and control of sand properties.

Casting Defects That Result When Sand Properties Are Above or Below Specified Limits

Sand Property	Casting Defects
	Sand Property Above Limit
Moisture content	Blows, scabs, cuts, rough finish, hot tears, porosity, rattails, dirt, high hot strength (difficult shakeout), oxide inclusions, dimensional inaccuracy
Permeability	Poor finish, pinholes, veining, sticky sand, misruns in thin sections
Green strength	Rough finish, difficult shakeout
Green deformation	Scabs
Mold hardness	Blows, scabs, hot tears, difficult shakeout
Dry strength	Hot tears, pinholes, difficult shakeout
Hot strength	Hot cracks, difficult shakeout
Hot deformation	Dimensional inaccuracy
Combustibles content ...	Blows, pinholes
	Sand Property Below Limit
Moisture content	Drops, cuts, poor finish, dirt, broken mold edges
Permeability	Blows, penetration of metal into mold, shakeout, scabs
Green strength	Drops, scabs, cuts and washes, pinholes, dirt, veining, stickiness, dimensional inaccuracy, shrinks
Green deformation	Drops, cuts, dirt
Mold hardness	Drops, cuts, rough finish, penetration of metal into mold
Dry strength	Cuts, dirt
Hot strength	Cuts, poor finish, penetration of metal into mold
Hot deformation	Scabs, rattails, dirt, veining
Combustibles content ...	Poor finish, veining, inaccuracy, burn-on, cuts, rattails

TABLE 4-1

Metal handling and pouring, on the other hand, is more difficult to control. All operations are manual. (Another recurring problem is that metal handlers, also paid on a piecework basis, will try to squeeze more mold fills out of each bucket of molten metal than production standards call for.)

Green sand mold casting is not used to produce parts whose mechanical properties are of prime concern. The internal integrity of such a casting is difficult to control. On the other hand, green sand mold casting is an economical way to produce a part, out of metal, with desired geometric properties. Defects are principally surface properties which effect these geometric properties (either functionally or aesthetically). Internal defects discovered by later machining are a mild embarrassment to the foundry but must be tolerated because there is no economical way to check for them.

Most of the defects listed in Table 4-1 manifest themselves as surface properties that could not have been the result of a legitimate casting operation. Automatic inspection in a batch-oriented foundry would require a system that could detect these surface properties independently of the particular part being viewed.

4.2.1 A SECOND PART IN THE MAKING

The particular part to be discussed is a small shuttle eye (thread guide) used in textile looms. It is one of about 50 different shuttle eyes produced. Some differ slightly in part geometry. Others differ slightly in part dimensions. It is made of gray iron and measures approximately 5 cm by 2.5 cm by 2.5 cm. The size is worth mentioning because this particular casting has a property shared by many green sand mold castings: if one were only interested in making this particular casting, one would not choose a green sand mold process. It is a small part of relatively complex shape. These two factors combine to make green sand molding particularly difficult. It is difficult to achieve mold stability for a part with such small, thin sections. It is difficult to pour the molten

metal so that each mold section is filled uniformly. Rejection rates for the shuttle eye are in excess of 30%. If there were only interest in making this particular part, it would probably be die cast. However, when there is already a green sand mold facility available, a high rejection rate can be tolerated.

Of those rejected, approximately 50% are due to a cold shut defect at the boundary between the two major sections of the casting. A cold shut defect occurs when two streams of molten metal meet in the mold cavity and the temperature differential between them prevents the two streams from welding together properly. It appears as a lapping or layering on the surface of the casting. Figure 4-1 shows a shuttle eye with a cold shut defect.

Approximately 25% of the rejects are due to pinhole defects. Pinholes are small cavities on the surface of the casting caused by bubbles of entrapped gas which reach the surface during solidification. Pinholes can occur anywhere on the surface of the casting although they are predominantly found on upward surfaces of the larger sections of the casting. Figure 4-2 shows a shuttle eye with a pinhole defect.

Cold shuts and pinholes are the two most serious defects associated with this particular (family of) parts. The cold shut of figure 4-1 implies a potential mechanical weakness between the two sections of the casting. But, the major reason for rejection due to either a cold shut or pinhole defect is aesthetic. The surface of the casting seen in figure 4-1 and figure 4-2 is to be used "as cast". No further machining is called for. Thus, those surfaces must "look right" whether or not any imperfection would actually effect the functional performance of the part.

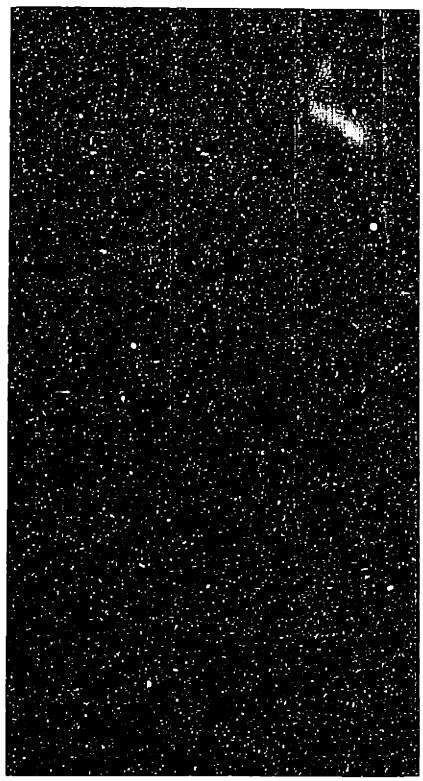

Figure 4-1 Image of a shuttle eye with a cold shut defect at the interface of the two major sections of the casting.

Figure 4-1 Image of a shuttle eye with a cold shut defect at the [illegible] of the two major sections of the casting.

Figure 4-2 Image of a shuttle eye with a pinhole defect.

No other single kind of defect accounts for more than 10% of the rejection rate. The two most predominant remaining defects are misruns (incomplete filling of sections of the mold cavity) and dirt blowouts (loose sand in the mold cavity, which, because of its wetness, explodes on contact with the molten metal). Misruns are more difficult to detect because, in order to decide that a particular section of the mold cavity has not filled completely, it is necessary to have some knowledge of what the part ought to have looked like. Dirt blowouts, on the other hand, are always quite obvious since the "explosion" of wet sand tears up a large portion of the part. A more complete catalogue of typical defects in metal castings is presented in Appendix: B.

5. A LOOK AT GRAIN SIZE ESTIMATION

Grain structure is an important process variable in many casting applications. For example, a gas turbine becomes more efficient as its operating temperature is raised. Therefore, methods are continually being developed to enhance the high-temperature performance of turbine blades and vanes. Grain boundaries play a critical role in determining the high-temperature mechanical properties of a metal. Increases in strength generally are achieved with a reduction in ductility, and, in high-temperature alloys, one manifestation of this phenomenon is a reduction in creep strain prior to failure. Examination of failed material shows that creep cracks are initiated along grain boundaries that make a large angle to the principal stress direction <Sullivan 1976>. Consequently, both grain size and preferred grain orientation significantly alter the mechanical response of a metal. Superior performance is achieved by carefully controlling grain structure in solidification processing.

The most important factor determining grain structure is the heat flow pattern occuring during solidification. The principal determiner of grain size is the rate of cooling during solidification. All else being equal, the faster the cooling the finer will be the resultant grain structure. Areas of a casting that cool very rapidly, and thus have a fine grain structure, are termed *chill zones*. The principal determiner of grain orientation is the direction of heat transfer during solidification. Grains tend to grow parallel to the direction of heat flow. Those that have an elongated aspect ratio are called *columnar grains*.

Castings which have no preferred grain orientation are called *equiaxed* castings. Castings which try for superior mechanical performance by giving a preferred grain orientation with respect to the principal stress

direction are called *directionally solidified (DS)* castings. The turbine blades and vanes considered in this work are examples of equiaxed castings. In the manufacture of these components, three qualitative grain properties are considered good predictors of subsequent mechanical performance (all of these relate to properties of crack propagation):

1. Grain must be sufficiently large.
2. Grain must not have a preferred orientation.
3. There must be no sharp demarcation lines between regions of different grain size.

Considerable effort is required to produce turbine blades and vanes with grain structure satisfying these three properties. Heat flow during solidification naturally occurs out from the leading and trailing edges of the airfoil. The columnar grain which forms as a natural consequence of this heat flow is particularly undesirable since the major stress the airfoil will encounter in service occurs precisely along this direction. Turbine blades and vanes are 100% inspected to verify grain structure.

It is also worthwhile to note that, in other casting applications, a different grain structure may be desired. For example, fine grain is generally desirable in aluminum castings. The coarseness of porosity is proportional to grain size. Consequently, porosity is finer and less harmful in fine grain aluminum castings. Also, certain mechanical properties, such as tensile strength, are usually superior for fine grain aluminum castings. Finally, for aluminum alloys, fine grain minimizes shrinkage, causing castings to be sounder.

5.1 ESTIMATING THE AVERAGE GRAIN SIZE OF METALS

The problem in (non-destructive) grain size estimation is to determine the average grain size of a metal structure, a three-dimensional property, from grain cross sections observed on a two-dimensional surface passing through that structure. It is important to recognize that such an estimation of grain size is not a precise measurement. A metal structure is an aggregate of three-dimensional crystals of varying sizes and shapes. Even if all these crystals were identical in size and shape, the grain cross sections, produced by a random surface of observation through such a structure, would have a distribution of areas varying from a maximum value to zero, depending upon where the surface cuts each individual crystal. Clearly, no two fields of observation can be exactly the same. In an equiaxed casting, the size and location of grains is normally completely random.

The American Society for Testing and Materials recommends three basic methods for grain size estimation (in ASTM Designation: E 112-74 Standard Methods for Estimating the Average Grain Size of Metals[1]):

1. Comparison Procedures:

   Comparison procedures are used for completely recrystallized or cast materials with equiaxed grain. They involve a direct comparison of a representative field of the test specimen with an appropriate collection of standard grain size pictures. The standard which most closely matches the test specimen is selected and the corresponding grain size is recorded.

Comparison procedures are considered convenient for human inspectors and sufficiently accurate for most commercial purposes. However, experience has shown that unless the appearance of the standard grain size series reasonably well approaches that of the sample, errors may occur. Thus, a particular standard grain size series does not adapt well to different alloys or different methods of specimen preparation.

2. Planimetric Procedures:

Planimetric procedures involve counting the number of grains in a known area of the test specimen (usually a circle or rectangle). The sum of all the grains included completely within the known area plus one half the number of grains intersected by the circumference of the area gives the number of equivalent whole grains, measured at the magnification used, within the area. A simple computation, based on an assumed formal relationship between grains per unit area and grains per unit volume, is then used to convert this count into an estimate of the number of grains per square millimeter. Planimetric procedures are more accurate than comparison procedures. Accuracy falls rapidly, however, when grain deviates from an equiaxed structure.

3. Intercept Procedures:

Intercept procedures involve counting the number of grains crossed by a standard pattern applied randomly to the test specimen (usually one or more straight lines or

circles). The length of the test pattern divided by count of the number of points where the test pattern is cut by a grain boundary gives the mean intercept distance (also called mean free path or Heyn intercept). It can be shown that this distance is an unbiased estimate of the mean intercept distance within the solid material in the direction, or over the range of directions, measured.

Intercept procedures are recommended particularly for structures consisting of elongated grains or for structures containing a mixture of actual grain sizes. In the absence of a specific engineering judgment to the contrary, the intercept size is always considered to be the defining grain size value. Indeed, ASTM Committee E-4 on Metallography, under whose jurisdiction the consensus standards for grain size estimation are written, adopted the following as their official position on measurement of grain size:

> *"The referee method should be the intercept method, and the defining equation for grain size number should be that presented in Methods E 112."*
> -- 1974 Report of Committee E-4 on Metallography
> ASTM Proceedings, Volume 75, 1975

Intercept procedures using circular test patterns automatically compensate for departures from equiaxed grain, without giving too much weight to any local portion of the field. Ambiguous intersections at the ends of linear test lines are eliminated. Circular intercept procedures are considered most suitable for grain size estimation in quality control.

In light of these recommendations, the method explored for estimating the average grain size of equiaxed turbine blades and vanes uses the three circle (Abrams) procedure specified in section 11.4 of ASTM Standard E 112-74. The goal of this work is to demonstrate that a machine vision system is capable of the performance and accuracy called for by an existing industry standard for grain size estimation. First, the Abrams procedure is outlined and then the details of the algorithm developed to implement it are presented. The techniques described for grain size estimation are motivated by the particular application and may not seem directly related to the more general issues underlying this thesis. At the conclusion of this chapter, it will be pointed out how the implementation also possesses the flexibility required to perform grain size estimation from views of arbitrarily curved surfaces. This discussion will attempt to tie the problem of grain size estimation down to the more general theory underlying this thesis.

5.2 THE THREE CIRCLE (ABRAMS) PROCEDURE

In the three circle (Abrams) procedure, it is assumed that the surface of observation is planar. This assumption of planarity is implicit in the computation used to infer the three-dimensional grain size of an equiaxed casting from measurements on a two-dimensional surface of observation. The Abrams procedure is an intercept procedure. The test pattern consists of three concentric, equally spaced, circles designed to cover a total circumference of 500 millimeters on the sample surface. (A little mathematical figuring will show that the diameters of these circles are 26.53 mm., 53.05 mm. and 79.58 mm. respectively.) The procedure is as follows:

1. Perform a cursory examination of the specimen to roughly estimate its grain size. Using this rough estimate, select an image magnification that will yield approximately 100 grain crossings over the 500 mm. three circle test pattern.
2. Randomly select one field for measurement and apply the test pattern to that field. If the count of grain crossings for the first application is less than 70 or more than 140, discard the result and adjust the image magnification accordingly. Repeat this step until the count is in the acceptable working range.
3. Randomly select four more fields for measurement and apply the test pattern to each field. A total of five such counts is considered sufficient to compute grain size to within 1/2 a standard ASTM grain number. If additional accuracy is required, additional fields may be sampled.

The grain size, as measured above, is indicated as a count of grain crossings over a known path length. Such a value is inconvenient for subsequent use. Hence, this count is normally reexpressed in terms of such (industry standard) quantities as nominal diameter, Feret's diameter, intercept size, specific surface, grains per unit volume, or ASTM micro-size or macro-size number.

The ASTM grain number is defined as follows:

$$G = 10.0 - 2 \log_2(L)$$

where L is the mean intercept distance which, for the three circle (Abrams) procedure, is given by:

$$L = \frac{\text{length of path (in millimeters)}}{\text{total number of grain crossings}}$$

If L is determined in millimeters at an image magnification of 100X, then the resulting G is called the *micro-grain number*. If L is determined in millimeters at an image magnification of 1X, then the resulting G is called the *macro-grain number*. The program discussed below which implements the Abrams procedure has sufficient accuracy to determine the statistically correct ASTM grain number for samples in the recommended working range. (The program was tested and calibrated using sample plates available from the American Society for Testing and Materials as an adjunct to standard E 112-74.) When a particular sample specimen was made to fall outside the recommended working range, the program was generally robust enough to be able to suggest an appropriate change to image magnification to bring the sample within the desired range.

5.3 A PROGRAM FOR DETERMINING ASTM GRAIN NUMBER

The initial discussion presented here focuses on the problem of applying the three circle (Abrams) procedure to images of a planar surface viewed in a direction normal to that surface. The reason for this is twofold. First, the applicable grain size measure, as defined in ASTM standard E 112-74, demands that the viewed surface be planar. Second, by considering the planar surface to be viewed normally, one avoids the additional mathematics required to account for the foreshortening of path length due to an oblique viewing angle.

The program discussed makes use of simple edge mask filters to

determine grain boundaries crossed by a circular test pattern. Unlike other simple detection schemes, however, the program does not make decisions based upon any single measurement. Rather, grain crossings are determined by comparing the relative response over an ensemble of different mask sizes. This makes the program usable over a broader range of image magnifications and grain sizes while, at the same time, making it less susceptible to false indications due to noise.

First, the method used to determine grain crossings along a circular path on the surface is summarized. Second, the performance of the each portion of the program is analyzed in more detail using synthesized data. Finally, an example of the program applied to an etched section of an actual turbine vane is provided.

The algorithm for determining grain crossings along a circular path on the surface can be summarized as follows:

1. DATA ACQUISITION:

   The image is sampled along a circle centered at image point (x_c, y_c) and corresponding to a surface diameter of d millimeters. The resulting intensity values are stored as a one-dimensional (circular) array called INTENSITY.

2. DATA PRE-PROCESSING:

   Three different edge detection filters are applied to the intensity values. Each edge filter is of the form:

   $$F_n(i) = (I(i+1)+I(i+2)+\ldots+I(i+m)) - (I(i-1)+I(i-2)+\ldots+I(i-m))$$

   where I(i) denotes the i^{th} element of the array INTENSITY. The results are stored as three new one-dimensional (circular) arrays, called FILTER1, FILTER2 and FILTER3 respectively. Each FILTER array corresponds to a different choice of the value m.

3. DATA COMPRESSION:

Each array FILTERn is processed to produce a list L_n of the form:

L_n = ((TYPE1 INDEX1 VALUE1) ... (TYPEk INDEXk VALUEk))

Each element of the list L_n denotes a local extremum in the corresponding FILTERn array. TYPE is MAXIMUM or MINIMUM, INDEX is the index of the extremum (in array FILTERn) and VALUE is the value (height) of the extremum. The three lists L_1, L_2 and L_3 are then merged into a single list

L = ((TYPE1 INDEX1) (TYPE2 INDEX2) ... (TYPEm INDEXm))

Again, TYPE is MAXIMUM or MINIMUM and INDEX is the index of the extremum. L contains an element for each local extremum found in either L_1, L_2 or L_3.

4. SYNTACTIC ANALYSIS:

The list L, together with the lists L_1, L_2 and L_3 are passed off to a syntactic parser. Basically, the job of the parser is to look at each extremum in L and decide whether it corresponds to an actual grain crossing. The parser consists of a collection of parsing routines which may accept a given extremum as a grain crossing. Each parsing routine is given initial (matched) pointers into L_1, L_2 and L_3. It can then look both forward and backward from those pointers using any or all of the lists L_1, L_2 or L_3 to compare the responses measured by the FILTER1, FILTER2 and FILTER3 arrays. If the responses are consistent with the type of edge being parsed, then the peak is accepted as a grain crossing.

For planar surfaces viewed normally (i.e., $\theta = 0$), the data acquisition problem is straightforward. Circles on the object surface will project to circles in the image. To compute the ASTM grain number, it is

only necessary to calibrate the imaging hardware with respect to magnification. The slow-scan vidicon camera (Spatial Data System 108) used to digitize images for this work has a differing resolution in image coordinates x and y. Thus, two calibration measurements were performed: one to determine A, the number of pixels per millimeter in the horizontal (left-right) direction and one to determine B, the number of pixels per millimeter in the vertical (up-down) direction. For a particular imaging situation, this calibration can either be done manually or automatically (using an appropriately scaled "ruler" in the field of view). Thus, in order to scan a circle on the surface centered at image point (x_c, y_c) and of diameter d millimeters, one actually scans the image ellipse described parametrically by:

$$x(\theta) = x_c + A\ r\ \cos(\theta)$$

$$y(\theta) = y_c + B\ r\ \sin(\theta)$$

where $r = d/2$, the radius of the circle in millimeters and $0 \leq \theta < 2\pi$.

The raw intensity values thus acquired are typically quite noisy and hence difficult to interpret directly. The simple edge mask filters used here are a common pre-processing technique to enhance effects due to edges and suppress effects due to noise. <Shirai 75> used the same filter in his program for tracking edges of polyhedra. <Marr 76b> uses a similar type of edge mask, extended in the second dimension, as one of the two basic operations in the computation of the primal sketch. The contribution of this work is not so much in the use of the simple edge mask filters but in the use of multiple masks of varying support widths. For any particular choice of m, the filter array computed by

$$F_m(i) = (I(i+1)+I(i+2)+\ldots+I(i+m)) - (I(i-1)+I(i-2)+\ldots+I(i-m))$$

forces an inevitable trade-off between noise immunity and resolution. For

small m, there will be a greater number of false peaks due to noise. For large m, there will be a loss of resolution as closely spaced edges become smeared together (especially in situations where adjacent edges have intensity gradients with the same sign).

For any given image, it is usually possible to hand-pick a choice for m that works reasonably well. In the first version of the grain size estimation program, a single FILTER array was computed corresponding to a single choice of m. Unfortunately, no single value of m proved satisfactory over the range of grain sizes called for in ASTM standard E 112-74. With three filter arrays, corresponding to three choices of m, superior noise immunity and resolution is achieved. The existence of a peak in one of the three filter arrays is used to hypothesize the presence of an edge. There may not be matching peaks in the other two filters arrays. But, if the values of the other two filter functions at the position of the peak are as predicted by the hypothesized edge, then the existence of that edge can be reliably asserted.

Figure 5-1 illustrates edge mask pre-processing applied to a single idealized grain crossing. Figure 5-1(a) shows the intensity profile corresponding to a step in intensity. Figure 5-1(b), figure 5-1(c) and figure 5-1(d) show, respectively, the filter profiles corresponding to choices of m_1, m_2 and m_3 where the ratio $m_1:m_2:m_3$ is equal to 1:2:3. Now, the step in intensity produces a simple peak in each filter array. The heights and widths of the corresponding peaks are also in the ratio $m_1:m_2:m_3$.

Figure 5-2 illustrates edge mask pre-processing applied to the same idealized grain crossing of figure 5-1. In this case, however, each intensity value in figure 5-2(a) has been perturbed by adding a random

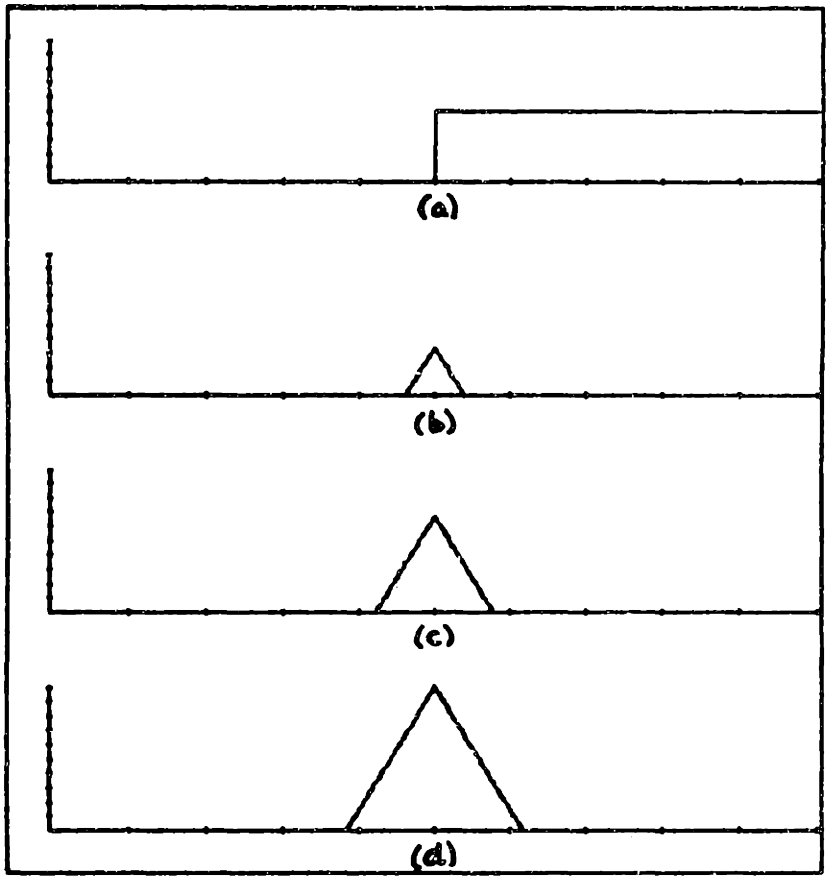

Figure 5-1 Edge mask pre-processing applied to an idealized intensity step. Figure 5-1(a) is the intensity profile. Figures 5-1(b), (c) and (d) are the mask results obtained when the widths of the masks are in the ratio 1:2:3.

(white) noise value (in the range 0 - h, where h is the height of the original step in intensity). Figure 5-2(b), figure 5-2(c) and figure 5-2(d) show, respectively, the filter profiles corresponding to choices of m_1, m_2 and m_3 where the ratio $m_1:m_2:m_3$ is again equal to 1:2:3. It is observed that all three of the filter profiles have successfully isolated the edge due to the step in intensity from the effects due to noise. The height of each peak in the filter arrays preserves the (approximate) ratio 1:2:3. So far, there seems to be no advantage to having computed three separate filter arrays.

Figure 5-3 illustrates the superior noise immunity that can be obtained using three separate filter arrays. Figure 5-3(a) again corresponds to the idealized grain crossing of figure 5-1 perturbed by noise. For figure 5-3(a), however, the magnitude of the noise was increased to the range 0 - 1.5h, where h is again the height of the original step in intensity. Figure 5-3(b), figure 5-3(c) and figure 5-3(d) show, respectively, the filter profiles computed using the same choices for m_1, m_2 and m_3 used in figure 5-2. There is a peak in the FILTER1 array corresponding to the underlying step in intensity. This peak, however, hardly "stands out" from the other peaks (due to noise) found in FILTER1. Note, however, that the height of the peaks in the three filter arrays corresponding to the underlying step in intensity preserve the (approximate) ratio 1:2:3. Other (false) peaks in FILTER1 do not preserve this ratio across the three filter arrays. Thus, they can be reliably rejected.

At this point, one might argue that the value chosen for m_1 is simply too small for the noise levels present in the example of figure 5-3. The next two figures are presented to illustrate that such a small value for m_1

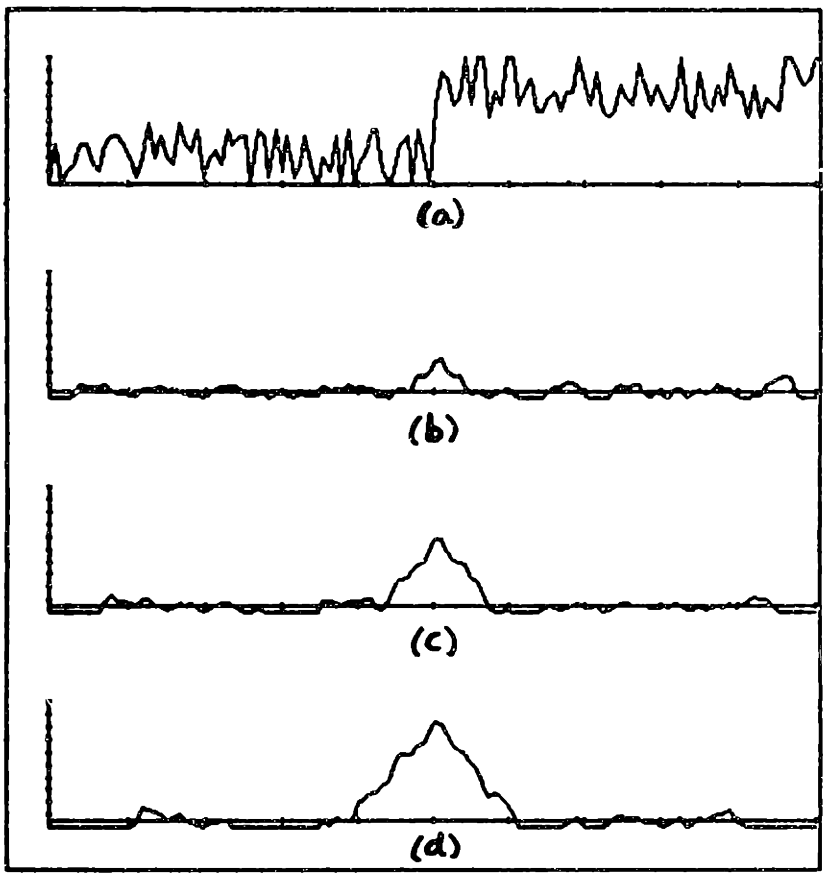

Figure 5-2 Edge mask pre-processing applied to a noisey intensity step. Figure 5-2(a) is the intensity profile. Figures 5-2(b), (c) and (d) are the mask results obtained when the widths of the masks are in the ratio 1:2:3. Each mask has isolated the step and the approximate ratio of the peak heights is preserved.

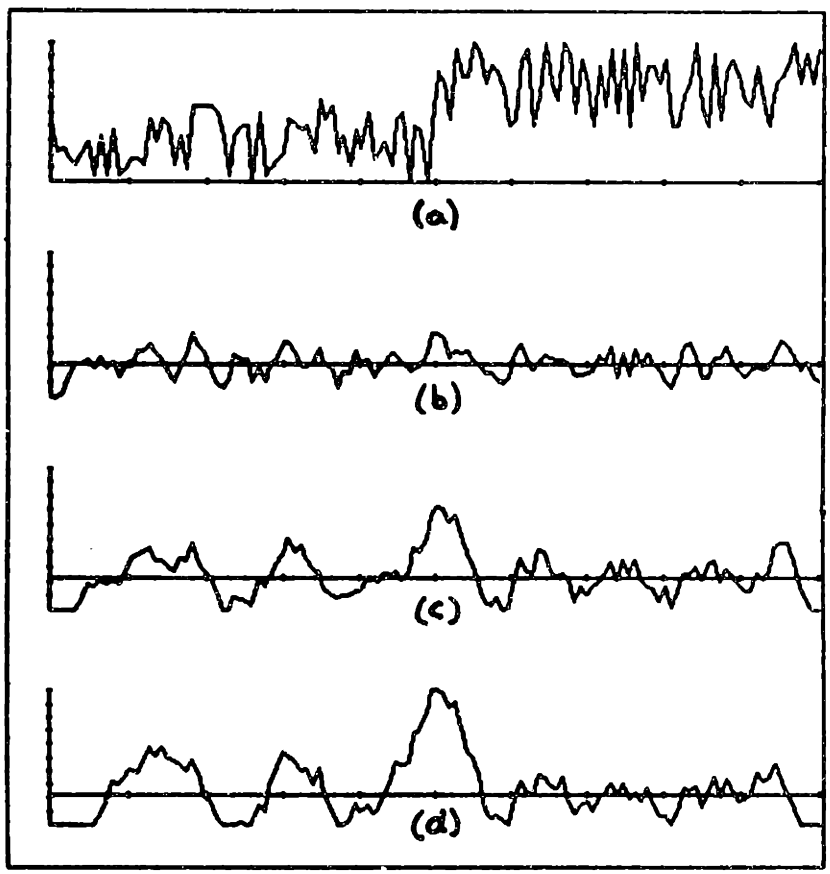

Figure 5-3 Edge mask pre-processing applied to a noisier intensity step. Figure 5-3(a) is the intensity profile. Figures 5-3(b), (c) and (d) are the mask results obtained when the widths of the masks are in the ratio 1:2:3. In figure 5-3(b), the peak due to the step is no higher than peaks due to noise. Nevertheless, the approximate ratio of the peak heights at that point confirms the presence of the step.

is necessary to resolve closely spaced edges. Figure 5-4 illustrates an idealized example corresponding to two closely spaced grain crossings such that the step in intensity across each boundary has the same sign. Figure 5-4(a) shows the intensity profile. Figure 5-4(b), figure 5-4(c) and figure 5-4(d) show, respectively, the filter profiles corresponding to the same choices of m_1, m_2 and m_3 used above. FILTER1 clearly resolves the two steps in intensity. FILTER2 has begun to smear the two peaks together. FILTER3 has smeared the two peaks together to the point that it is no longer possible to resolve them. Note, however, that the values in the three filter arrays, at each peak position in the FILTER1 array, preserve the approximate ratio 1:2:3. Thus, the presence of two separate grain crossings, as hypothesized by the two peaks in the FILTER1 array, can be reliably asserted, not due to the presence of corresponding peaks in the FILTER2 and FILTER3 arrays but rather due to the corresponding values in the FILTER2 and FILTER3 arrays.

Figure 5-5 illustrates the same example as figure 5-4 with the addition of noise (in the range 0 - h, where h is the height of each step in intensity). Again, the presence of separate grain crossings is hypothesized by the two peaks in the FILTER1 array and verified by the corresponding values in the FILTER2 and FILTER3 arrays. Thus, the computation of filter arrays corresponding to three different choices of m provides the basis for a method for determining grain crossings which gives superior noise immunity without a corresponding loss in ability to resolve closely spaced edges.

Initially, however, computing the three FILTER arrays simply generates three new arrays of numbers. The next important step in the algorithm is to convert these FILTER arrays into a form more amenable to the kind of

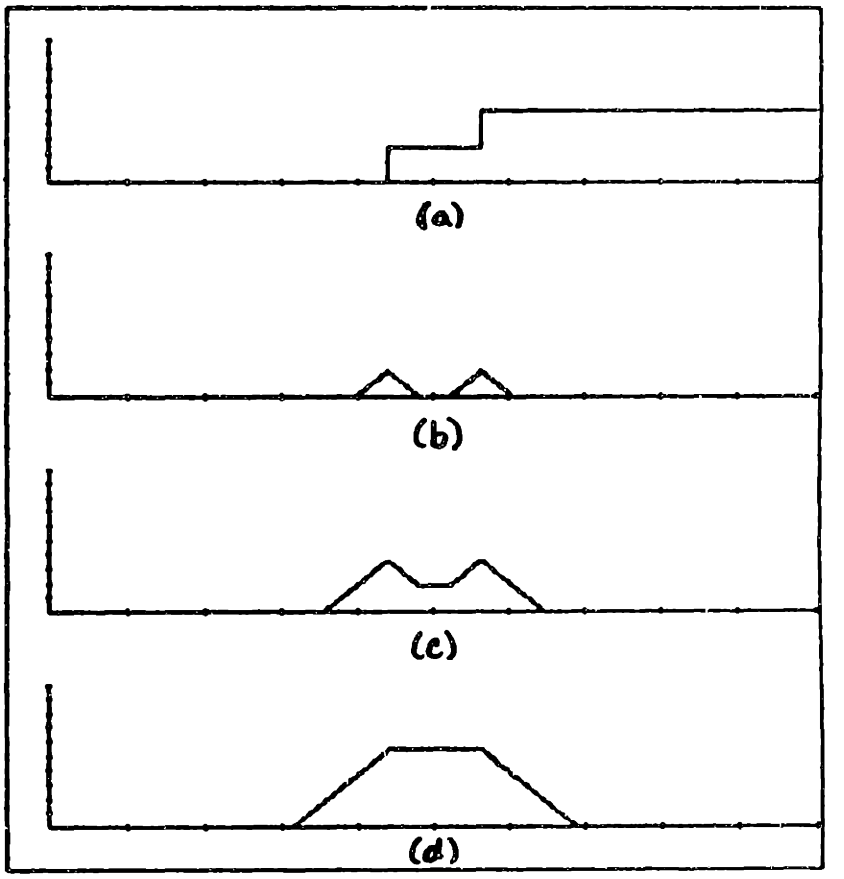

Figure 5-4 Edge mask pre-processing applied to two closely spaced idealized intensity steps (of the same sign). Figure 5-4(a) is the intensity profile. Figures 5-4(b), (c) and (d) are the mask results obtained when the widths of the masks are in the ratio 1:2:3.

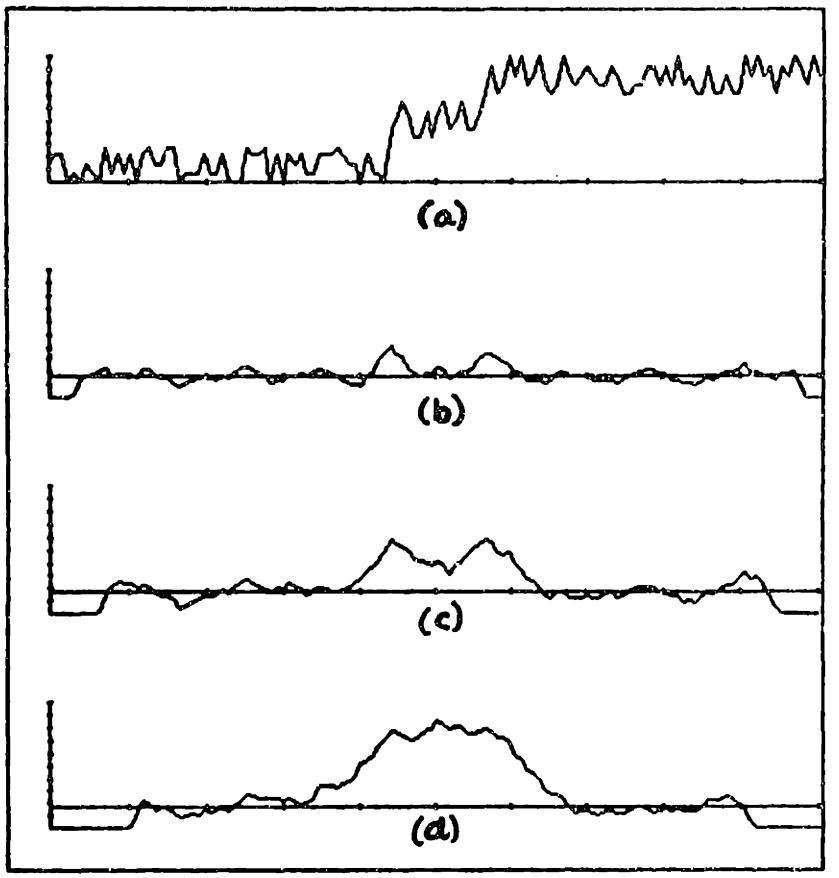

Figure 5-5 Edge mask pre-processing applied to two noisy closely spaced intensity steps (of the same sign). Figure 5-5(a) is the intensity profile. Figures 5-5(b), (c) and (d) are the mask results obtained when the widths of the masks are in the ratio 1:2:3.

analysis presented informally in the discussion of figure 5-1 through figure 5-5 above.

The computation of each list L_n, where

$$L_n = ((\text{TYPE1 INDEX1 VALUE1}) \ldots (\text{TYPEk INDEXk VALUEk}))$$

serves two functions. First, it represents each FILTER array as a set of symbolic assertions which serves as the appropriate input to the syntactic parser. Second, it can also be properly viewed as a data compression process. The list L_n carries information only about the position, height and type of each local extremum (in the corresponding FILTERn). In fact, one can throw away the INTENSITY and FILTER arrays at this point. It is true that subsequent analysis will require values for $F_n(i)$ where i is not a local extremum of the particular F_n, but these values can be successfully approximated as a linear interpolation between the values at the extrema neighboring i. Saying the same thing again, each L_n used in the subsequent syntactic analysis corresponds to a "stylized" $F_n(i)$ for which neighboring local extrema are joined by straight lines. (Note: In the current implementation, it turns out to be more convenient to actually refer back to the original FILTER arrays when needed. A scheme based on linear interpolation between peaks has also been tried with no loss of accuracy.)

The three lists L_1, L_2 and L_3 are also merged into the single list

$$L = ((\text{TYPE}_1\ \text{INDEX}_1)\ (\text{TYPE}_2\ \text{INDEX}_2) \ldots (\text{TYPE}_l\ \text{INDEX}_l))$$

The list L collects, in one place, all the peaks found in either of the arrays FILTER1, FILTER2 and FILTER3. This list feeds the parser candidate positions for possible grain crossings. The lists L_1, L_2 and L_3 are available to each individual parsing routine for examining particular features within each filter profile and for comparing responses across filter profiles. The process of parsing consists of passing successive

peaks from L off to the individual parsing routines (which define the class of edges that will be accepted by the parser). When invoked, each individual parsing routine is also passed pointers to the closest matching peak in each of L_1, L_2 and L_3. These individual routines may look forward or backward in any or all of the L_1, L_2 and L_3 in an effort to parse a candidate peak. A peak is rejected as an edge if it is rejected by all of the parsing routines present in the system. A peak is accepted as an edge when it is accepted by one of the individual parsing routines present in the system. If a peak is accepted by one of the individual parsing routines, it is the responsibility of that routine to position the pointer to L past any adjacent peaks that have already been accepted as part of the edge. Parsing is complete when there are no more candidate peaks to consider.

The simplest example of a parsing routine is STEP-UP which "accepts" grain crossings corresponding to a simple upwards step in intensity (of the sort discussed in figure 5-1 through figure 5-5). STEP-UP is invoked whenever a peak of type MAXIMUM occurs in the list L. STEP-UP, like all the individual parsing routines, is passed the four arguments: i, i1, i2 and i3 where i is the index of the candidate peak (of type MAXIMUM) from L and i1, i2 and i3 are, respectively, the indices in FILTER1, FILTER2 and FILTER3 of the peak nearest to i (of type MAXIMUM). STEP-UP "accepts" a grain crossing at index i if:

(1) $F_1(i) > (\text{THRESHOLD} * m_1)$

(2) $F_1(i)/m_1$, $F_2(i)/m_2$ and $F_3(i)/m_3$ have "about the same value".

(STEP-UP is so simple that it does not make use of any forward or backward analysis of the three lists L_1, L_2 and L_3. Below, another parsing routine,

PULSE-UP, will be presented that does make use of forward and backward analysis.) THRESHOLD is a global threshold which establishes the minimum step size to be considered significant. Alas, it was not possible to rid the program entirely of thresholding operations. The value of THRESHOLD, however, is not critical. The actual value used in the program examples is THRESHOLD = 3 which is slightly below the average noise level of the imaging hardware. The presence of a threshold is required to rule out spurious combinations of peaks (at the level of noise) which happen to satisfy (2) above. Finally, a set of numbers (v_i) is said to have "about the same value" if the absolute value of the difference between any two of them is less than one half the absolute value of the one with largest magnitude. This definition corresponds to a rather *ad hoc* definition of qualitative equality. A more rigorous definition would have to take into account the signal to noise properties of the imaging hardware. Again, however, the particular definition of "about the same value" is not critical. In general, for choices of m_1, m_2 and m_3 in the ratio 1:2:3, there is a good separation between peak heights of "about the ratio 1:2:3" and peak heights corresponding to noise. The actual boundary chosen is not of critical importance.

The above parsing routine STEP-UP, together with a similarly defined routine STEP-DOWN, is sufficient to perform the syntactic analysis required to apply the three circle (Abrams) to alloy specimens that can be prepared using a *contrast etch* technique. In a contrast etch, the cross section of each grain is etched so that surface reflectivity becomes a function of grain orientation. Thus, individual grains appear as regions of (approximately) homogeneous intensity. Grain boundaries appear as contrast boundaries between adjacent regions. Other alloy specimens are more

appropriately prepared using a *flat etch* technique. In a flat edge, the cross section of each grain is not affected. Rather, the boundaries themselves are etched. Regions within the confines of a grain boundary are unaffected while the grain boundaries themselves appear as (dark) lines on the specimen.

The turbine blade and vane specimens used in this work were prepared using a contrast etch technique. On the other hand, the standard plates obtained from the American Society for Testing and Materials correspond to samples prepared using a flat etch technique. Thus, additional parsing routines were also included to handle grain crossings which appear as thin lines in the image. Figure 5-6 illustrates edge mask pre-processing applied to a single idealized grain crossing from a specimen prepared using a flat etch technique. Figure 5-6(a) shows the intensity profile corresponding to a narrow pulse in intensity. Figure 5-6(b), figure 5-6(c) and figure 5-6(d) show, respectively, the filter profiles corresponding to choices of m_1, m_2 and m_3 where the ratio $m_1:m_2:m_3$ is once again equal to 1:2:3. The pulse in intensity produces a doublet in each filter array. The positive peak corresponds to the leading edge of the pulse and the negative peak corresponds to the trailing edge of the pulse. Note that if the width, w, of the pulse is small compared to m_1, m_2 and m_3, then the height of each positive and negative peak is constant in each of the FILTER1, FILTER2 and FILTER3 arrays. It is, in fact, equal to the area under the pulse. Note, also, that the transition from positive peak to negative peak occurs over the width w, again independent of which filter array is considered.

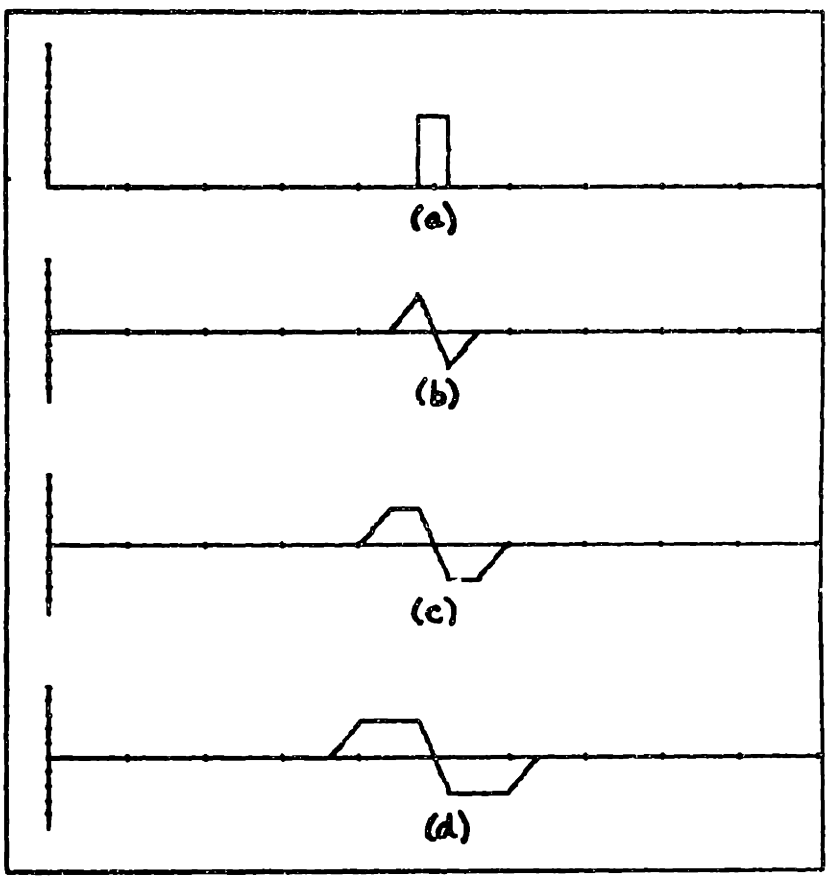

Figure 5-6 Edge mask pre-processing applied to an idealized pulse (two closely spaced intensity steps of opposite sign). Figure 5-6(a) is the intensity profile. Figures 5-6(b), (c) and (d) are the mask results obtained when the widths of the masks are in the ratio 1:2:3.

Figure 5-7 illustrates edge mask pre-processing applied to the same idealized grain crossing of figure 5-6. In this case, however, each intensity value in figure 5-7(a, has once again been perturbed by adding random noise (in the range 0 - 0.5h, where h is the height of the pulse in intensity). Figure 5-7(b), figure 5-7(c) and figure 5-7(d) show, respectively, the filter profiles corresponding to the same choices of m_1, m_2 and m_3 used above. The same qualitative observations hold true. The pulse in intensity produces a doublet in each filter array. The magnitude of each positive and negative peak is independent of the choice of m_1, m_2 and m_3. The width of the transition from positive peak to negative peak in each filter array approximates the width of the original pulse in intensity. These observations form the basis for the parsing routine PULSE-UP used to "accept" grain crossings from a specimen prepared using a flat etch technique.

PULSE-UP is also invoked whenever a peak of type MAXIMUM occurs in the list L. PULSE-UP is passed the four arguments: i, i1, i2 and i3 where i is the index of the candidate peak (of type MAXIMUM) from L and i1, i2 and i3 are, respectively, the indices in FILTER1, FILTER2 and FILTER3 of the peak nearest to i (of type MAXIMUM). PULSE-UP "accepts" a grain crossing at index i if:

(1) The value, V+, of FILTER1 at the closest (previous) peak, I+, of type MAXIMUM is greater than (THRESHOLD * m_1).

(2) The value, V-, of FILTER1 at the closest (following) peak, I-, of type MINIMUM is less than -(THRESHOLD * m_1).

(3) In going backward in L1 from the positive peak at I+, a

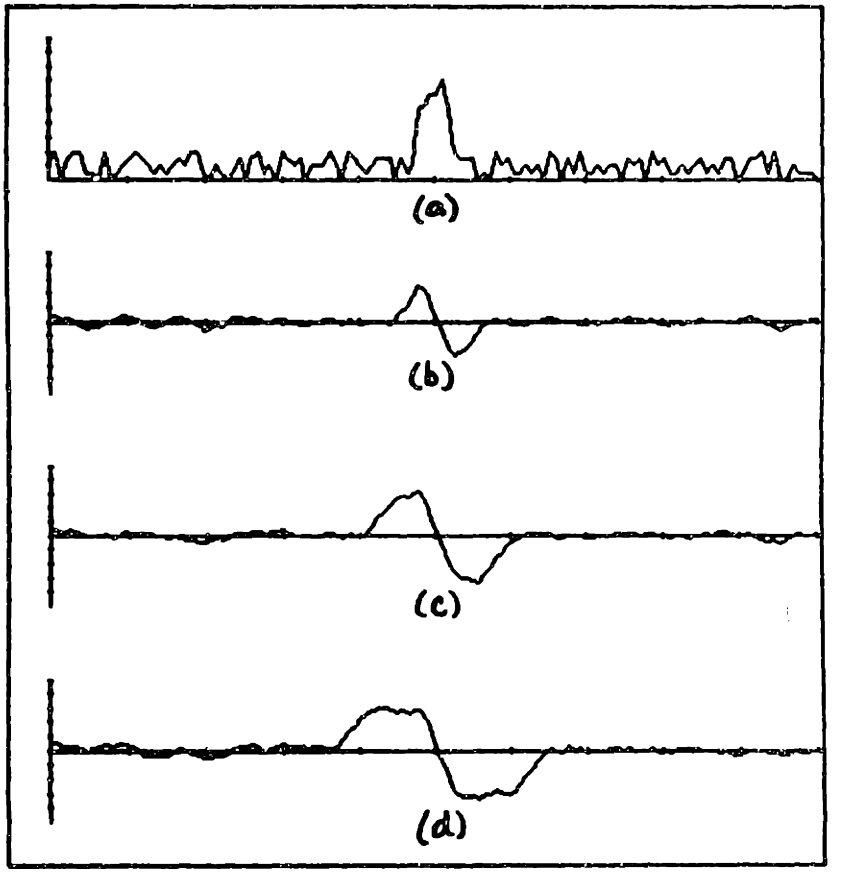

Figure 5-7 Edge mask pre-processing applied to a noisy pulse (two closely spaced noisy steps of opposite sign). Figure 5-7(a) is the intensity profile. Figures 5-7(b), (c) and (d) are the mask results obtained when the widths of the masks are in the ratio 1:2:3.

value below (THRESHOLD * m_1) or V+ - (THRESHOLD * m_1), whichever is greater, is encountered before a value above V+.

(4) In going forward in L1 from the negative peak at I-, a value above -(THRESHOLD * m_1) or V- + (THRESHOLD * m_1), whichever is less, is encountered before a value below V-.

(5) Let the distance between the MAXIMUM peak at I+ and the MINIMUM peak at I- be w. Then:

a) w is less than m_3.

b) $F_1(I+)/\min(w,m_1)$, $F_2(I+)/\min(w,m_2)$ and $F_3(I+)/w$ have "about the same value".

c) $F_1(I-)/\min(w,m_1)$, $F_2(I-)/\min(w,m_2)$ and $F_3(I-)/w$ have "about the same value".

THRESHOLD is the same global threshold referred to in the definition of STEP-UP. Again, (1) and (2) rule out spurious doublets occurring at the level of noise. (3) and (4) make sure that the doublet in FILTER1 has well defined leading and trailing edges. Otherwise, a local zero crossing which actually is a part of a more global feature may incorrectly be accepted as a grain crossing. (5a) makes sure that the separation between the MAXIMUM and MINIMUM peaks is small enough, compared to the values of m_1, m_2 and m_3, so that the doublet can be considered as corresponding to a single pulse in intensity, rather than to two separate steps in intensity. (5b) and (5c) are the key steps in PULSE-UP. (1), (2), (3), (4) and (5a) serve only to eliminate cases which otherwise behave as if they corresponded to a pulse in intensity. (5b) and (5c) check, respectively, that the height of the MAXIMUM peaks and the height of the MINIMUM peaks in each of FILTER1,

FILTER2 and FILTER3 have "about the same value". In the discussion of figure 5-6, it was pointed out that if w is small compared to m_1, m_2 and m_3, then the magnitude of each positive and negative peak is constant in each of the FILTER1, FILTER2 and FILTER3 arrays. Here, a little more generality is allowed. If w is less than m_i, then the expected height of each peak in FILTERi is h * w. On the other hand, if w is greater than m_i, then a pulse of width w looks to FILTERi like two separate opposite steps in intensity and the expected height of each peak in FILTERi is h * m_i.

The above parsing routine PULSE-UP, together with a similarly defined routine PULSE-DOWN, is sufficient to perform the syntactic analysis required to apply the three circle (Abrams) procedure to alloy specimens that are prepared using a flat edge technique. PULSE-UP and PULSE-DOWN are also useful for alloy specimens prepared using a contrast etch. The presence of PULSE-UP and PULSE-DOWN gives the program superior ability to resolve closely spaced intensity steps in situations where the adjacent steps have intensity gradients with the opposite sign. Of course, in the case of samples prepared using a contrast etch, a peak "accepted" by PULSE-UP or PULSE-DOWN counts as two grain crossings rather than as one.

A real example is now discussed. Figure 5-8(a) shows a macro-etched section of a turbine airfoil. The airfoil has been prepared using a contrast etch. Superimposed upon the grain pattern is the three circle test pattern used in the analysis. (For illustrative purposes, the test pattern is given as three concentric circles in the image rather than as the corrected three ellipses.) Crosses marked along the three circles indicate positions where grain crossings were detected by the program. Figure 5-8(b) illustrates the results obtained when the program analyzed the middle circle of figure 5-8(a).

Figure 5-8(b) consists of five graphs. In each case, the abscissa corresponds to angular position (0 to 2π radians) along the test circle. The first graph shows the intensity values obtained with the vidicon camera. The next three graphs show the filter values computed for case $m_1 = 5$, $m_2 = 10$ and $m_3 = 15$ respectively. The fifth graph simply marks, for reference purposes, the points at which grain crossings were detected.

A good example of how the use of three different choices of m helps can be seen in the second and third (from the left) grain crossings marked in figure 5-8(b). The FILTER1 graph does have two (negative) peaks at those points but their magnitude is not much above that of the noise. The FILTER2 graph shows two distinct (negative) peaks at the points marked. The FILTER3 graph, on the other hand, has smeared the two peaks together in such a way that no program could reasonably be expected to disambiguate them. Nevertheless, the relative magnitudes of the matched values in the three graphs are consistent with the two crossing interpretation indicated.

5.4 DISCUSSION

Flexibility as well as accuracy must be regarded as keys to success with any automatic inspection system. This chapter describes an important step forward in the domain of castings inspection. First, it has been demonstrated that an automatic inspection system is capable of the accuracy required to implement an existing industry standard for grain size estimation. A certain amount of flexibility has also been demonstrated in the program's ability to maintain high noise immunity without a corresponding loss in resolution.

In this section, the problem of grain size estimation is related to the more general theme of the thesis. The goal is to show how the

(a)

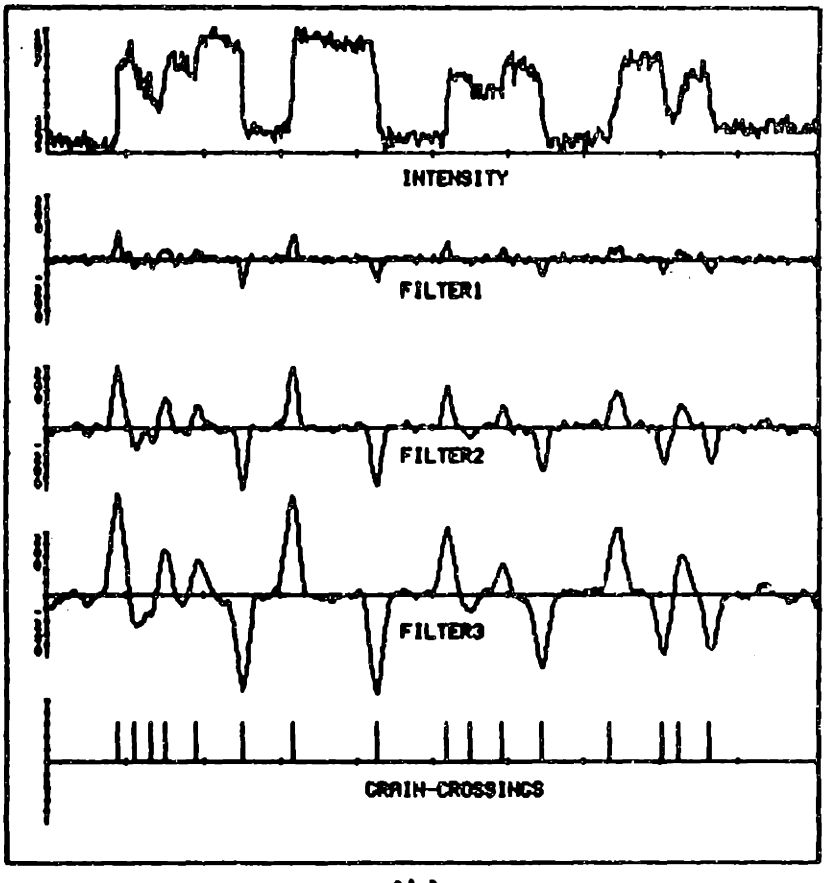

(b)

Figure 5-8 Three circle (Abrams) procedure applied to macro-etched section of turbine airfoil. Figure 5-8(a) marks the grain crossings detected using a three concentric circle test pattern. Figure 5-8(b) shows the analysis of the intensity profile corresponding to the middle circle of figure 5-8(a).

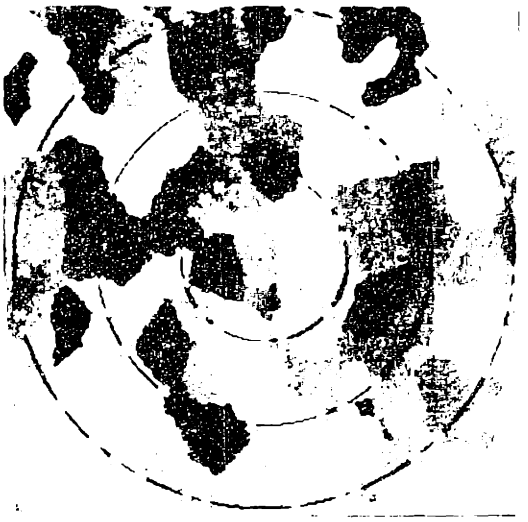

(a)

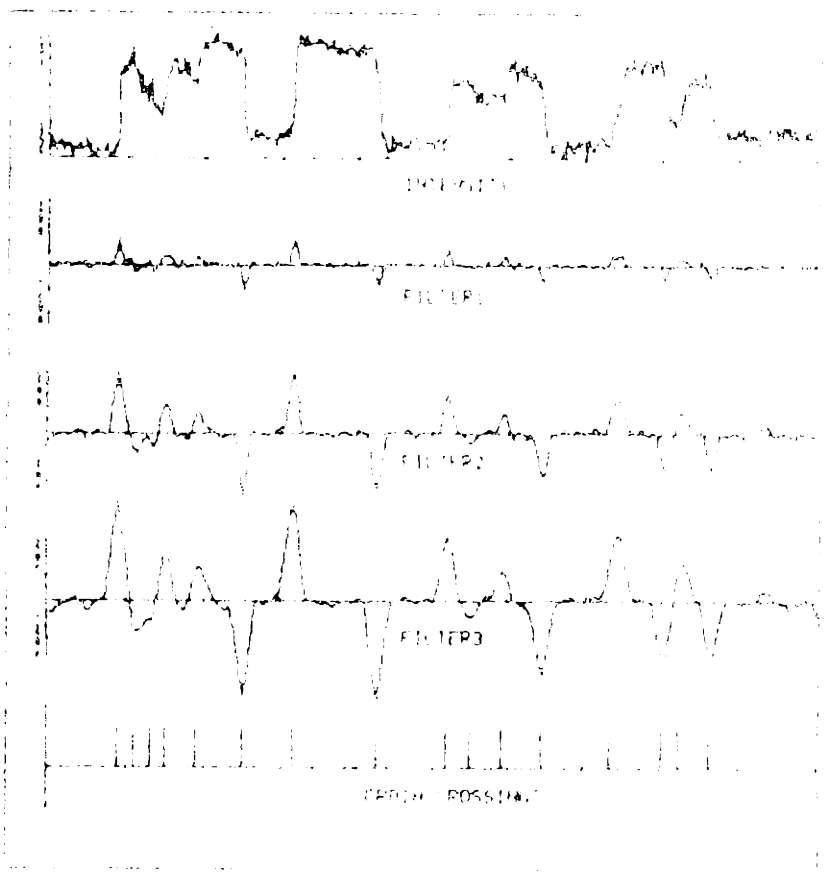

(b)

Figure 5-8 Three circle (Abrams) procedure applied to macro etched section of turbine airfoil. Figure 5-8(a) marks the grain crossings detected using a three concentric circle test pattern. Figure 5-8(b) shows the analysis of the intensity profile corresponding to the middle circle in figure 5-8(a).

techniques developed in this chapter can be made flexible enough to estimate grain size over a wide variety of part surfaces. A word of caution is in order, however. The discussion will center on the ability to make the measurements required by ASTM standard E 112-74 to views of curved surfaces and not on the validity of those measurements. It is not a goal here to develop a theory for estimating the three-dimensional grain size of metals from arbitrary two-dimensional surfaces of observation. (ASTM standard E 112-74 develops the appropriate statistical theory for planar surfaces of observation and it will be left at that.)

Suppose one applies the three circle (Abrams) procedure to sections of an image of an arbitrary curved surface of observation. A change in the measured grain size from one region of the image to another may be due to either an actual change in grain size or to an apparent change produced by a change in the view angle from the one region to the other. In order to measure actual changes in grain size, it is necessary to explicitly account for the foreshortening effect of the view angle at each image point.

In a planimetric procedure, which involves counting the number of grains in a known area of test specimen, one can explicitly account for the effect of foreshortening if one knows the view angle e at each image point. The surface area corresponding to a test region R in the image is given by:

$$A = \iint_R \sec(e)\, dxdy$$

where, once again, it is assumed that the image is an orthographic projection scaled so that image coordinates (x,y) correspond to object coordinates (x,y)

In an intercept procedure, which involves counting the number of grains crossed by a one-dimensional curve on the test specimen, one can explicitly account for the effect of foreshortening if one knows the gradient (p,q) at each image point. The path length ds corresponding to a (small) movement [dx,dy] in the image is given by:

$$ds^2 = [dx\ dy] \begin{bmatrix} p^2+1 & pq \\ pq & q^2+1 \end{bmatrix} \begin{bmatrix} dx \\ dy \end{bmatrix} \qquad (5.4.1)$$

Equation (5.4.1) has the interpretation that the component of ds in the direction of steepest descent is foreshortened by the factor cos(e) while the component of ds in the direction of constant view angle e is unchanged (see Appendix: A.5).

Thus, in order to interpret the measurements derived by applying the three circle (Abrams) procedure to sections of an image of an arbitrary curved surface of observation, it is necessary to have the viewer-centered representation for surface shape developed in Chapter: 2. Conversely, with such a representation, the interpretation becomes straightforward.

The macro-etched turbine vane used in the example above was prepared using a contrast etch. A contrast etch makes the surface photometric function of the casting non-homogeneous. Thus, in order to determine the viewer-centered representation required by (5.4.1), it would be necessary to first (pre)view an unetched part (or have the representation supplied externally). On the other hand, for parts prepared using a flat etch, these two operations can be combined if the method for determining the viewer-centered representation is modified to ignore the dark markings (corresponding to the grain boundries).

Fortunately, for airfoils, additional simplifications can be exploited. Airfoils can be approximated as singly curved surfaces. There is negligible curvature in directions parallel to the leading and trailing edges. Directions orthogonal to the leading and trailing edges are either strictly convex (on the upper surface) or strictly concave (on the lower surface).

In this chapter, emphasis has been placed on a method for quantitatively estimating the average grain size of metals. In quality control, the requirements are often more qualitative. It should be clear, however, that this chapter has developed a foundation for implementing a variety of qualitative techniques. The key is to be able to relate measurements made in an image to the topography of the surface being viewed. Columnar grain can be detected by comparing grain size estimates using two sets of linear intercept procedures. One set would sample lines parallel to the leading and trailing edges. The other set would sample lines orthogonal to the leading and trailing edges. Any significant discrepancy would indicate the presence of columnar grain.

A more local version of the three circle (Abrams) procedure can be used to asign a grain size estimate to each point in an image. Demarcation lines between regions of different grain size would then appear as boundary lines in this "image" of local grain size values.

FOOTNOTE TO CHAPTER 5:

1. ASTM Designation: E112 - 74 is equivalent to American National Standard Z30.9 of the American National Standards Institute and has been approved by the Department of Defense to replace methods 311.1 and 312 of Federal Test Method Standard 151b and for listing in the DoD Index of Specifications and Standards.

6. EXPERIMENTS RELATING REFLECTANCE DATA AND OBJECT RELIEF

This chapter discusses the experimental determination of a reflectance map and its relation to object relief. The goal is to understand better how to determine the data required to apply the techniques developed in earlier chapters to practical situations. There is actually very little literature on the measurement of the surface photometric function $\phi(i,e,g)$ required for image analysis. The results presented here are meant to be illustrative, not conclusive.

6.1 SPECIFYING SURFACE REFLECTANCE

Two distinct physical processes are responsible for the reflection of radiant energy at boundary surfaces. The first of these is the mirror-like *specular reflection*. The second of these is the matte reflection which is believed to occur due to multiple reflections at the boundaries of small particles of which the surface is composed. This second process will be referred to as *diffuse reflection*. The *reflecting power* of a material is defined by:

$$R = \frac{I}{I_0}$$

where I_0 is the intensity of incident radiant energy and I is the intensity of energy reflected by the medium. At this point, there is some confusion over terminology. The convention is sometimes adopted that the reflecting power associated with a specular process is termed *reflectivity*, while the reflecting power associated with a diffuse process is termed *reflectance* <Wendlandt & Hecht 66>. Elsewhere, the term reflectance is used to cover both cases <Morgan 53>, <Jenkins & White 57>. Fortunately, in the determination of the reflectance map R(p,q), no fundamental distinction

need be made between specular and diffuse reflection. Here, the term reflectance will be used to cover both cases.

A complete knowledge of the reflectance properties of a particular sample involves the determination of both the spatial and spectral distribution of the reflected radiation with respect to both intensity and state of polarization. Reflectance measurements are an important tool in optics and analytic chemistry. The dependence of the reflecting power of optically smooth materials on wavelength, polarization and angle of incidence can be used to determine the fundamental optical constants of the material. Reflectance spectroscopy extends this analysis to materials with non smooth micro-structure. Such studies are useful for the analysis of powders of known particle size and shape ground from samples that can not be analyzed using traditional spectroscopic techniques, as well as for chemical constituent analysis of compound substances. Little of this work can be related directly to image analysis. Reflecting power considers only the fraction of the incident intensity reflected and not its spatial distribution. (One area of interest, however, is in the analytic modeling of reflectance based on models of surface micro-structure)

In order to make use of reflectance measurements in image analysis, it is necessary to explicitly account for the spatial distribution of the reflected energy. Let I_0 be the intensity of incident radiant energy as before. Consider a surface element of size ds. Let i, e and g be the three photometric angles defined in figure 2-2. The surface element ds reflects energy into the hemisphere defined by $e < \pi/2$. Let I_l be the intensity per unit solid angle per unit surface area perpendicular to the emitted ray of energy reflected by the surface element ds in the direction of the viewer. I_l is called the *luminance* of the (extended) surface

element ds and determines how bright it will appear when seen from view angle e. The surface photometric function $\phi(i,e,g)$ is defined by:

$$\phi(i,e,g) = \frac{I_i}{I_o} \qquad (6.1.1)$$

Note that (6.1.1) ignores the dependence of $\phi(i,e,g)$ on the wavelength of the incident illumination. Thus, to use the corresponding reflectance map R(p,q) in image analysis, it is necessary to measure $\phi(i,e,g)$ under the same illumination conditions that will obtain when objects are to be viewed. In addition, it is necessary to account for (possibly) differing sensitivities between the device used to measure $\phi(i,e,g)$ and the device used to take the image.

One method for determining the surface photometric function which avoids these problems is to measure the intensities recorded in an image of an object of known (convex) shape. The corresponding reflectance map R(p,q) will hold for all objects made from the same material and viewed using the same imaging device and under the same object surface, light source and viewer geometry.

Another method for determining the surface photometric function is to use a photo-goniometer to explicitly measure the dependence of reflectance on the three photometric angles i, e and g. Such measurements were carried out using a sample gray iron casting as the specimen material and are discussed in the section below.

6.2 MEASURING THE REFLECTANCE OF CAST GRAY IRON

First, in presenting the measurements, it is important to be clear on what the measurements are measurements of. Other definitions of the surface photometric function arise which differ from the one defined here by constant factors or by additional terms of cos(e) and/or cos(i). These distinctions can be made clear if one carefully analyzes the measurement situation.

Consider the experimental situation depicted in figure 6-1. Here, there is a distant source producing a narrow collimated beam of incident illumination. Suppose the incident light intensity is I_0 per unit area perpendicular to the incident beam. Suppose the cross-sectional area of the incident beam is dA. In this situation, the total luminous flux incident on the surface is independent of the angle of incidence and is simply equal to $I_0 dA$. Let the corresponding area of surface illuminated by the incident beam be ds. Then, ds varies with the angle of incidence and is given by:

$$ds = \frac{dA}{\cos(i)} \qquad (6.2.2)$$

Suppose that the receptive field of the distant detector is large compared to ds so that all of the incident flux reflected in the direction of the viewer is captured by the detector. Let F be the flux so measured by the detector and let I_l denote the intensity per unit solid angle per unit area perpendicular to the emitted beam as given in (6.2.1). Then the flux F is proportional to $I_l \cos(e) ds$ so that:

$$\phi(i,e,g) = \frac{I_l}{I_0} \propto \frac{F}{I_0 \cos(e) ds} \propto \frac{F \cos(i)}{\cos(e)} \qquad (6.2.3)$$

Thus, (6.2.3) relates measurements obtained in the experimental situation

depicted in figure 6-1 to the definition of the photometric function given by (6.2.1).

Compare this to the experimental situation depicted in figure 6-2. In this second situation, there is a distant source producing a collimated beam of incident illumination that is wide compared to the receptive field of the distant detector. Let I_0 and I_1 be given as before. Suppose the cross-sectional area of the receptive field of the detector is dR and let ds be the corresponding area of surface sampled by the detector. Now, $dR = \cos(e)ds$. Let F be the flux measured by the detector. Then,

$$\phi(i,e,g) = \frac{I_1}{I_0} \propto \frac{F}{I_0 \cos(e) ds} \propto F \qquad (6.2.4)$$

Thus, (6.2.4) relates measurements obtained in the experimental situation depicted in figure 6-2 directly to the definition of the photometric function given in (6.2.1). This is not surprising, since figure 6-2 correctly depicts what happens in an imaging situation. Each picture element (pixel) in an image does not sample a single point on the object surface. Rather, each pixel samples an (extended) element of surface ds. The intensity recorded at each pixel appears brighter due to the foreshortening effect produced by the view angle e.

The experimental situation under which the photo-goniometer measurements were made for cast gray iron corresponds to that depicted in figure 6-1. The particular goniometer geometry is diagrammed in figure 6-3. A LEITZ PRADO UNIVERSAL projector was used as the light source. An opaque slide containing a small pinhole was projected to produce a collimated beam of about 1 cm in diameter. A UNITED DETECTOR TECHNOLOGY, INC. 80X OPTO-METER (fitted with a tele-photometer) was used as the detector. It was set to measure flux (in watts). At a distance of about 2 m, the

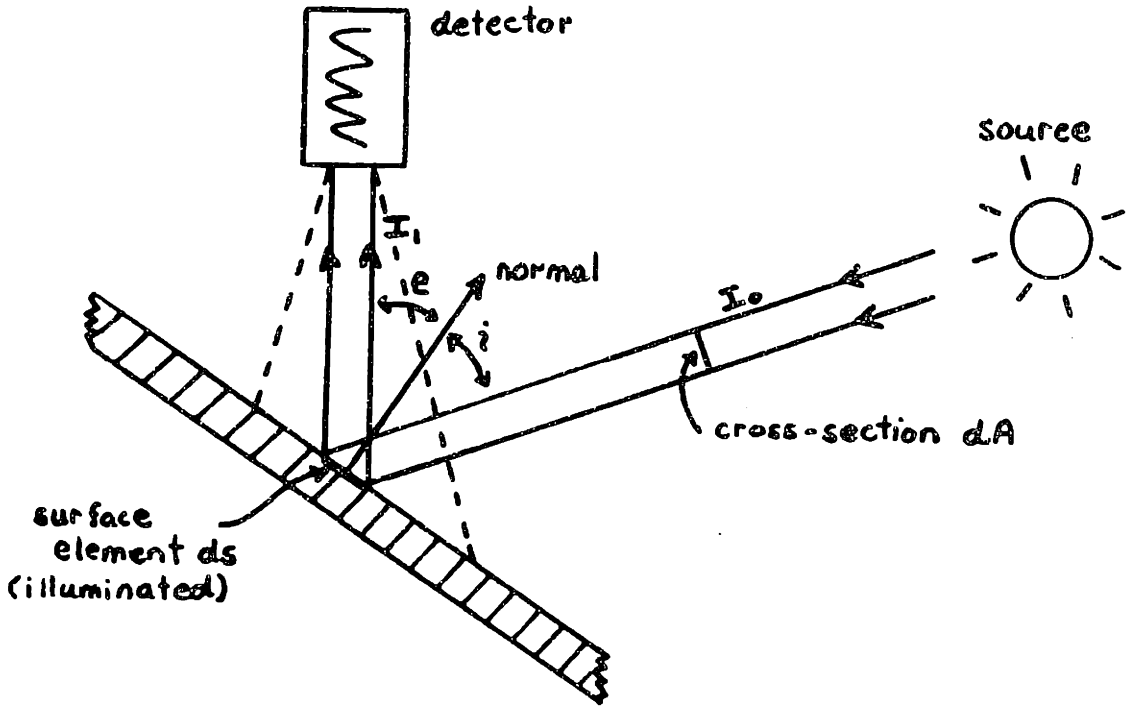

Figure 6-1 Measurement situation corresponding to a collimated beam of incident illumination which is narrow compared to the receptive field of the detector.

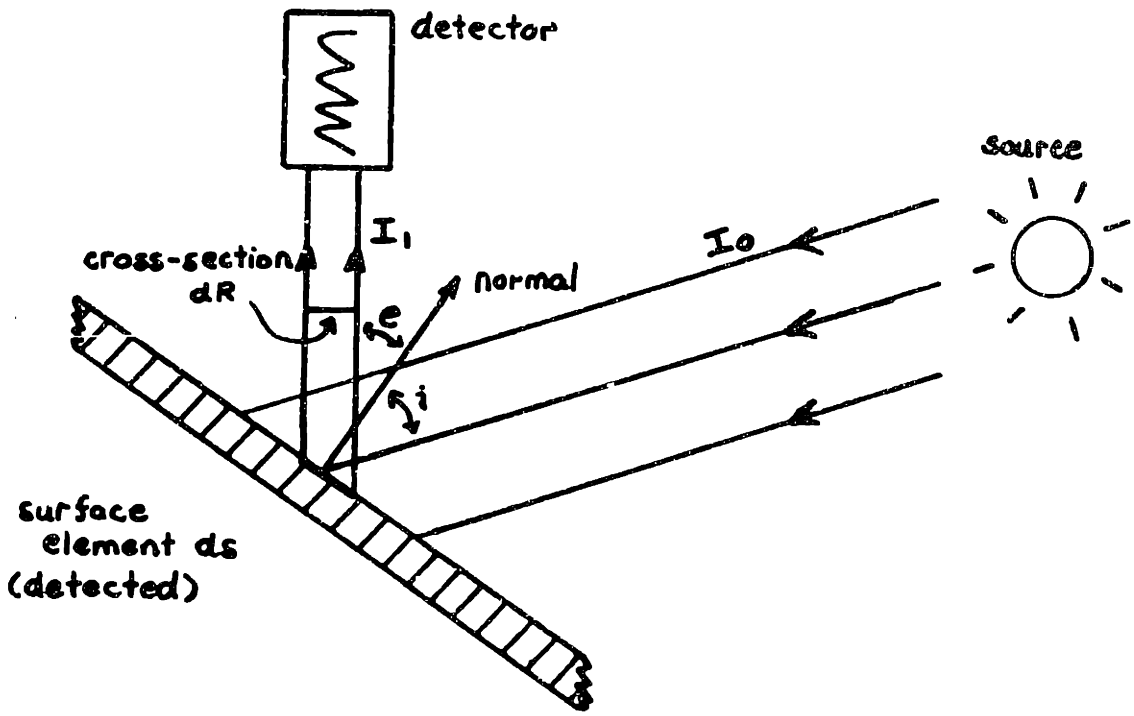

Figure 3-2 Measurement situation corresponding to a collimated beam of incident illumination which is wide compared to the receptive field of the detector.

receptive field of the tele-photometer subtended about 8 cm of sample surface. A small (planar) section of specimen material, about 3 cm by 8 cm, was mounted at the origin of the XYZ coordinate system as shown. The phase angle g is the angle between the light source and the tele-photometer. For the particular experiment, the phase angle g was held fixed. The view angle e and the angle of incidence i were varied by rotating the sample about the x-axis and y-axis.

Let θ_x be the angle first rotated about the x-axis. Let θ_y be the subsequent angle of rotation about the y-axis. Measurements were made in increments of 5° in both θ_x and θ_y subject only to the restriction that the assumptions underlying figure 6-1 continued to hold. From (6.2.2), one observes that, for a fixed dA, ds increases as cos(i) decreases. Thus, measurements were stopped when ds exceeded the receptive field of the detector, or, as was more often the case, when the (relatively small) sample no longer captured all of the incident flux.

To generate a reflectance map, the angles θ_x and θ_y must be related to gradient coordinates p and q. Two anomalies of the particular goniometer geometry must be dealt with. First, the positions of the source and viewer have been interchanged with respect to the standard imaging geometry used to define the reflectance map in Chapter: 2.3. The vector [0,0,-1] now points at the source while the vector [sin(g),0,-cos(g)] points at the viewer. Second, with the particular optical arrangement used, the x-axis and y-axis were coupled. That is, a rotation about one axis moved the other.

Now, if one first rotates θ_x about the x-axis and then rotates θ_y about the y-axis, it can be shown that the equivalent gradient coordinates describing the resultant surface orientation are given by:

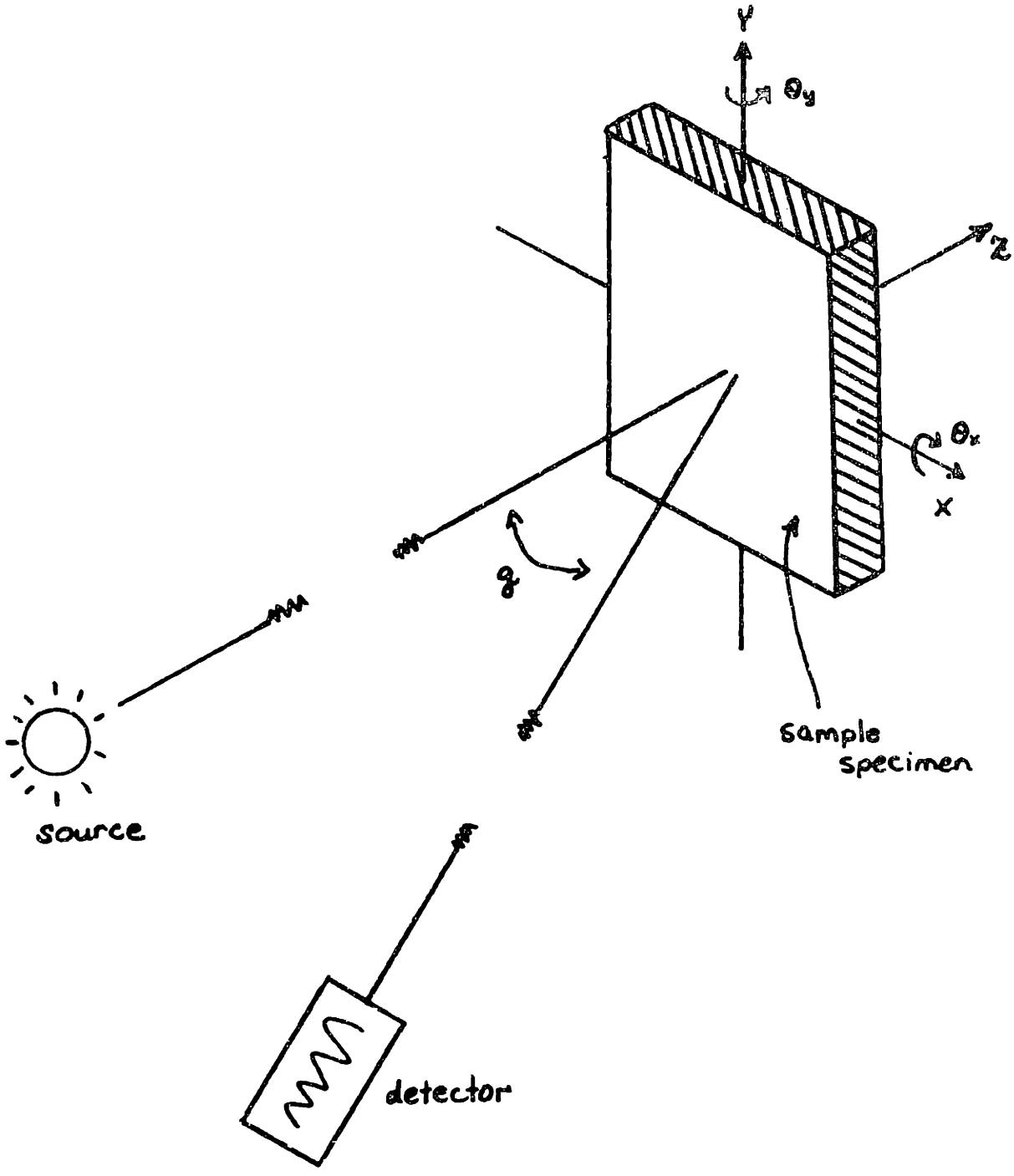

Figure 6-3 Photo-goniometer geometry.

$$p = \tan(\theta_y - g)$$

$$q = \frac{\tan(\theta_x)}{\cos(\theta_y - g)}$$

In this scheme, the position of the light source is given by:

$$p_s = -\tan(g)$$

$$q_s = 0$$

For the particular measurements to be reported, the phase angle g was fixed at $g = 35°$. The measurements were first multiplied by the "correction factor" cos(i)/cos(e) and then normalized so that the maximum reflectance value was 1.0. The results are presented as a contour plot. Figure 6-4 plots these contours (spaced 0.1 units apart). The box enclosing the contours delimits that portion of gradient space which was measured. Figure 6-5 plots contours of constant cos(i)/cos(e) (spaced 0.2 units apart).

One would expect reflection from the surface of a metal to be highly specular. Specular reflection from an optically smooth surface is easy to characterize. For such reflection, e = i and the incident, view and phase angles all lie in the same plane. Call this viewing direction the *perfect specular direction*. Note, however, that as surface roughness increases, materials with a high degree of specular reflection will nonetheless reflect light in directions away from the perfect specular direction. For any viewing direction e, one can determine the angle between e and the perfect specular direction. Call this angle the *off specularity angle s*. It can be shown that

$$\cos(s) = 2\cos(i)\cos(e) - \cos(g) \qquad (6.2.5)$$

Figure 6-6 plots contours of constant cos(s) for $p_s = -\tan(35°)$ $q_s = 0$ (spaced 0.1 units apart). Contours of constant cos(s) are circles in

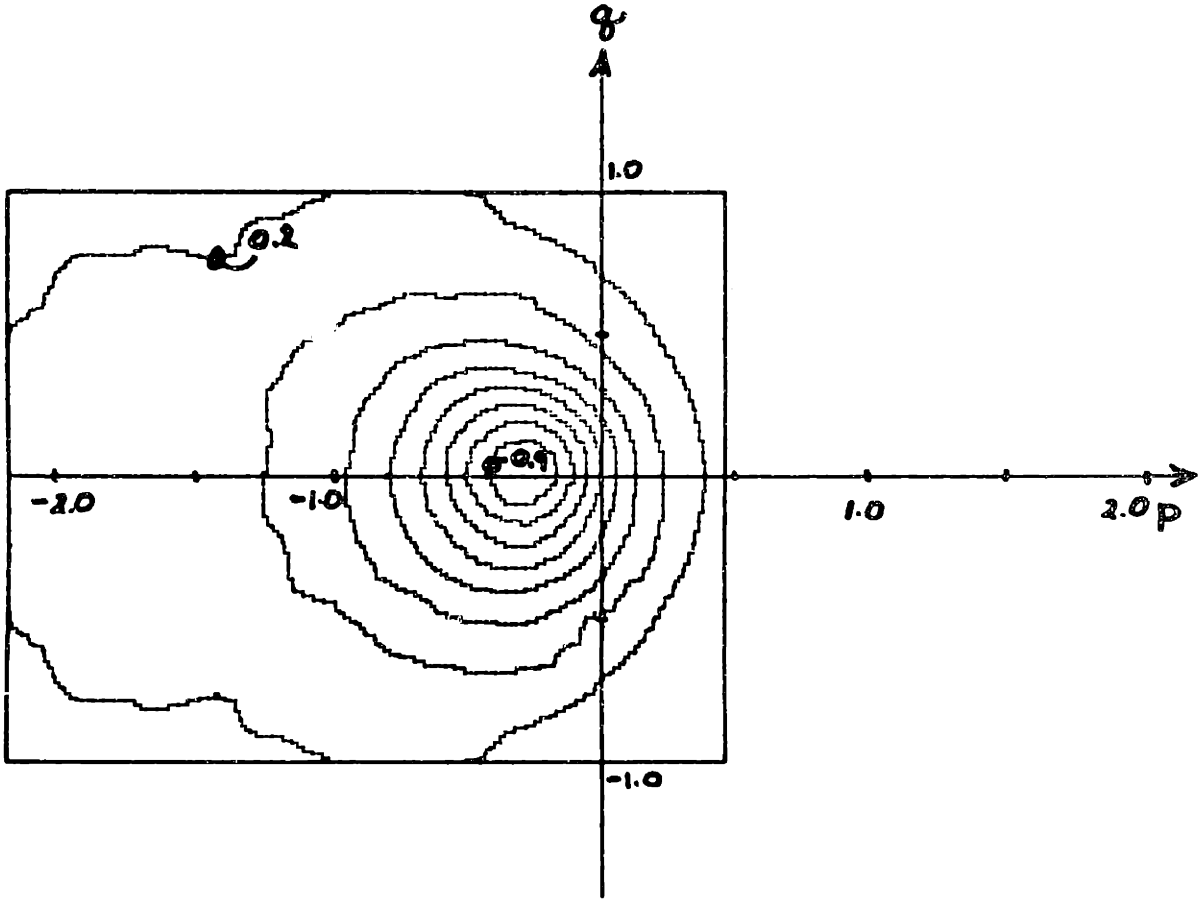

Figure 6-4 Measured reflectance map for cast gray iron with light source at $p_s = -0.7$ and $q_s = 0.0$ (contours are spaced 0.1 units apart). The solid box marks the region of gradient space over which measurements were made.

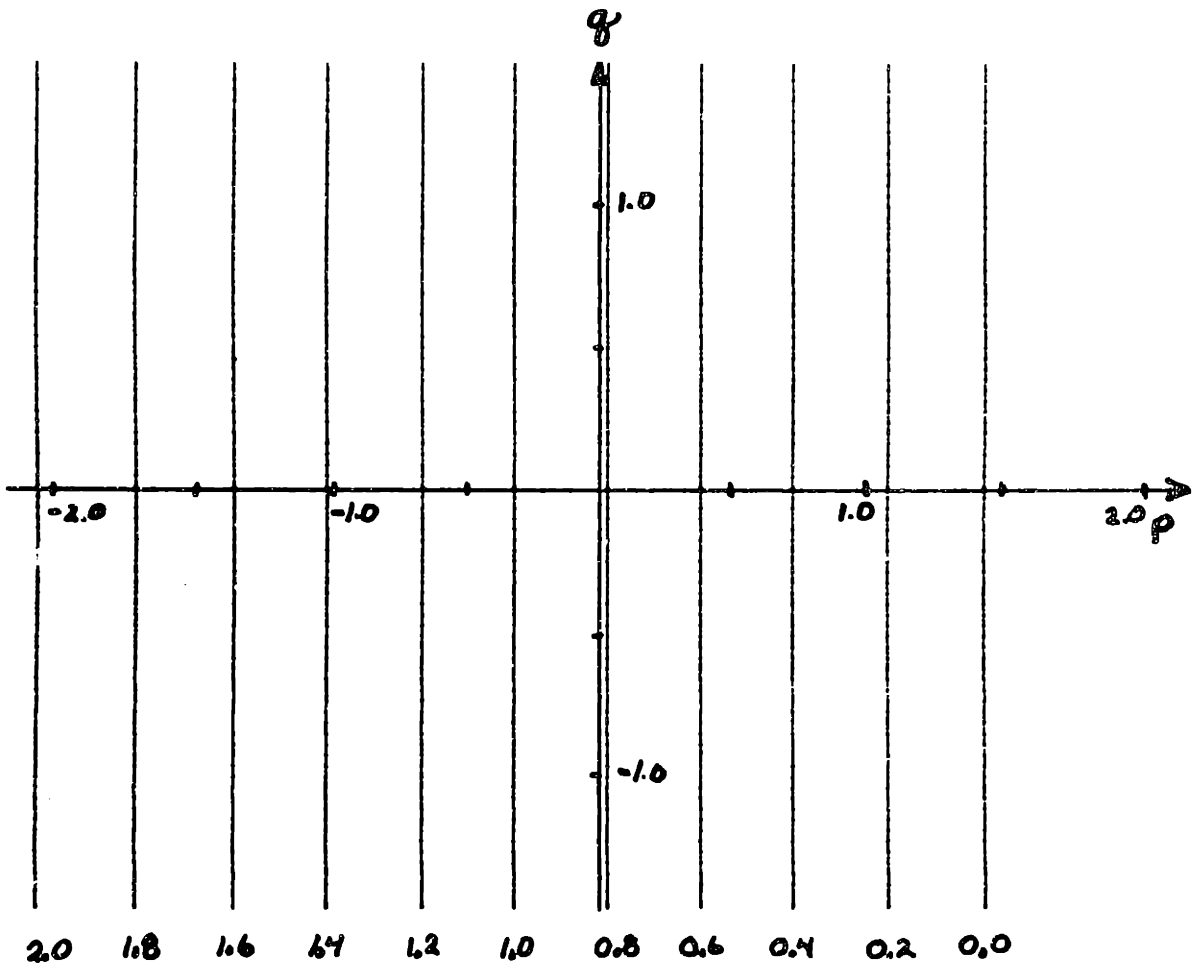

Figure 6-5 Contours of constant cos(i)/cos(e) for light source at p_s = -0.7 and q_s = 0.0 (contours are spaced 0.2 units apart).

gradient space. In general, if the light source is positioned at (p_s, q_s), then the contour $\cos(s) = k \geq 0$ is a circle in gradient space centered at (cp_s, cq_s) and of radius r where:

$$c = \frac{\cos(g)}{k + \cos(g)}$$

and

$$r^2 = \frac{1 - k^2}{[k + \cos(g)]^2}$$

For most surfaces, measurements suggest that both specular and diffuse reflection is always present, the relative proportion of each depending on the nature of the material <Wendlandt & Hecht 66>. By combining a term in cos(s), to account for the specular component, and a term in cos(i), to account for the diffuse component, it is possible to model different surface materials. A good approximation to many materials is achieved by letting the surface photometric function be:

$$\phi(i,e,g) \propto t^{\frac{(n+1)}{2}}\cos(s)^n + (1-t)\cos(i) \qquad (6.2.6)$$

where t lies between 0 and 1 and determines the fraction of incident light reflected specularly, a parameter which models the optical properties of the material, and n determines the sharpness of the specular peak, a parameter which models the surface micro-structure (from <Horn 77a>). Figure 6-7 plots the reflectance map obtained using (6.2.6) with $p_s = -0.7$, $q_s = 0$, $n = 3$ and $t = 0.6$. There is good qualitative agreement between figure 6-7 and the data shown in figure 6-4. Note, however, that this agreement has been verified for only one phase angle and over a limited region of gradient space.

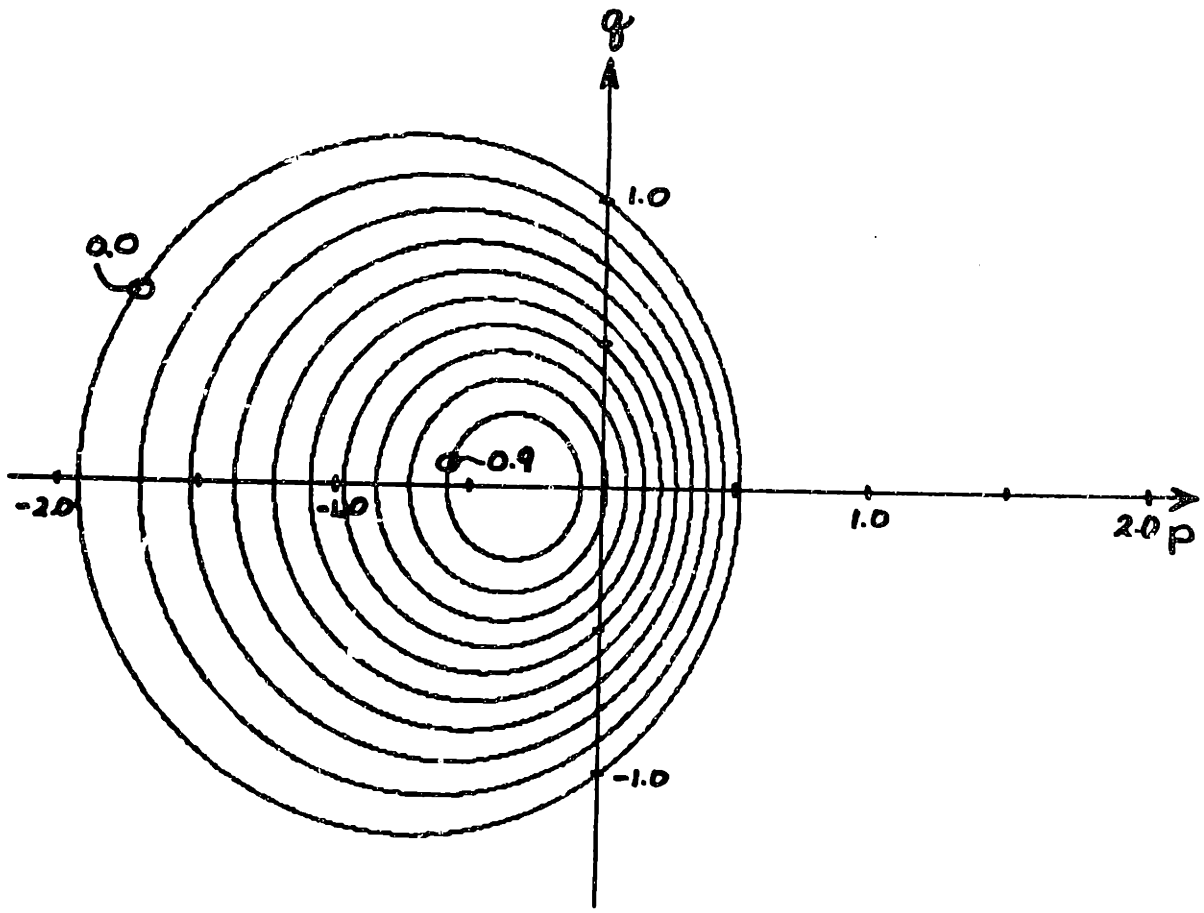

Figure 6-6 Contours of constant cos(s) for light source at p_s = -0.7 and q_s = 0.0 (contours are spaced 0.1 units apart).

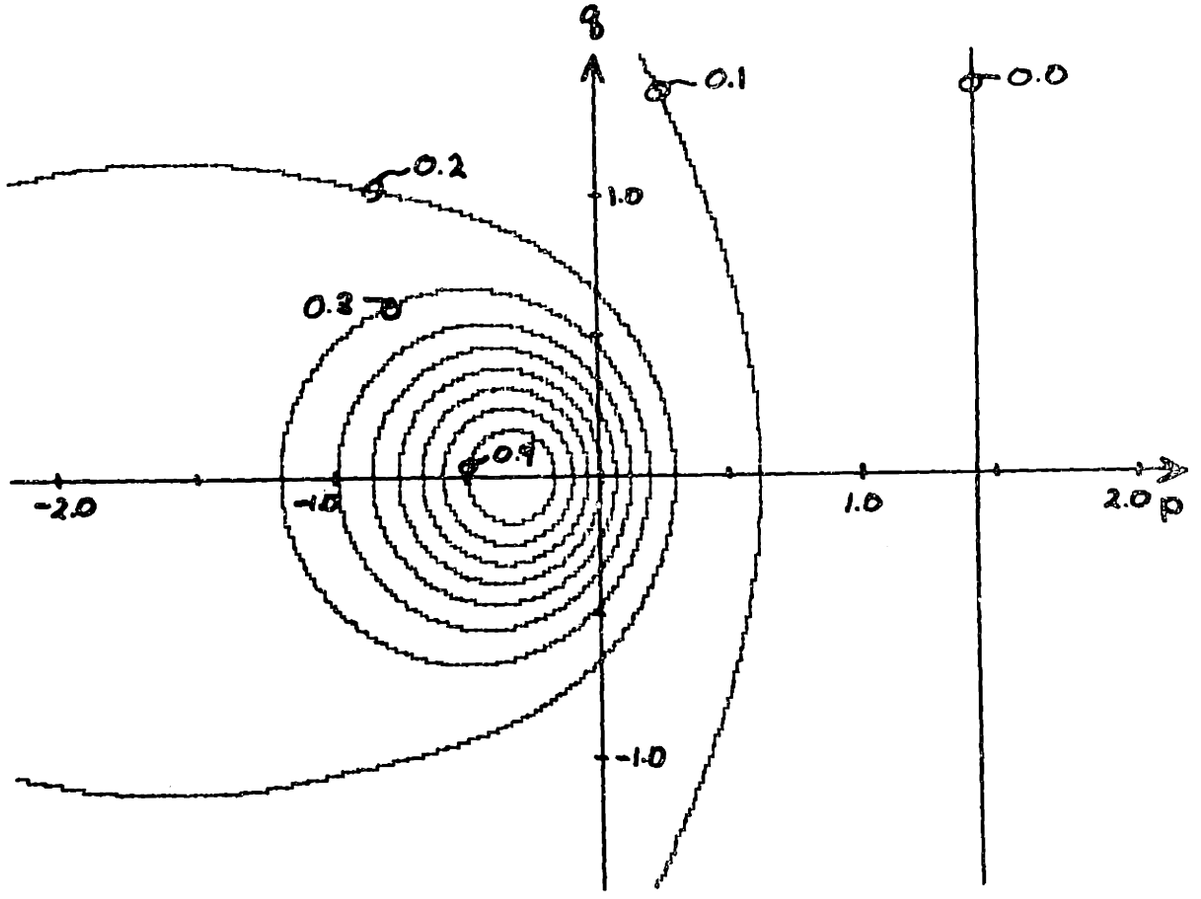

Figure 6-7 Phenomenological model of reflectance map for gray cast iron with light source at p_s = -0.7 and q_s = 0.0 (contours are spaced 0.1 units apart).

It is important to point out that (6.2.6) is a phenomenological model and is not based on any optical theory or actual photometric measurements. Where such measurements have been made, there are some additional points to note. The analytic model developed to predict the pattern of sunlight (or moonlight) glitter on a wind-ruffled sea surface <Plass *et al* 77> notes a "shift to the horizon" of the bright spot as a function of wind speed. The data presented in figure 6-4 has its maximum bright spot centered about the surface normal oriented 15.1° from the viewer. (6.2.6), on the other hand, predicts that the bright spot should be centered about the surface normal oriented 17.5° from the viewer. Thus, here a "shift to the viewer" of 2.4° is observed.

The point here is not to produce closed form expressions for the surface photometric function of gray iron. At best, such an expression would vary with alloy composition and sand grain size. Rather, the point has been to demonstrate that a reflectance map for a particular alloy with a particular surface-microstructure can be determined empirically and is, at least, consistent with phenomenological models of reflectance already in existence.

6.3 OBTAINING RELIEF DATA

An effort was also made to determine object relief directly for the shuttle eye discussed in Chapter: 4.2. To do this, a crude coordinate gauging program was written using a force sensing mechanical manipulator <Silver 73>. A needle probe was inserted between the manipulator grippers and the surface scanned at a resolution of 0.01 inches in x and y. At each (x,y) point, the manipulator was programmed to descend until it "touched" the surface. The height of each touch was recorded to create a terrain

file. Figure 6-8 plots, from four different orientations, the terrain data obtained for the shuttle eye. Figure 6-9 is an image of the shuttle eye synthesized from the terrain data and the reflectance map determined above.

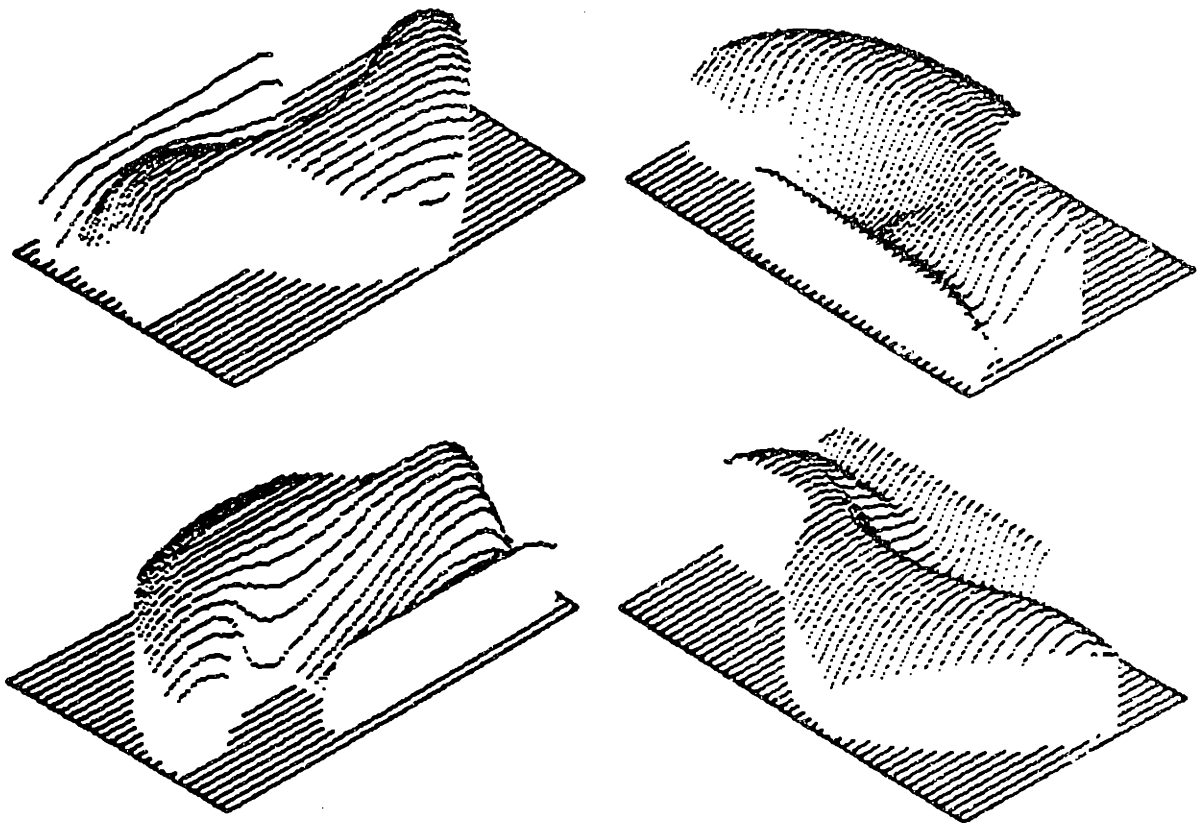

Figure 6-8 Plot of measured terrain data for shuttle eye (from four views).

Figure 6-9 Synthesized image of shuttle eye using measured terrain data and phenomenological model of reflectance map with light source at $p_s = 0$ and $q_s = 0$.

7. CONCLUDING REMARKS

This chapter summarizes the thesis in terms of the goals initially set forth and the results achieved. The thesis had two initial goals: one theoretical and one practical. The theoretical goal was to understand how to interpret image intensity in terms of the underlying surface topography of the objects being imaged. The practical goal was to explore how machine vision systems could be applied to the problem of inspecting surface defects in metal castings.

With these two goals in mind, the thesis naturally split into two parts. The first part of the thesis consisted of a basic investigation into the problem of determining object relief directly from image intensity. The nature of this computation is of fundamental importance to image analysis. Image analysis is a hard problem unless properties of image intensity can be related to properties of the objects being imaged. The work of <Horn 75> and <Horn 77a> provided the initial formulation for determining object relief from intensity. The key observation is that, in a mathematical sense, the problem of determining object relief locally at each image point is underdetermined. Thus, in order to achieve a global interpretation, it necessary to invoke additional assumptions about the nature of the object surface in view.

This present work extends the work of Horn by providing a convenient mechanism for expressing assumptions about the curvature of the object surface (relative to the viewer) and by demonstrating how such assumptions can be exploited as geometric constraints in methods for computing object relief from intensity. The image Hessian matrix H captures the notion of object curvature and assumptions about object curvature map intuitively into properties of H.

In its theoretical contribution, the thesis is evolutionary rather than revolutionary. Dealing with arbitrary doubly curved surfaces remains a difficult problem. In general, there is no unique surface $z = f(x,y)$ for an image $I(x,y)$ even if the reflectance map $R(p,q)$ is known. One unexplored idea is to try and compute that surface interpretation which requires the least amount of surface curvature to account for the observed change in intensity.

Yet, many situations have been demonstrated in which the image analysis problem simplifies greatly. Surfaces which are singly curved or which are solids of revolution (i.e., have a circular cross-section) are particularly easy to deal with. Such simplifications dominate manufactured parts since there are few fabrication methods for producing doubly curved surfaces. (But, alas, casting is one!). Such simplifications also seem to dominate the interpretation humans will assign to underdetermined images. <Marr 76a> points out how the assumption that the boundary curve of an image silhouette is the projection of a planar curve in space leads to the interpretation that the object is a generalized cone.

It is also worthwhile to point out that the design of curved surfaces has always presented difficulties to the engineer. Some types of curved shapes, such as cylinders, spheres, surfaces of revolution and singly curved surfaces can be represented or indicated on a two-dimensional drawing with considerable precision. Wherever possible the engineer constrains curved portions of his design to one of these types. There are few accepted drafting techniques for generating curves in a drawing which are not planar in space. (Attempts at such renderings are generally difficult for humans to interpret.)

The second part of the thesis consisted of a practical demonstration of a working inspection system. Having discussed the needs of casting inspection with various representatives of the castings industry, a particular inspection problem was chosen. An industry standard for estimating the average grain size of metals was obtained and existing ideas in machine vision <Marr 76b>, <Lozano-Perez 77> were specialized to the particular problem of verifying grain structure for equiaxed turbine blades and vanes. The motivation for this second part of the work was simply to demonstrate that current ideas and technology could be applied to an existing inspection problem. Such a demonstration was illustrated in Chapter: 5.

It soon became obvious, however, that in order to build flexible casting inspection systems, it is necessary to interpret features of intensity in terms of the underlying three-dimensional geometry of the part being inspected. Simple-minded inspection schemes that ignore this fact will fail.

One might propose to do visual inspection of metal castings by comparing the image of each sample casting against the image of a casting known to be free of defects. This would require a standardized method of part presentation. Suppose, for the sake of argument, that this is an acceptable constraint. A least-squares measure of the difference in image intensities would be a possible inspection criterion. Parts whose intensities match to within a specified tolerance would be accepted while those outside the specified tolerance would be rejected.

This method of inspection can be likened to a method of inspection that is actually used in many foundries. Castings can be weighed very cheaply. If the casting does not weigh as much as it should, then there

are likely shrinkage voids or regions of high porosity (i.e., holes) inside the casting. This is a convenient way to find obvious internal defects without incurring the high cost associated with a more quantitative radiographic or ultra-sonic inspection. This method does not discriminate the nature or position of the defect within the casting but it is successful to the extent that there is a simple linear relationship between the weight measured and the amount of metal missing from the part.

Unfortunately, in comparing intensities, there is no such simple relationship between measured differences in intensity and features of part geometry. Features of topography map into intensity according to the local object surface, light source and viewer geometry. This mapping is one to many (i.e., a particular feature of topography maps into many features of intensity depending on the position of the light source and the view angle). Simple detection methods will fail unless the features detected can be interpreted in the context of the part as a whole. A good example of this fact occurred in the method for grain size estimation presented in Chapter: 5. Any measurement of grain size from a two-dimensional image is meaningless unless that measurement can be related to surface curvature (relative to the viewer).

There are two strategies one might adopt to overcome this problem. A first strategy would be to incorporate models of all the parts being inspected and attempt to relate intensity to part geometry by matching images to these models. This strategy has been explored elsewhere <Perkins 77>. A second strategy would be to attempt to determine topography directly from the intensity values recorded in the image.

The first part of this thesis develops the theory for applying this second strategy. The two properties of a casting which determine its surface photometry, namely alloy composition and surface micro-structure, are carefully controlled in a casting process. The light source and viewer geometry can be standardized in any inspection station.

Many typical surface defects in castings (eg. pinholes, cold shuts, cracks and hot tears) manifest themselves as properties of surface topography that could not have been the result of an intended casting operation. To do the kind of first visual inspection required in a typical batch-oriented foundry, it is not necessary to have a precise model of the part geometry. Consider the problem of finding cold shut defects in a green sand mold foundry. A possible inspection system would use course resolution photometric stereo to determine the approximate shape of the casting and then look for variations in intensity at the (concave) boundaries between large sections of the casting which would indicate a lapping or layering of the surface. The viewer-centered representation of object relief discussed in Chapter: 2.1 seems to be the right level of description for this kind of casting inspection.

REFERENCES

Agin, G. J. and Binford, T. O. (1973), "Computer Description of Curved Objects", in *Proceedings of the 3rd International Joint Conference on Artificial Intelligence*, pp 629-640, August 1973.

ASM (1970), *Metals Handbook (8th Edition), Vol. 6, Forging and Casting*, American Society for Metals, Metals Park, Ohio, 1970.

ASTM (1976), ASTM Designation: E 112-74, "Standard Methods for Estimating the Average Grain Size of Metals", in *1976 Annual Book of ASTM Standards*, Part 11, pp 208-240, American Society for Testing and Materials, 1976.

Beck, J. (1974), *Surface Color Perception*, Cornell University Press, 1974.

Binford, T. O. and Horn, B. K. P. (1973), "The Binford-Horn Line Finder", AI MEMO 285, AI Laboratory, M.I.T., December 1973.

Caulfield, H. J. (1976), "Three Dimensional Range Finding", *International Optical Computing Conference*, Digest of Papers, pp 78-79, IEEE Catalog No. 76CH1100-7C, August 31-September 2, 1976.

Draper (1973), "Annual Progress Report No. 2 for the Development of Multi-Moded Remote Manipulator Systems (Period Ending January 1973)", C. S. Draper Laboratory, M.I.T., March 1973.

Ejiri, M., Uno, T., Mese, M., and Ikeda, S. (1973), "A Process for Detecting Defects in Complicated Patterns", *Computer Graphics and Image Processing*, Vol 2, No. 3/4, pp 326-329, December 1973.

Freuder, E. C. (1976), "A Computer System for Visual Recognition Using Active Knowledge", AI TR 345, AI Laboratory, M.I.T., June 1976.

Guzman, A. (1968), "Computer Recognition of Three-Dimensional Objects in a Visual Scene", MAC TR-59 (Thesis), Project MAC, M.I.T., December 1968.

Horn, B. K. P. (1968), "Focussing", AI-MEMO 160, AI Laboratory, M.I.T., May 1968.

Horn, B. K. P. (1975), "Obtaining Shape from Shading Information", in *The Psychology of Computer Vision*, P. H. Winston (ed.), McGraw-Hill, pp 115-155, 1975.

Horn, B. K. P. (1977a), "Understanding Image Intensities", in *Artificial Intelligence*, Vol 8, pp 201-231, 1977.

Horn, B. K. P. (1977b), "Using Synthetic Images to Register Real Images with Surface Models", AI-MEMO 437, AI Laboratory, M.I.T., August 1977.

Huffman, D. A. (1971), "Impossible Objects as Nonsense Sentences", in *Machine Intelligence 6*, R. Meltzer and D. Michie (ed.), Edinburgh University Press, pp 295-323, 1971.

Huffman, David A. (1975), "Curvature and Creases: A Primer on Paper", *Proceedings of Conference on Computer Graphics, Pattern Recognition and Data Structures*, pp 360-370, May 1975.

Jenkins, F. A. and White, H. E. (1957), *Fundamentals of Optics*, (3rd edition), McGraw-Hill, 1957.

Johnston, A. R. (1973), "Infrared Laser Rangefinder", Report NPO-13460, Jet Propulsion Laboratory, Pasadena, California, August 1973.

Kepr, B. (1969), "Differential Geometry", in *Survey of Applicable Mathematics*, K. Rektorys (ed.), The M.I.T. Press, pp 298-373, 1969.

Lozano-Perez, T. (1977), "Parsing Intensity Profiles", *Computer Graphics and Image Processing*, Vol 6, No. 1, February 1977.

Luenberger, D. G. (1973), *Introduction to Linear and Nonlinear Programming*, Addison-Wesley, 1973.

Mackworth, A. K. (1973), "Interpreting Pictures of Polyhedral Scenes", in *Artificial Intelligence*, Vol 4, pp 121-137, 1973.

Mangasarian, O. L. (1969), *Nonlinear Programming*, McGraw-Hill, 1969.

Marr, D. (1976a) "Analysis of Occluding Contour", AI-MEMO 372, AI Laboratory, M.I.T., October 1976.

Marr, D. (1976b), "Early Processing of Visual Information", *Philosophical Transactions of the Royal Society of Britain 275*, pp 483-524, 1976.

Marr, D. (1977) "Representing Visual Information", AI-MEMO 415, AI Laboratory, M.I.T., May 1977.

Marr, D. and Poggio, T. (1976), "Cooperative Computation of Stereo Disparity", in *Science 194*, pp 283-287.

Moore, J. T. (1968), *Elements of Linear Algebra and Matrix Theory*, McGraw-Hill, 1968.

Morgan, J. (1953), *Introduction to Geometrical and Physical Optics*, McGraw-Hill, 1953.

Nevatia, R. & Binford, T. O. (1973), "Structured Descriptions of Complex Objects", in *Proceedings of the 3rd International Joint Conference on Artificial Intelligence*, pp 641-645, August 1973.

Nitzan, D., Brain, A. E. & Duda, R. O. (1977), "The Measurement and Use of Registered Reflectance and Range Data in Scene Analysis", *Proc. IEEE*, pp 206-220, Feb. 1977.

Perkins, W. A. (1977), "Model-Based Vision System for Scenes Containing Multiple Parts", in *Proceedings of IJCAI-77*, pp 678-684, August 1977.

Phong, B. T. (1975), "Illumination for Computer Generated Pictures", *CACM*, 18 pp 311-317, 1975.

Plass, G. N., Kattawar, G. W. and Guinn Jr., J. A. (1977), "Isophotes of Sunlight Glitter on a Wind-Ruffled Sea", *Applied Optics*, pp 643-653, March 1977.

Rindfleisch, T. (1966), "Photometric Method for Lunar Topography", *Photogrammetric Engineering*, pp 262-276, March 1966.

Roberts, L. G. (1965), "Machine Perception of Three-Dimensional Solids", in *Optical and Electro-optical Information Processing*, J. T. Tippett et al (ed.), M.I.T. Press, pp 159-197, 1965.

Rosenfeld, A., Hummel, R. A. and Zucker. S. W. (1976), "Scene Labelling by Relaxation Operations", *IEEE Transactions on Systems, Man and Cybernetics, SMC-6*, pp 420-433.

Shirai, Y. (1975), "Analyzing Intensity Arrays Using Knowledge About Scenes", in *The Psychology of Computer Vision*, P. H. Winston (ed.), McGraw-Hill, pp 93-113, 1975.

Silver, D. (1973), "The Little Robot System", AI MEMO 273, AI Laboratory, M.I.T., January 1973.

Sullivan, C. P. (1976), "Unidirectionally Solidified Superalloy Airfoils", *Foundry M&T*, pp 118-121, Jan. 1976.

van Diggelen, J. (1951), "A Photometric Investigation of the Slopes and the Heights of the Ranges of Hills in the Maria of the Moon", *Bulletin of the Astronomical Institutes of the Netherlands*, Vol. XI, No. 423, July 1951.

Wendlandt, W. W. and Hecht, H. G. (1966), *Reflectance Spectroscopy*, Interscience Publishers, John Wiley & Sons, 1966.

Waltz, D. (1975), "Understanding Line Drawings of Scenes with Shadows", in *The Psychology of Computer Vision*, P. H. Winston (ed.), McGraw-Hill, pp 19-91, 1975.

Will, P. M. and Pennington, K. S. (1971), "Grid Coding: A Preprocessing Technique for Robot and Machine Vision", *Advance Papers of the 2nd International Joint Conference on Artificial Intelligence*, pp 66-70, Spetember 1971.

Winston, P. H. (1972), "The M.I.T. Robot", in *Machine Intelligence 7*, Edinburgh University Press, 1972.

Winston, P. H. (1975), "Learning Structural Descriptions From Examples", in *The Psychology of Computer Vision*, P. H. Winston (ed.), McGraw-Hill, pp 157-209, 1975.

Young, I. T. (1969), "Automated Leukocyte Recognition", PhD Thesis, M.I.T., 1969.

APPENDIX A: MATHEMATICAL DETAILS

The purpose of this appendix is to explore more formally the question of how physical constraints on the object surface $z = f(x,y)$ map into geometric constraints on possible solutions to the basic equation $I(x,y) = R(p,q)$. Intuitive reasoning about smooth surfaces and gradient space needs to be augmented by some formal definitions and theorems. The mathematics presented in this appendix is not new. The pertinent definitions and theorems arise from work in linear algebra, convex analysis, differential geometry and nonlinear programming. The primary goal is to examine how this mathematics can be applied to the problem of interpreting image intensities. Thus, the required formal results are merely summarized. Technical details of proofs have been omitted. For those details, the reader is referred to <Mangasarian 69>, <Moore 68>, <Luenberger 73> and <Kepr 69>.

In order to develop the required theorems, the notion of surface smoothness must be made precise.

> **Definition.** Let $f(x)$ be a real-valued function defined on an open set $\Gamma \subset \mathbb{R}^n$. Then the (hyper)surface described by the equation $z = f(x)$ is *smooth over* Γ if $f(x)$ is twice differentiable with continuous second partial derivatives at every $x \in \Gamma$.

It will also be important to deal explicitly with surface curvature. The Hessian matrix H is the generalization to $\mathbb{R}^n$ of the concept of the curvature of a function of a real variable.

> **Definition.** Let $f(x)$ be a real-valued function defined on an open set $\Gamma \subset \mathbb{R}^n$ and let $x^* \in \Gamma$. Then, the $n \times n$ matrix $H = \nabla^2 f(x^*)$, whose ij^{th} element is given by:

$$[\nabla^2 f(x^*)]_{ij} = \frac{\partial^2 f(x^*)}{\partial x_i \partial x_j}$$

is called the *Hessian (matrix) of* $f(x)$ *at* x^*.

This first theorem establishes the symmetry of the Hessian matrix for smooth surfaces.

Theorem A.1 Let $f(x)$ be a real-valued function defined on an open set $\Gamma \subset \mathbb{R}^n$ and let $x^* \in \Gamma$. If the (hyper)surface described by the equation $z = f(x)$ is smooth at x^*, then

$$\frac{\partial}{\partial x_i}\frac{\partial f(x^*)}{\partial x_j} = \frac{\partial}{\partial x_j}\frac{\partial f(x^*)}{\partial x_i}$$

Corollary A.1 If $z = f(x)$ is smooth at x^*, then the Hessian matrix H exists at x^* and is symmetric.

It will now be shown how the Hessian matrix H underlies the model of the image forming process. Once again, recall that the assumptions used are that the viewer is distant, that the image projection is orthographic taking object point (x,y,z) onto image point (x,y) and that each image point receives the same incident illumination. The basic image forming equation $I(x,y) = R(p,q)$ is one equation in the two unknowns p and q. By taking partial derivatives of this equation with respect to X and Y, two equations are obtained:

$$I_x = p_x R_p + q_x R_q$$

$$I_y = p_y R_p + q_y R_q$$

(subscripts are used to denote partial differentiation). Theorem A.1 says that, for a smooth surface, $p_y = q_x$. Thus, two equations are obtained in the three unknowns p_x, q_x and $p_y = q_x$ where:

$$p_x = \frac{\partial^2 f(x,y)}{\partial x^2} \qquad q_y = \frac{\partial^2 f(x,y)}{\partial y^2} \qquad p_y = q_x = \frac{\partial^2 f(x,y)}{\partial x \partial y}$$

Thus, if these two equations are written as the single matrix equation:

$$\begin{bmatrix} I_x \\ I_y \end{bmatrix} = \begin{bmatrix} p_x & q_x \\ p_y & q_y \end{bmatrix} \begin{bmatrix} R_p \\ R_q \end{bmatrix}$$

then the relationship between the vector of first partial derivatives of the intensity function $[I_x, I_y]$ and the corresponding vector of first partial derivatives of the reflectance map function $[R_p, R_q]$ is given by:

$$[I_x, I_y]^T = H\,[R_p, R_q]^T \qquad (A.1)$$

where $H = \nabla^2 f(x,y)$ is the Hessian matrix of second partial derivatives of the object surface $z = f(x,y)$.

First-order (approximate) equations, in terms of differentials, relating a small movement in the image to the corresponding movement in gradient space are given by:

$$dp = p_x\,dx + p_y\,dy$$

$$dq = q_x\,dx + q_y\,dy$$

Again, these two equations are written as the single matrix equation:

$$\begin{bmatrix} dp \\ dq \end{bmatrix} = \begin{bmatrix} p_x & p_y \\ q_x & q_y \end{bmatrix} \begin{bmatrix} dx \\ dy \end{bmatrix}$$

Thus, to a first-order approximation, the relationship between a small movement [dx,dy] in the image and the corresponding movement [dp,dq] in gradient space is also determined by the Hessian matrix H. It is given by the equation:

$$[dp,dq]^T = H\,[dx,dy]^T \qquad (A.2)$$

A few words of caution are in order. While equation (A.1) above is exact at any image point (x,y) and its corresponding gradient point (p,q), equation (A.2) is only approximate. The Hessian matrix H varies with x

and y. In the subsequent analysis, however, the standard assumption of nonlinear programming is adopted. It is assumed that, for a smooth surface $z = f(x,y)$, third and higher order derivatives can be ignored (locally). It is assumed that $[dx,dy]$ can be chosen small enough so that H can be considered constant over the interval (x,y) to $(x+dx,y+dy)$.

Suppose image point (x,y) is known to correspond to gradient point (p,q). If two linearly independent directions $[dx_1,dy_1]$ and $[dx_2,dy_2]$ and the corresponding $[dp_1,dq_1]$ and $[dp_2,dq_2]$ are known, then the Hessian matrix H is determined uniquely at (x,y). Indeed,

$$H = \begin{bmatrix} dp_1 & dp_2 \\ dq_1 & dq_2 \end{bmatrix} \begin{bmatrix} dx_1 & dx_2 \\ dy_1 & dy_2 \end{bmatrix}^{-1}$$

A.1 HORN'S METHOD FOR OBTAINING SHAPE FROM SHADING INFORMATION

It is now appropriate to look at the method Horn developed for obtaining shape from shading information <Horn 75>, <Horn 77a>. The goal in this section is to interpret Horn's method in the context of the current development. This will lead to a better understanding of the problem of determining relief from intensity and will help to motivate the remaining sections of this appendix.

The basic recipe for Horn's solution is as follows:

(i) Suppose image point (x,y) is known to correspond to a point (p,q) in gradient space. Then, the change in $z = f(x,y)$ corresponding to a small movement $[dx,dy]$ in the image is given by the first-order approximation:

$$dz = pdx + qdy$$

(ii) The new gradient point corresponding to the image point (x+dx,y+dy) is obtained by updating the current gradient (p,q) according to the equation:

$$[dp,dq]^T = H\,[dx,dy]^T$$

By starting at some known point and iterating the above two operations, a path in the image is traced out for which the corresponding gradients and hence the corresponding relief profile can be determined. Unfortunately, there is not enough information to determine the matrix H. The only constraint on H is that it satisfies the equation:

$$[I_x,I_y]^T = H\,[R_p,R_q]^T$$

Note, however, that matrix multiplication is a linear operation. If [dx,dy] is chosen to be in the direction of $[R_p,R_q]$ then linearity is sufficient to guarantee that [dp,dq] will be in the direction of $[I_x,I_y]$. More precisely:

$$\text{If } [dx,dy] = [R_p,R_q]ds, \text{ then } [dp,dq] = [I_x,I_y]ds$$

Thus, by starting at some known point and iterating these two operations, a path in the image is traced out for which the corresponding gradients, and hence the corresponding relief profile on the object surface, can be determined. The catch is that an arbitrary direction for [dx,dy] can not be chosen. [dx,dy] must be chosen in the direction $[R_p,R_q]$. Horn has called the curves traced out on the surface in this fashion *characteristics* and their projection in the image plane *base characteristics*.

This result can be interpreted geometrically. Choosing [dx,dy] to be in the direction $[R_p,R_q]$ means that a base characteristic is traced out that is always perpendicular to the reflectance map contour for the current (p,q). Similarly, the fact that the resulting [dp,dq] is in the direction

$[I_x, I_y]$ means that the corresponding path traced out in gradient space is always perpendicular to the image intensity contour for the current (x,y). Figure A-1 illustrates this result.

In general, the path the base characteristic will trace out can not be controlled. It will depend on the particular object being viewed. For the remainder of this appendix, the requirement that [dx,dy] be choosen in such a way that the corresponding [dp,dq] can be determined exactly will be relaxed. The reason for this is not just to make the problem more difficult! Rather, the goal is to try and gain more control over the "path" that can be analyzed, independent of the object being viewed. To do this, the analysis of how properties of the object surface $z = f(x,y)$ relate to properties of the image Hessian matrix H is extended.

A.2 THE IMAGE HESSIAN MATRIX

In this section, the requirement that [dx,dy] be chosen in a particular direction is relaxed. Instead, this section examines how properties of the object surface $z = f(x,y)$ map into properties of H and, in turn, how these properties of H constrain the set of [dp,dq]'s that can correspond to a particular [dx,dy]. This analysis underlies the ability to hypothesize monotonicity relations between sets of (closely spaced) image points $I_1, I_2, \ldots, I_n$.

If H were known then the problem would be solved since Horn's method could be used to trace out an arbitrary base characteristic, independent of the object being viewed. On the other hand, if constraints on the object surface $z = f(x,y)$ can be expressed in terms of properties of H, then these constraints can be applied to the set of possible solutions to the basic equation $I(x,y) = R(p,q)$. It has already been claimed that the

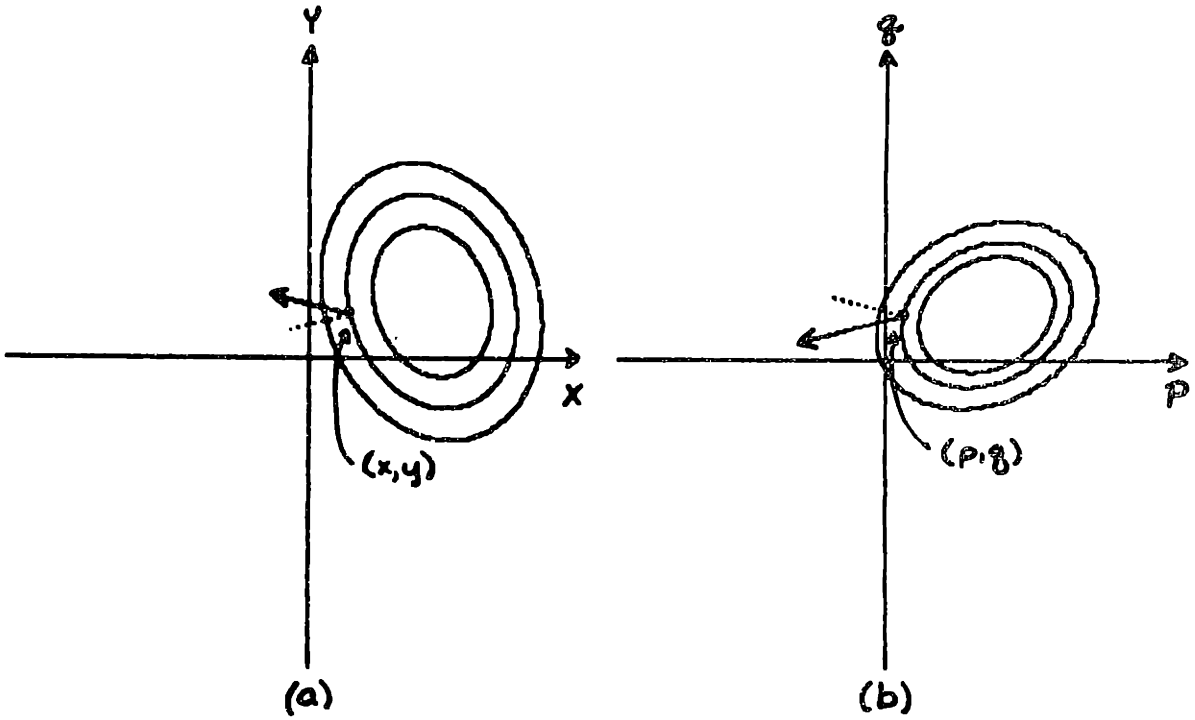

Figure A-1 Suppose image point (x,y) corresponds to gradient (p,q). In expanding a characteristic, movement in the image is in the direction normal to the contour of constant reflectance at (p,q). Similarly, movement in gradient space is in the direction normal to the contour of constant intensity at (x,y).

Hessian matrix H is the generalization to $\mathbb{R}^n$ of the concept of curvature of a function of a real variable. Here, it is established that the corresponding positive (negative) definiteness of the Hessian is the generalization of positive (negative) curvature.

> **Definition.** Let A be a real n x n symmetric matrix. Then A is called *positive semidefinite* if $x^TAx \geq 0$ for all $x \in \mathbb{R}^n$. A is called *positive definite* if $x^TAx > 0$ for all non-zero $x \in \mathbb{R}^n$. Similarly, A is called *negative semidefinite* if $x^TAx \leq 0$ for all $x \in \mathbb{R}^n$ and A is called *negative definite* if $x^TAx < 0$ for all non-zero $x \in \mathbb{R}^n$.

H is a real symmetric matrix (Corollary A.1). Therefore, it is appropriate to examine conditions under which H is positive (negative) definite. The positive (negative) definiteness of the Hessian matrix H is intimately related to the convexity (concavity) of the corresponding (hyper)surface $z = f(x)$. The following definitions and theorems give the required results:

> **Definition.** A real-valued function f(x) defined on a convex set $\Gamma \subset \mathbb{R}^n$ is said to be *convex* if, for every $x_1, x_2 \in \Gamma$ and every λ, $0 \leq \lambda \leq 1$,
>
> $$f(\lambda x_1 + (1 - \lambda)x_2) \leq \lambda f(x_1) + (1 - \lambda)f(x_2).$$
>
> If, for every $0 < \lambda < 1$ and $x_1 \neq x_2$
>
> $$f(\lambda x_1 + (1 - \lambda)x_2) < \lambda f(x_1) + (1 - \lambda)f(x_2),$$
>
> then f(x) is said to be *strictly convex*.
>
> Similarly, a real-valued function f(x) defined on a convex set $\Gamma \subset \mathbb{R}^n$ is said to be *concave* if -f(x) is convex and *strictly concave* if -f(x) is strictly convex.

Theorem A.2 Let $f(x)$ be a real-valued function defined on an open convex set $\Gamma \subset \mathbb{R}^n$ and let the (hyper)surface described by the equation $z = f(x)$ be smooth over Γ. Then, $f(x)$ is convex on Γ if and only if $H = \nabla^2 f(x)$ is positive semidefinite on Γ. Similarly, $f(x)$ is concave on Γ if and only if $H = \nabla^2 f(x)$ is negative semidefinite on Γ.

Unfortunately, theorem A.2 does not extend to strictly convex and strictly concave functions by simply replacing the inequalities by strict inequalities. The extent by which it does extend is given by the following theorem.

Theorem A.3 Let $f(x)$ be a real-valued function defined on an open convex set $\Gamma \subset \mathbb{R}^n$ and let the (hyper)surface described by the equation $z = f(x)$ be smooth over Γ. A sufficient but not necessary condition that $f(x)$ be strictly convex on Γ is that $H = \nabla^2 f(x)$ is positive definite on Γ. Similarly, a sufficient but not necessary condition that $f(x)$ be strictly concave on Γ is that $H = \nabla^2 f(x)$ is negative definite on Γ.

These results will now be used to show how convexity adds constraint. (A similar argument will hold for concavity.) Multiplying the two equations $[I_x, I_y]^T = H\,[R_p, R_q]^T$ and $[dp, dq]^T = H\,[dx, dy]^T$ on the left by $[R_p, R_q]$ and $[dx, dy]$ respectively generates the two inequalities:

$$[R_p, R_q]\, H\, [R_p, R_q]^T = I_x R_p + I_y R_q \geq 0$$

$$[dx, dy]\, H\, [dx, dy]^T = dp\,dx + dq\,dy \geq 0$$

The first inequality $I_x R_p + I_y R_q \geq 0$ can be viewed as additional *a priori* constraint on the contour in gradient space of possible solutions to the basic equation $I(x,y) = R(p,q)$ for image points (x,y) corresponding to

sections of surface that are convex. Suppose image point (x_0,y_0) has $I(x_0,y_0) = \alpha$. Figure A-2(a) shows the point (x_0,y_0) along with the corresponding image intensity contour $I(x,y) = \alpha$. The vector $[I_x, I_y]$ defines the direction normal to the contour $I(x,y) = \alpha$ at the point (x,y). Figure A-2(b) shows the reflectance map contour $R(p,q) = \alpha$. The vector $[R_p, R_q]$ defines the direction normal to the contour $R(p,q) = \alpha$ at the point (p,q).

$I_x R_p + I_y R_q \geq 0$ if and only if the angle between the normal $[I_x, I_y]$ and the normal $[R_p, R_q]$ is less than or equal to 90°. Thus, if (x_0,y_0) lies on a section of surface known to be convex, points on the contour $R(p,q) = \alpha$ for which $I_x R_p + I_y R_q < 0$ (the dotted section of the contour $R(p,q) = \alpha$ of figure A-2(b)) can immediately be excluded from the set of possible gradient points corresponding to image point (x_0,y_0).

The second inequality helps to constrain the movement in gradient space $[dp,dq]$ that can correspond to a movement $[dx,dy]$ in the image of a section of surface known to be convex. Suppose image point (x_0,y_0) is known to correspond to the gradient point (p_0,q_0). The vector $[dx,dy]$ defines the direction of movement in image space (figure A-3(a)). Now, $dp\,dx + dq\,dy \geq 0$ if and only if the angle between $[dx,dy]$ and the corresponding $[dp,dq]$ is less than or equal to 90°. Thus, if a movement is made in the direction $[dx,dy]$ from the image point (x_0,y_0) on a section of surface known to be convex, then the corresponding movement in gradient space must take the point (p_0,q_0) into the region R of figure A-3(b).

This second result can be used to choose $[dx,dy]$ in such a way as to guarantee that the view angle increases or that the direction of steepest descent increases. Figure A-4, illustrates what happens if $[dx,dy]$ is chosen to be in the direction $[p_0,q_0]$. In this case, the line

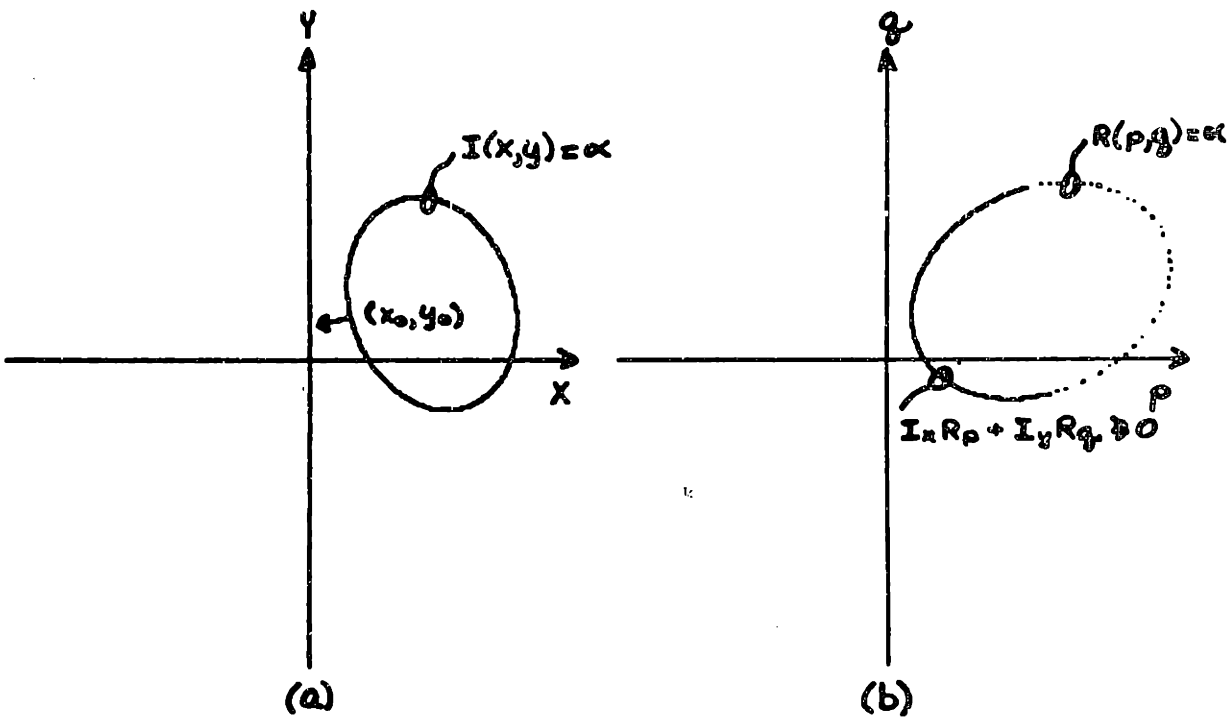

Figure A-2 The inequality $I_x R_p + I_y R_q \geq 0$ restricts the contour in gradient space that can correspond to a given image point.

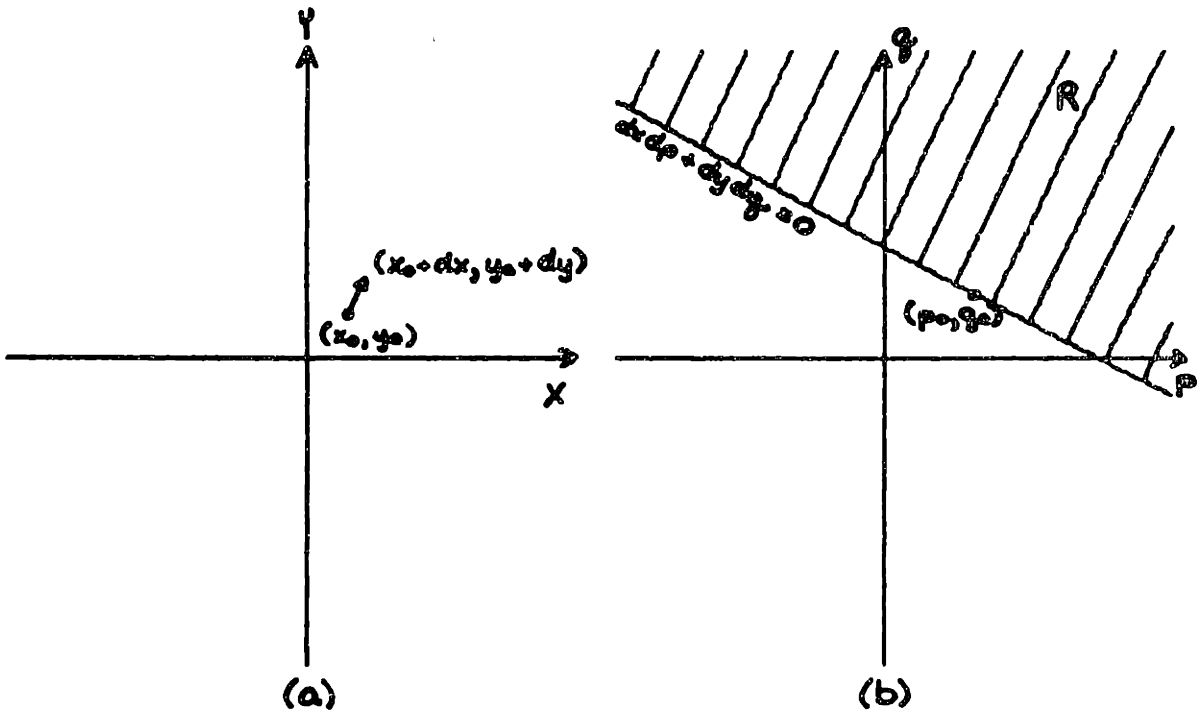

Figure A-3 The inequality dxdp + dydp ≥ 0 restricts the movement in gradient space that can correspond to a given movement in image space.

$dpdx + dqdy = 0$ is the tangent line to the gradient space circle $p^2 + q^2 = p_0^2 + q_0^2$. All points in R now lie outside this circle so that the point (p_0,q_0) must move to a point of increasing view angle.

Figure A-3, illustrates what happens if [dx,dy] is chosen to be in the direction $[-q_0,p_0]$. In this case, the line $dpdx + dqdy = 0$ is the line connecting (p_0,q_0) and the origin (0,0). All points in R lie above this line so that the point (p_0,q_0) must move to a point of increasing direction of steepest descent.

A.3 A GEOMETRIC INTERPRETATION OF MULTIPLICATION BY THE IMAGE HESSIAN

A useful geometric interpretation of multiplication by a real symmetric matrix can be derived from the fact that any positive definite matrix can be used to define a norm. One can begin by providing a geometric interpretation of multiplication by a positive definite H and then extend this result (trivially) to negative definite H and (finally) to arbitrary nonsingular H.

Definition. Let A be an n x n positive definite matrix and let $x \in R^n$. Then, $\|x\|_A$ is called the *A-norm of* x where

$$\|x\|_A^2 = x^T A x$$

The key observation is that an A-norm is like the standard Euclidean norm except that it applies disproportionate weights to the components of x in different directions. These weights and directions are determined by the eigenvalues and eigenvectors of A. The following three theorems establish this observation more formally.

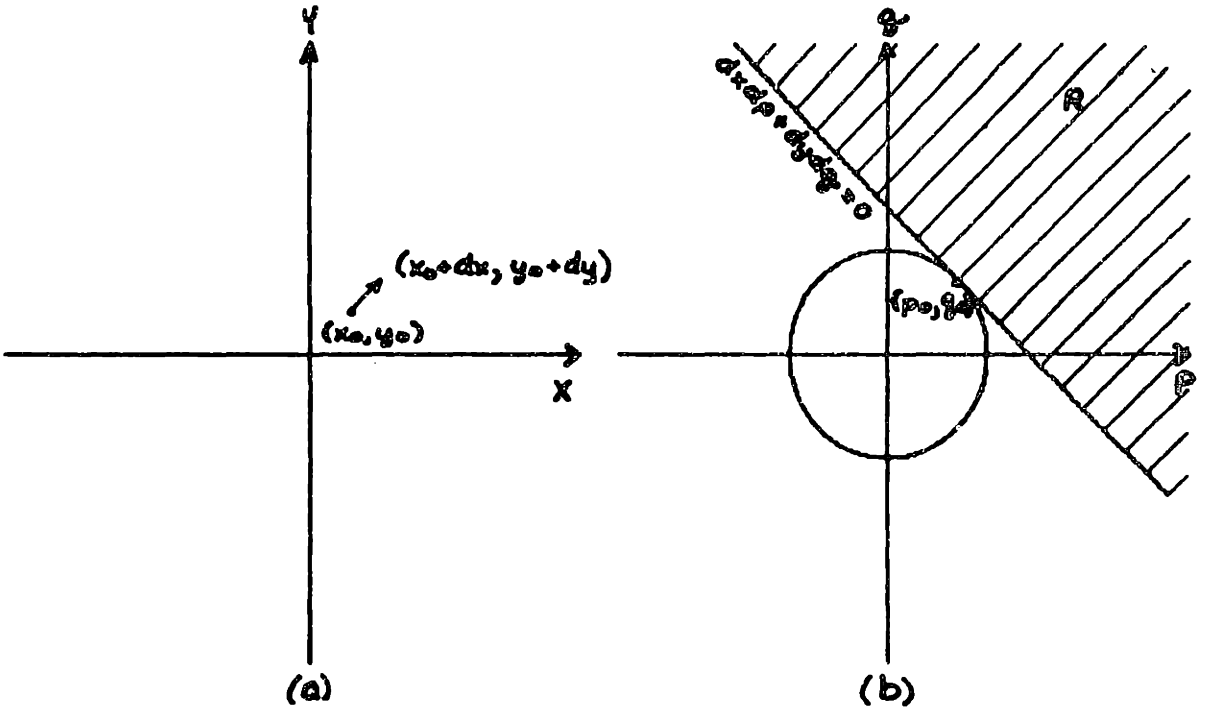

Figure A-4 Surface convexity can be used to choose a movement [dx,dy] in the image such that the corresponding movement [dp,dq] in gradient space increases the view angle e.

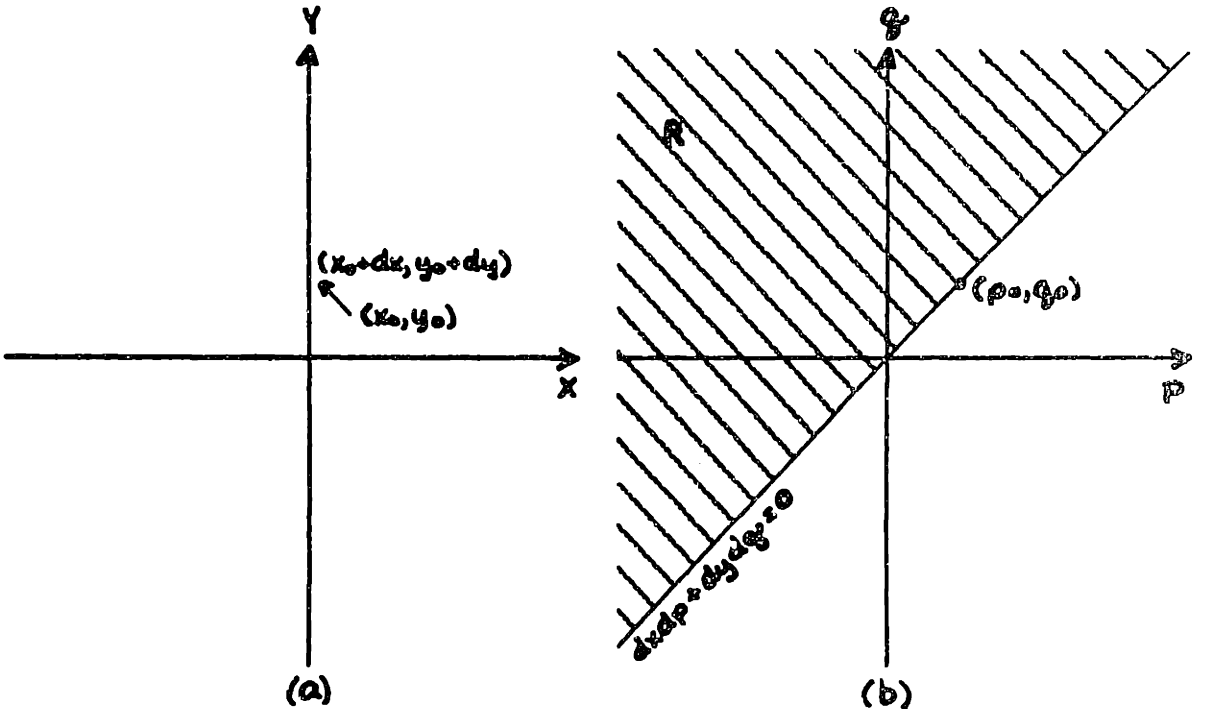

Figure A-5 Surface convexity can be used to choose a movement [dx,dy] in the image such that the corresponding movement [dp,dq] in gradient space increases the direction of steepest descent.

Theorem A.4 Let A be a real symmetric n x n matrix. Then all the eigenvalues of A are real and there exist n mutually orthogonal eigenvectors corresponding to each of the (not necessarily distinct) eigenvalues of A.

Theorem A.5 Let A be positive definite. Then all the eigenvalues of A are positive.

Theorem A.6 Let A be a positive definite n x n matrix. Let $\lambda_1,\lambda_2,\ldots,\lambda_n$ be the n positive but not necessarily distinct eigenvalues of A and let $\omega_1,\omega_2,\ldots,\omega_n$ be a corresponding set of n mutually orthogonal eigenvectors. (Without loss of generality, choose each ω_i to be a unit vector and order the ω_i so that the vectors $\omega_1,\omega_2,\ldots,\omega_n$ form a right-handed coordinate system.) Then, using $\omega_1,\omega_2,\ldots,\omega_n$ as a set of basis vectors, any n-vector x can be rewritten in the form:

$$x = y_1\omega_1 + y_2\omega_2 + \ldots + y_n\omega_n$$

Then:

$$\|x\|_A^2 = \lambda_1 y_1^2 + \lambda_2 y_2^2 + \ldots + \lambda_n y_n^2$$

Theorem A.6 follows from the fact that any n x n symmetric matrix A is orthogonally (rotationally) similar to an n x n diagonal matrix (of the eigenvalues of A). Knowing that all the eigenvalues of a positive definite matrix are positive guarantees that the quadratic form x^TAx satisfies the requirements of a metric norm. Theorem A.6 provides a useful geometric interpretation for multiplication of a vector by a positive definite matrix. To avoid unnecessary complication, let us specialize the interpretation to the case of the 2 x 2 Hessian matrix H corresponding to a surface z = f(x,y). Recall, from (A.2) above, that

$$[dp,dq]^T = H\,[dx,dy]^T$$

For notational convenience let

$$a = p_x,\ b = q_y \text{ and } c = p_y = q_x$$

Then, it can be shown that the two eigenvalues of H are:

$$\lambda_1 = \frac{a+b}{2} - \frac{1}{2}\sqrt{(a-b)^2 + 4c^2}$$

$$\lambda_2 = \frac{a+b}{2} + \frac{1}{2}\sqrt{(a-b)^2 + 4c^2}$$

and that the corresponding (unit) eigenvectors are:

$$\omega_1 = [\cos(\theta),-\sin(\theta)]$$

$$\omega_2 = [\sin(\theta),\cos(\theta)]$$

where

$$\tan(2\theta) = \frac{2c}{b-a}$$

Multiplication by H can then be interpreted as follows: the vector [dp,dq] is obtained by summing the components of [dx,dy] in each of the eigenvector directions ω_1 and ω_2 where each component is scaled respectively by the eigenvalues λ_1 and λ_2. Consider moving a small distance ds in the image. Consider the family of all [dx,dy] such that

$$ds = \sqrt{dx^2 + dy^2}$$

If H is positive definite at an image point (x_0,y_0) known to correspond to the gradient point (p_0,q_0), then multiplication by H induces a 1-1 continuous mapping of the image space circle centered at (x_0,y_0) and with radius ds onto the gradient space ellipse centered at (p_0,q_0) and with axes $\lambda_1 ds$ and $\lambda_2 ds$ in the directions ω_1 and ω_2 respectively. Figure A-6 illustrates this result (with image space coordinates and gradient space coordinates superimposed). The fact to be exploited is that the mapping from this image space circle to the corresponding gradient space ellipse is

continuous and 1-1. Multiplication by a positive definite H is monotonic in the following sense: multiplication by a positive definite H preserves the ordering in angular position of the [dp,dq]'s corresponding to given [dx,dy]'s. Let us make this more precise.

Definition. Suppose two non-zero vectors $x = [x_1, x_2]$ and $y = [y_1, y_2]$ are described in a right-handed (positive) coordinate system. Then x is said to be *(strictly) less in angular position* than y if the angle required to align x with y by rotating x in a counter-clockwise direction is (strictly) less than the angle required to align x with y by rotating x in a clockwise direction. Similarly, x is said to be *(strictly) greater in angular position* than y if the angle required to align x with y by rotating x in a counter-clockwise direction is (strictly) greater than the angle required to align x with y by rotating x in an clockwise direction.

Definition. Let $z = f(x,y)$ be the equation describing a smooth surface and let λ_1 and λ_2 be the two eigenvalues of the corresponding Hessian matrix H at image point (x_0, y_0). The surface $z = f(x,y)$ is said to be *planar at* (x_0, y_0) if and only if $\lambda_1 = \lambda_2 = 0$. The surface $z = f(x,y)$ is said to be *singly curved at* (x_0, y_0) if and only if one (but not both) of λ_1 and λ_2 is equal to zero. The surface $z = f(x,y)$ is said to be *doubly curved at* (x_0, y_0) if and only if both λ_1 and λ_2 are not equal to zero.

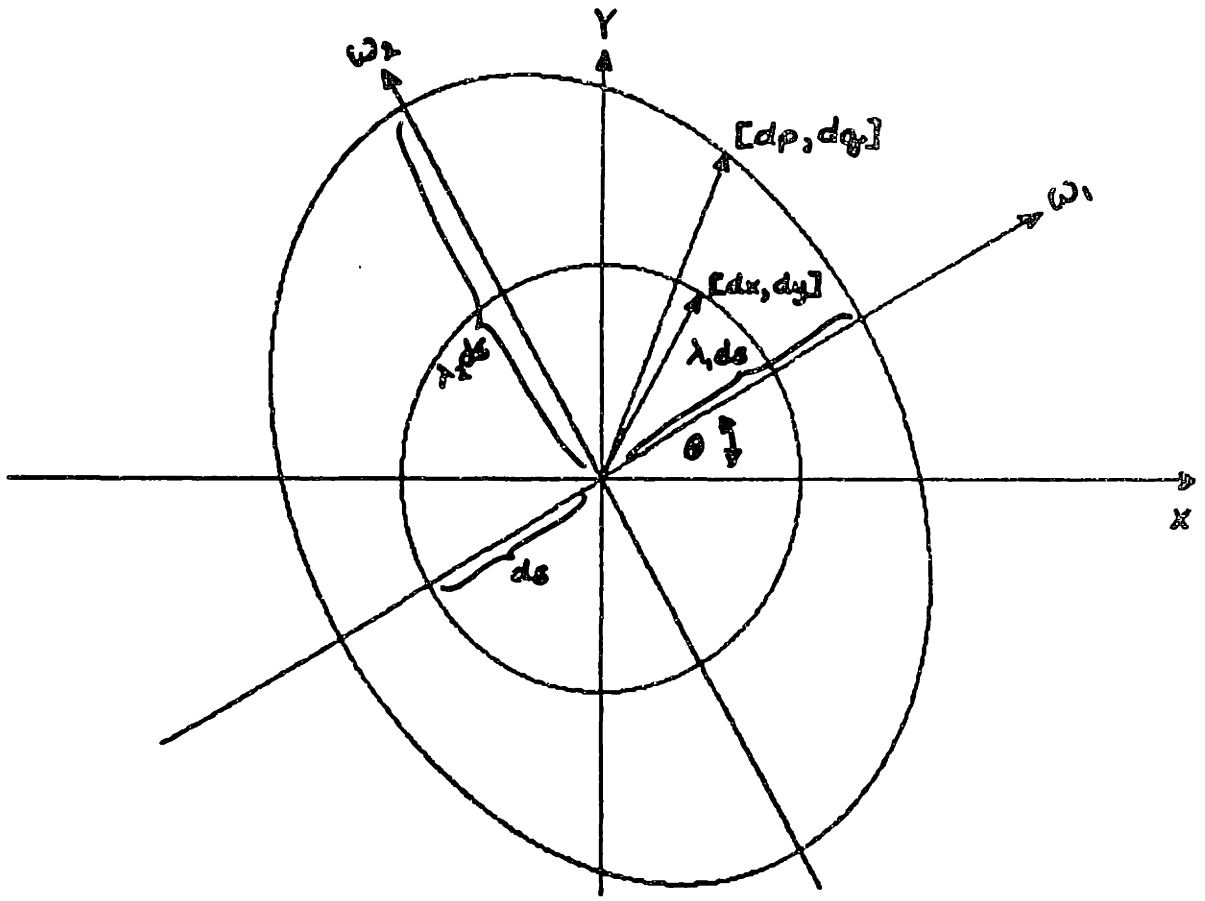

Figure A-6 Multiplication by the image Hessian H induces a 1-1 mapping between a circle of radius ds in the image and an ellipse in gradient space. The major and minor axes of this ellipse are determined by the eigenvalues and eigenvectors of H.

Theorem A.7 Let $z = f(x,y)$ be the equation describing a smooth surface. Then $z = f(x,y)$ is doubly curved at (x_0,y_0) if and only if the corresponding Hessian matrix H is nonsingular at (x_0,y_0).

Theorem A.8 Let $z = f(x,y)$ be the equation describing a smooth surface and suppose $z = f(x,y)$ is doubly curved at image point (x_0,y_0). Let H be the corresponding Hessian matrix at (x_0,y_0) having non-zero eigenvalues λ_1 and λ_2.

(i) If H is positive or negative definite (λ_1 and λ_2 have the same sign), then multiplication by H preserves the ordering of angular positions of $[dp,dq]$'s with respect to the corresponding $[dx,dy]$'s. That is, if $[dp_1,dq_1]^T = H\,[dx_1,dy_1]^T$, $[dp_2,dq_2]^T = H\,[dx_2,dy_2]^T$ and $[dx_1,dy_1]$ is (strictly) less in angular position than $[dx_2,dy_2]$ then $[dp_1,dq_1]$ is (strictly) less in angular position than $[dp_2,dq_2]$.

(ii) If H is neither positive nor negative definite (λ_1 and λ_2 have opposite sign), then multiplication by H reverses the ordering of angular positions of $[dp,dq]$'s with respect to the corresponding $[dx,dy]$'s. That is, if $[dp_1,dq_1]^T = H\,[dx_1,dy_1]^T$, $[dp_2,dq_2]^T = H\,[dx_2,dy_2]^T$ and $[dx_1,dy_1]$ is (strictly) less in angular position than $[dx_2,dy_2]$ then $[dp_1,dq_1]$ is (strictly) greater in angular position than $[dp_2,dq_2]$.

Theorem A.8 requires that $z = f(x,y)$ be doubly curved in order to guarantee that multiplication by H is a 1-1 mapping. However, if H is nonsingular, then theorem A.8 gives precise conditions with which to order the angular changes to position in gradient space corresponding to given movements in image space. If H is either positive or negative definite then the mapping of image space circle to gradient space ellipse goes from a right-handed (positive) coordinate representation to a right-handed (positive) coordinate representation so that the ordering of angular positions is preserved. If H is neither positive nor negative definite then the mapping of image space circle to gradient space ellipse goes from a right-handed (positive) coordinate representation to a left-handed (negative) coordinate representation so that the ordering of angular positions is reversed.

A.4 THE IMAGING MATHEMATICS OF A SPHERE

In this section, expressions are developed for the surface orientation and the image Hessian matrix H for images of a sphere. The purpose is not simply to perform an exercise in differential calculus. Rather, the analytic results developed here can be used to illustrate the connection between a viewer-centered definition of the image Hessian matrix H and a more traditional object-centered definitions of curvature.

Consider a sphere of radius r centered at the object space origin. The surface of the sphere is described (implicitly) by the equation:

$$f(x,y,z) = x^2 + y^2 + z^2 - r^2 = 0$$

This equation, however, gives no indication of which points on the surface actually appear in the image nor which points on the surface are hidden from view. It is an object-centered representation of the surface. In the

formulation used here, an explicit representation of the surface is required of the form $z = f(x,y)$. For the sphere, this explicit representation is given by the equation:

$$z = f(x,y) = -\sqrt{r^2 - x^2 - y^2}$$

This explicit representation of the form $z = f(x,y)$ is a viewer-centered representation. (Recall that the viewer is looking along the positive z-axis so that the points on the sphere actually in view correspond to negative values of z as indicated above.)

The gradient coordinates p and q are determined by differentiating f(x,y) with respect to x and y. One finds:

$$p = \frac{\partial f(x,y)}{\partial x} = \frac{-x}{z}$$

$$q = \frac{\partial f(x,y)}{\partial y} = \frac{-y}{z}$$

Taking second partial derivatives of f(x,y) with respect to x and y, one finds:

$$p_x = \frac{\partial^2 f(x,y)}{\partial x^2} = -\frac{(r^2-y^2)}{z^3}$$

$$q_y = \frac{\partial^2 f(x,y)}{\partial y^2} = -\frac{(r^2-x^2)}{z^3}$$

$$p_y = q_x = \frac{\partial^2 f(x,y)}{\partial x \partial y} = -\frac{xy}{z^3}$$

Thus, the Hessian matrix H is given by:

$$H = -1/z^3 \begin{bmatrix} r^2-y^2 & xy \\ xy & r^2-x^2 \end{bmatrix}$$

The eigenvalues of the Hessian matrix H are given by:

$$\lambda_1 = \frac{-1}{z}$$

$$\lambda_2 = \frac{-r^2}{z^3}$$

and that the corresponding (unit) eigenvectors are:

$$\omega_1 = [\sin(\theta), -\cos(\theta)]$$

$$\omega_2 = [\cos(\theta), \sin(\theta)]$$

where

$$\tan(\theta) = \frac{y}{x}$$

First, consider the special case $x = 0$ $y = 0$. Then $z = f(0,0) = -r$, $p = 0$, $q = 0$ and the Hessian matrix H becomes:

$$H = \begin{bmatrix} 1/r & 0 \\ 0 & 1/r \end{bmatrix}$$

This is as might be expected. The curvature in each of the two principal directions of movement is the same (and equal to the reciprocal of the radius of the sphere). This fact is true for any point on the surface of a sphere. (Conversely, a sphere is the only surface for which this fact is true at every point.) If one is standing (normally) at a point on a sphere and looking about, then the surface curvature is the same in every direction. But, in saying that one is standing (normally) on the surface of the sphere one is considering an object-centered definition of curvature.

A.5 RELATING THE IMAGE HESSIAN TO OBJECT CURVATURE

The way the image Hessian matrix H has been formulated in this thesis corresponds to a viewer-centered definition of curvature. Using the explicit surface representation $z = f(x,y)$, the corresponding Hessian matrix H relates movement in the image to changes in local surface

orientation (and not movement on the object surface to changes in local surface orientation). The case $x = 0$ $y = 0$ is the unique situation for which the object-centered definition of curvature and the viewer-centered definition of curvature coincide. Here, the value of the Hessian matrix $\mathbf{H}$ is intuitively what one would expect from a "curvature" matrix. In a viewer-centered representation, the image Hessian matrix $\mathbf{H}$ is not constant, even for the case of a simple quadratic surface such as a sphere. Although this is perhaps confusing, a little thought will reveal that this is necessarily true. In general, a circle of (infinitesimal) radius ds in the image does not correspond to a circle on the object surface. The dependence of H on x and y captures the variation in apparent curvature when a surface is viewed obliquely.

This can be made clear if the expression for the image Hessian $\mathbf{H}$ of a sphere is rewritten in terms of gradient coordinates p and q. One finds:

$$\mathbf{H} = 1/\cos(e)\begin{bmatrix} p^2+1 & pq \\ pq & q^2+1 \end{bmatrix}\begin{bmatrix} 1/r & 0 \\ 0 & 1/r \end{bmatrix}$$

where e is the view angle. That is:

$$\cos(e) = \frac{1}{\sqrt{1 + p^2 + q^2}}$$

The following two theorems provide the necessary analytic results to interpret the above expression for the image Hessian matrix H:

> **Theorem A.9** Let $z = f(x,y)$ be the equation describing a smooth surface. Let dA be a differential element of area on the surface. Then,
>
> $$dA = \frac{1}{\cos(e)}dxdy$$
>
> where dxdy is the corresponding differential element of

area in the image and e is the view angle subtended by the surface element dA. Thus, the surface area corresponding to a region R in the image is given by:

$$A = \iint_R \sec(e)\, dxdy$$

Theorem A.10 Let $z = f(x,y)$ be the equation describing a smooth surface. Let ds be the differential of the arc on the surface corresponding to a movement [dx,dy] in the image. Then, ds is given by the A-norm of [dx,dy]. That is,

$$ds = \|[dx,dy]\|_A = \sqrt{[dx,dy]A[dx,dy]^T}$$

where the matrix A is given by:

$$A = \begin{bmatrix} p^2+1 & pq \\ pq & q^2+1 \end{bmatrix}$$

Thus, theorem A.9 allows one to interpret multiplication by $1/\cos(e)$ as compensation for the foreshortening of area due to the oblique view corresponding to an object point with gradient (p,q). Similarly, theorem A.10 allows one to interpret multiplication by A as compensation for the foreshortening of arc length due to the oblique view corresponding to an object point with gradient (p,q). Note that finding the area of surface corresponding to a given region of image depends only on the magnitude of the gradient at each image point in the region. On the other hand, finding the arc length along the surface corresponding to a given curve in the image depends on both the magnitude and angular position of the gradient at each image point on the curve.

This dependence of arc length on the gradient (p,q) can be made more explicit by, once again, examining the eigenvalue and eigenvector structure of A. A is positive definite with eigenvalues:

$$\lambda_1 = 1$$

$$\lambda_2 = \frac{1}{\cos^2(\theta)}$$

and corresponding (unit) eigenvectors:

$$\omega_1 = [\sin(\theta), -\cos(\theta)]$$

$$\omega_2 = [\cos(\theta), \sin(\theta)]$$

where

$$\tan(\theta) = \frac{q}{p}$$

Thus, the component of the differential ds of the arc on the surface in the direction of steepest descent is foreshortened by the factor cos(e) while the component of the differential ds in the direction of the contour of constant z = f(x,y) is unchanged.

Since A is positive definite, it is also invertible (and its inverse A^{-1} is positive definite). Thus, knowing the gradient point (p,q) and the Hessian matrix H at an image point (x,y) allows one to determine the magnitude and direction of the (object-centered) principal radii of curvature of the object surface z = f(x,y). Suppose that k_1 and k_2 are the two eigenvalues and ω_1 and ω_2 are the corresponding (unit) eigenvectors of the matrix C where

$$C = \cos(e)A^{-1}H = \cos^3(e)\begin{bmatrix} q^2+1 & -pq \\ -pq & p^2+1 \end{bmatrix} H$$

Then, $r_1 = 1/k_1$ and $r_2 = 1/k_2$ are the two principal radii of curvature of the object surface z = f(x,y) (oriented respectively in the directions

defined by ω_1 and ω_2). C can thus be written in the form

$$C = \begin{bmatrix} \cos(\alpha) & -\sin(\alpha) \\ \sin(\alpha) & \cos(\alpha) \end{bmatrix} \begin{bmatrix} 1/r_1 & 0 \\ 0 & 1/r_2 \end{bmatrix} \begin{bmatrix} \cos(\alpha) & \sin(\alpha) \\ -\sin(\alpha) & \cos(\alpha) \end{bmatrix}$$

where α is the direction in the image corresponding to ω_1.

Finally, since $\cos(e) > 0$ and A^{-1} is positive definite, the number of non-zero eigenvalues of H is equal to the number of non-zero eigenvalues of $C = \cos(e)A^{-1}H$. An eigenvalue λ_i of H is zero or non-zero precisely as the corresponding principal radius of curvature r_i is infinite or finite. Thus, the definitions of a surface $z = f(x,y)$ being planar at (x_0,y_0), singly curved at (x_0,y_0) and doubly curved at (x_0,y_0) given in terms of the (viewer-centered) Hessian matrix H are equivalent to the perhaps more standard definitions given in terms of the (object-centered) principal radii of curvature $r_1 = 1/k_1$ and $r_2 = 1/k_2$.

APPENDIX B: CATALOGUING CASTING DEFECTS

The initial goal in exploring casting inspection as a suitable area of application for machine vision was to develop a simple catalogue of defects in metal castings. The first observation to be made is that the phrase "defects in metal castings" encompasses a broad spectrum of possible issues. The defects asssociated with a particular casting process fall roughly into one of three categories:

1. INHERENT DEFECTS
   - defects introduced during the preparation of the metal alloy or other raw materials
2. PROCESSING DEFECTS
   - defects introduced during the casting process
3. SERVICE DEFECTS
   - defects introduced during the operating cycle of the casting

Here, only defects introduced by the casting process itself are considered. It is appropriate to further split such processing defects into three categories:

1. SHAPE DEFECTS
   - defects that affect the overall dimensional accuracy of the part
2. SURFACE DEFECTS
   - defects that manifest themselves as local surface properties of the part

3. STRUCTURE DEFECTS

- defects that affect the mechanical response of the part

These three categories of processing defects are not mutually exclusive. There is considerable overlap between categories. The kind of inspection considered in this work relates primarily to SURFACE defects. SHAPE defects related to the accurate verification of part dimensions are excluded. STRUCTURE defects which can be found only by destructive testing, special test equipment or by imaging rays which penetrate the object surface (eg. X-rays, ultra-sonic rays) are also excluded. As the catalogue below demonstrates, many defects which affect the structural properties of a casting are nonetheless manifest as surface properties. These are not excluded.

Before presenting the catalogue, a slight disclaimer is in order: this catalogue of casting defects really should take into account the particular alloy used, the particular casting technique chosen and the particular part geometry. Fortunately, however, each alloy, each casting technique and each part geometry share the same broad categories of defects. The difference lies in the relative rate of occurrence of the various kinds of defects and, to a lesser extent, in the way in which these defects manifest themselves.

With that disclaimer, here is the catalogue of defects:

COLD SHUT (FLOW MARK)

DESCRIPTION:

A defect that affects both the SURFACE and the STRUCTURE of a casting. Broadly speaking, a cold shut defect arises when molten metal does not weld together properly. There are two types of cold shut defect. One type occurs at the interface of two streams of molten metal whose temperature differential prevents them from welding together properly. This is manifest as a lapping or layering on the surface of the casting. The other type results from loose droplets of molten metal entering the mold cavity ahead of the main stream of metal. These solidify and become partially embedded in the surface of the casting.

CAUSES

DESIGN:

- portions of the mold too cold

PRODUCTION:

- pouring/injection rate too slow
- mold temperature too low
- metal temperature too low
- dirty metal (gating blockages)

CRACKS

DESCRIPTION:

A defect that affects both the SURFACE and the STRUCTURE of a casting. A crack is a defect that occurs during contraction shrinkage following solidification. Localized stresses are set up within a casting immediately following solidification, especially at junctions of restraining ribs, right angle intersections, and junctions between thick and thin sections.

These stresses can produce cracks as the casting cools to room temperature. Because such cracks occur after solidification, there is little chance for oxidization and they are typically very clean.

CAUSES

DESIGN:

- uneven or too rapid cooling
- excessive mold rigidity restraining normal contraction of the metal

PRODUCTION:

- mechanical jarring during removal from the mold

HOT TEARS

DESCRIPTION:

A defect that affects both the SURFACE and the STRUCTURE of a casting. A hot tear is a cracklike defect that occurrs during solidification. As the molten metal touches the comparatively cold mold surface, it soldifies as a skin and starts contracting ahead of the remainder of the casting. This skin is placed in tension and may tear if it becomes overstressed. These tears are characterized by having a heavily oxidized surface while CRACKS (see above), which occur after solidification, are relatively clean.

CAUSES

DESIGN:

- uneven or too rapid cooling
- excessive mold rigidity restraining normal contraction of the metal
- poor pattern design

  too small a radius of curvature at a section boundary

  too high a ratio of areas between sections joined in a T

INCLUSIONS

DESCRIPTION:

Inclusions are defects that arise due to foreign material trapped in a casting. Inclusions affect both the SURFACE and the STRUCTURE of a casting. Broadly speaking, inclusions are classified according to their origin.

INCLUSIONS OF METALLIC ORIGIN (DROSS/SLAG)

Improper melting and pouring practice may cause metallic inclusions in the casting. The formation of oxides, slag and other metallic waste material is an inherent part of the melting process. This slag material is lighter than the molten metal and floats to the surface. Careful design of the metal feeding system attempts to take advantage of this fact to prevent slag material from entering the mold cavity.

CAUSES

DESIGN:

- faulty gating design

PRODUCTION:

- poor quality control on raw materials
- superheating of metal in melting furnace
- melting cycle too long
- turbulent flow of metal

INCLUSIONS OF NON-METALLIC ORIGIN

Some of the possible sources of non-metallic inclusions are:

Mold and core material

Extraneous mold and core material may remain loose in the mold cavity or may be generated by the erosive action of the incoming molten metal.

Pattern material

In investment casting, residue from wax or plastic patterns may remain in the mold cavity and contaminate the casting.

Crucible and furnace lining material

Lining breakdown in crucibles and melting furnaces adds contaminants to the molten metal.

(PARTING LINE) MISMATCH

DESCRIPTION:

A defect that alters both the SURFACE and the SHAPE of a casting. (Parting line) mismatch occurs in casting techniques that employ a two-piece mold. Misalignment between the mold halves induces a step shift at the parting line of the casting. This results in a surface irregularity and loss of dimensional accuracy. The tolerable degree of parting line mismatch is generally specified in the mechanical drawing of a casting.

CAUSES

DESIGN:

- misalignment of pins and receptacles of the mold halves

PRODUCTION:

- play (due to wear over time) developing between pins and receptacles of mold halves

MISRUN

DESCRIPTION:

A SHAPE defect due to the incomplete filling of the mold cavity. Misruns occur when an advancing stream of molten metal lacks sufficiant force to overcome back pressure generated in the mold. (Typically, misruns occur in isolated thin sections of a casting.)

CAUSES

DESIGN:

- faulty gating design
  (need for additional vents, overflows or altered direction of metal flow)
- low mold permeability
- incorrect mold/metal temperatures

PRODUCTION:

- dirty metal (gating blockages)
- failure of mold reaction inhibitors (excessive evolution of gases)
- overlubrication (inhibits permeability)
- pouring/injection rate too slow
- inadequate quantity of molten metal in shot well
- mold temperature too low
- metal temperature too low

POROSITY

DESCRIPTION:

There is some confusion about the use of the term porosity. When not distinctly referring to shrinkage porosity, porosity generally implies bubbles of gas entrapped in the metal during solidification. Many of these bubbles remain internal to the casting and thus represent STRUCTURE defects (internal porosity). Certain others reach the surface during solidification and thus represent SURFACE defects (surface porosity). Large surface porosity defects are commonly referred to as BLOWHOLES. Small surface porosity defects are commonly referred to as PINHOLES. There are three main sources of entrapped gas in a casting:

1. Gas evolved within the molten metal itself. (Gas solubility in a metal decreases as temperature decreases.)
2. Air trapped in mold cavity
3. Gas evolved due to chemical reactions between the casting metal and the mold or core material

CAUSES

DESIGN:

- faulty gating design
- improper mold reaction inhibitors
- improper innoculants
- low mold permeability
- incorrect mold/metal temperatures
- poor metal handling

PRODUCTION:

- overlubrication
- pouring/injection rate too slow
- turbulent flow of metal
  - pouring/injection rate too high
  - partial blockage in gating system
- mold temperature too high
- metal temperature too high
- contamination of raw materials

SHRINKS

(SHRINK CAVITIES, SHRINKAGE VOIDS, SHRINKAGE POROSITY, PIPE)

DESCRIPTION:

In cooling from a molten state to room temperature, metal goes through three stages of shrinkage:

volumetric shrinkage as a liquid

solidification shrinkage during conversion to a solid

contraction shrinkage as a solid cooling to room temperature

Shrinkage defects (commonly referred to a shrink cavities, shrinkage voids, shrinkage porosity or pipe) are STRUCTURE defects. They arise due to metal shrinkage within a shell of already solidified metal that is not compensated for by a continued inflow of molten metal. Shrinkage defects typically occur near the center of large, heavy sections of a casting.

CAUSES

DESIGN:

- faulty gating design
- poor control of direction of solidification

PRODUCTION:

- pouring/injection rate too slow
- mold temperature to high
- metal temperature too high
- carbon equivalent of metal too low

MISCELLANEOUS METAL/MOLD INTERACTION DEFECTS

In the discussion of green sand mold casting, we have already seen a table of miscellaneous surface defects that result from a poor metal-to-mold interface. In permanent mold casting techniques, there are similar defects.

SOLDERING:

Soldering is a SURFACE defect in permanent mold castings due to the adhering of metal to the mold surface. Soldering results in pimples or torn skin on the surface of the casting. It arises when the mold surface has become pitted or when there is inadequate lubrication between mold and metal.

STAINS:

Excessive lubrication of the mold surface can result in stains on the surface of the casting.